Synchrotron radiation based studies of complex molecules on surfaces

Karsten Handrup, M.Sc.

Thesis submitted to the University of Nottingham for the degree of Doctor of Philosophy.

December 2013

Contents

Acknowledgements

I would like to thank my supervisor, James N. O'Shea, and my colleagues Andrew J. Britton, Matthew Weston, Robert H. Temperton and Andrew J. Gibson, as well as everyone in the NanoScience Group at the University of Nottingham. I would like to thank all the technical support at MAXlab, particulary the I311 and D1011 beamline managers, Karina Schulte and Alexei Preobrajenski. I would also like to thank Nicolaou Alessandro and Nicolas Jaouen for the technical support at the SEXTANS beamline at SOLEIL. I am grateful for the financial support through the Marie Curie Action - ITN SMALL network.

Abstract

In this thesis two single molecule magnets based on the dodecamanganese (III, IV) cluster, with either benzoate or terphenyl-4-carboxylate ligands have been studied on the Au(111) and rutile TiO_2(110) surfaces. We have used *in situ* electrospray deposition to produce a series of surface coverages from a fraction of a monolayer to multilayer films in both cases. X-ray absorption spectroscopy measured at the Mn L-edge (Mn $2p$) has been used to study the effect of adsorption on the oxidation states of the manganese atoms in the core. In the case of the benzoate-functionalized complex, reduction of the manganese metal centres is observed due to the interaction of the manganese core with the underlying surface. In the case of terphenyl-4-carboxylate, the presence of this much larger ligand prevents the magnetic core from interacting with either the gold or the titanium dioxide surfaces and the characteristic Mn^{3+} and Mn^{4+} oxidation states necessary for magnetic behaviour are preserved.

In contrast to the single molecule magnets where no charge transfer between the molecules and the substrates or within the molecules themselves were wanted, the molecules of bi-isonicotinic acid and the giant zinc porphyrin nanorings have been studied on rutile TiO_2(110) and Au(111) surfaces in the pursuit of charge transfer. In the case of the bi-isonicotinic acid it is studied on the rutile TiO_2(110) where the technique of resonant inelastic X-ray scattering was been employed. Here we introduce the core-hole clock implementation to estimate the charge transfer from the molecule to the substrate. We verify previous results of ultrafast charge transfer in the sub-femtosecond regime (2.9 $\pm$ 0.3 femtoseconds) out of the LUMO+1 orbital. When the higher lying state of the LUMO+2 state is probed charge transfer out of this state and to the

substrate is possibly there, but it is not possible to resolve it since it is masked by other effects originating from the inelastic scattering of the system. Furthermore, we see potential charge transfer within the molecule itself and new states observed in the inelastic scattering

Finally, zinc porphyrin nanorings were investigated on two surfaces of rutile $TiO_2(110)$ and Au(111). The techniques used here were X-ray photoemission spectroscopy and resonant photoemission spectroscopy. When the rutile $TiO_2(110)$ surface was employed hardly any participator decay was present suggesting charge transfer within the molecule itself or to the surface. This is further backed up by the fact that all of the core-excited unoccupied states are found to overlap energetically with the unoccupied states of the substrate, facilitating charge transfer out all the core-excited states. In the case of the Au(111) surface somewhat similar results are found, having all the core-excited states of the molecule located within the unoccupied states of the substrate, which again will facilitate charge transfer out all the core-excited states of the molecule. When the Au(111) substrate was employed the technique of near edge X-ray absorption fine structure was used to investigate the geometric orientation of the molecule on the surface. With the result of $86° \pm 10°$ to the surface normal we verify previous scanning tunneling microscopy measurement that the zinc porphyrin nanorings will take a flat lying orientation on the gold substrate.

List of publications

1. "*Single molecule magnets with protective ligand shells on gold and titanium dioxide surfaces: in-situ electrospray deposition and x-ray adsorption spectroscopy*", **K. Handrup**, V. J. Richards, M. Weston, N. R. Champness and J. N. O'Shea, The Journal of Chemical Physics, **139**, 154708 (2013).

2. "*Experimental observation of sub-femtosecond charge transfer in a model water splitting dye-sensitized solar cell*", M. Weston, **K. Handrup**, T. J. Reade, N. R. Champness, and J. N. O'Shea, The Journal of Chemical Physics, **137**, 224706 (2012).

3. "*Adsorption of dipyrrin-based dye complexes on a rutile TiO_2(110) surface*", M. Weston, T. J. Reade, **K. Handrup**, N. R. Champness, and J. N. O'Shea, The Journal of Chemical Physics C, 2012, **116** (34), 18184-18192.

4. "*Charge transfer dynamics from and within an aromatic adsorbate on a semiconductor TiO_2 surface probed on the femtosecond time scale with resonant inelastic x-ray scattering*", **K. Handrup**, A. J. Gibson, R. H. Temperton and J. N. O'Shea, (in preparation).

5. "*Zinc porphyrin nanoring adsorbed on rutile TiO_2(110) and Au(111) investigated by resonant photoemission spectroscopy*", **K. Handrup**, M. Westen and J. N. O'Shea, (in preparation).

Chapter 1

Introduction

1.1 Nanoscience

Nanoscience by its very nature, crosses and joins many scientific and engineering disciplines and the "birth" of this scientific discipline is often referenced to a simple but clear question which the legendary physicist Richard P. Feynman asked in his "There's plenty of room at the bottom" lecture in 1959 [1]. Feynman posed why matter could not be manipulated and controlled atom-by-atom since there was apparently no physical law prohibiting this type of nanoscale engineering. In his lecture he also proposed two challenges, with financial incentive. Feynman's first challenge of reducing the first page of a book by 25000 times took almost three decades, and was achieved by the lithographic technology used in the semiconductor industry. These processes are still being pushed to create ever smaller, faster, cheaper electronics. Currently Intel's state-of-the-art production processor chips contain transistors with a 45 nm footprint[2], achieved using ultraviolet lithography. The second challenge from Feynman was to create an electric motor no greater than 1/64th inch cubed. To his surprise William McLellan created such a device only 5 months later. This could possibly be thought of as the birth of micro electrical mechanical systems, MEMS. The interdisciplinary nature of nanoscience includes a broad variety of different disciplines stretching over organic photovoltaic to research within molecular building block for nanoscale electronics.

One of the great motivations for the investigation within organic photovoltaic is founded in the ever increasing demand for new technologies to fulfill the human exploration of resources. The past century has seen an average worldwide temperature rise of 0.7°C (1906-2005) [3]. There is now very little doubt that human activities are to blame for example the enormous emissions of greenhouse gases [3]. Without action, temperatures are expected to rise further with devastating environmental consequences. These include the retreat of Antarctic ice sheets causing sea levels to rise and releasing further greenhouse gases (methane) from melting permafrost. It is the ever increasing requirement for energy that is at the heart of the problem, especially within the ever growing electronic industry, which supplies the whole chain within our production of every day items, consumer products to heavy industry and our infrastructure. With an estimated 120 PW of sunlight reaching the Earth's surface solar electric generation has been one of the obvious choices to explore for the last half century. For the past couple of decades organic solar cells have come into focus due to their low production cost in high volumes and with the combination of high flexibility of organic molecules, organic solar cells are potentially cost-effective, more energy-efficient, and more environment-friendly than their inorganic counterparts.[4, 5]

The traditional solar cells consists of a relatively narrow band gap semiconductor such as silicon. When electromagnetic radiation is absorbed in the device, the energy, due to the photovoltaic effect, is converted into electrical energy. All photovoltaic devices are based on the concept of charge separation at the interface between two materials with different methods of charge conduction caused by incident visible light. In Figure 1.1 the schematics are shown of a conventional silicon based solar cell. The charge separation occurs due to the interface between two differently doped regions of a semiconductor. In the n-type region of the system is doped with atoms called donors which at room temperature supply the conduction band of the silicon with electrons. The p-type region the system consists of acceptor atoms, which play the role of supplying the valence band of the silicon with holes. This donor-acceptor

difference across the p-n-junction creates an electric field. The energy levels associated with this cell are schematically illustrated in Figure 1.1. An incoming photon will create a electron-hole pair as electrons are excited across the band gap of the silicon, from the valence to the conduction band. The generation of a photocurrent is done by the charge separation, and is obtained through the potential difference that naturally exists across the junction region. In the thermodynamic equilibrium, (no-light) the electrochemical potential is constant across the device, giving rise to a "built-in" voltage. The electrochemical potential is defined as the sum of the electrical potential energy and the chemical potential energy and is identified with the Fermi level (E_F) [6]. Out of equilibrium, quasi-Fermi levels specific to the type of carrier are defined in analogy to the equilibrium Fermi level.

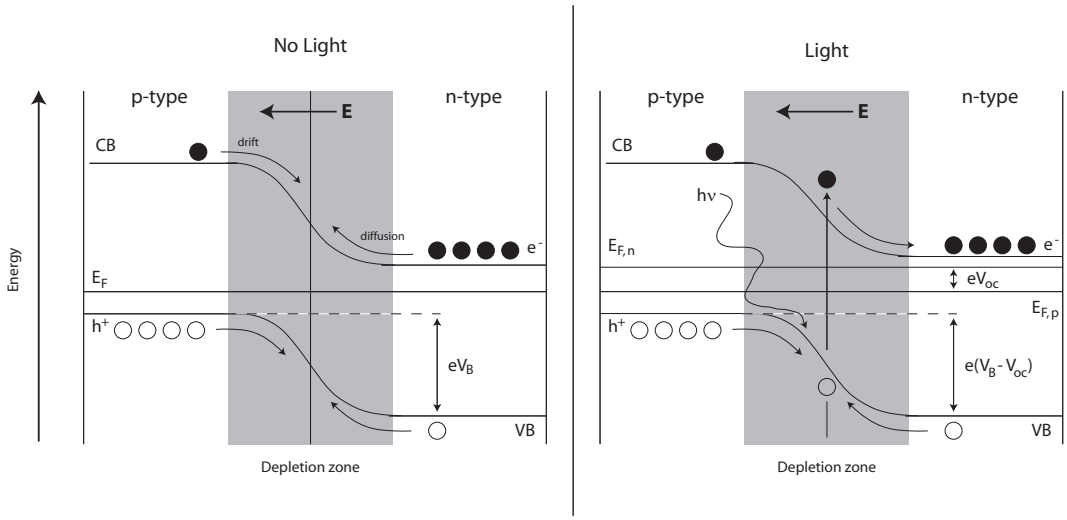

Figure 1.1: Schematic operation of a p-n junction at open circuit when no light is present is illustrated on the left hand side. On the right the situation of illumination is found. The coloured spheres represent electrons and the non-coloured will be holes. The terms CB, V_B, E_F, will denote the conduction band, valence band and Fermi level, respectively. The terms $E_{f,n}$ and $E_{f,p}$ are the quasi-Fermi levels for the electron and the hole, respectively. V_B is the built-in voltage and V_{OC} represents the open circuit voltage caused by the adsorption of photons of energy $h\nu$. Because the quasi-Fermi levels are approximately constant, V_{OC} is both the contact potential difference (assuming ohmic contacts) and the maximum possible photovoltage (largest splitting of quasi-Fermi levels).

The great advantage of using amorphous silicon solar cells is their lim-

ited production cost in low power applications, such as calculators and wrist watches. A major disadvantage of using conventional silicon based solar cells is the high cost of processing silicon and the relative thick layer – micrometers – of doped silicon needed to ensure a reasonable photon capture, and it degrades in sunlight since it suffers from photocorrosion.[7] A wide-band gap semiconductor such as TiO_2, with a band-gap of 3.1 eV, fits the latter criteria of not suffering from the same amount of photocorrosion as silicon. This is due to the band-gap being a measure of the chemical bond strength, therefore the higher the band-gap available, the higher the resistance against photodegradation.[7] The straightforward solution to the former problem is by using a low-cost material. Looking towards the well-established mass production industry, where low-production cost is a key issue, the material of titanium dioxide, TiO_2, is found. In this scenario TiO_2 is widely used in white pigments, and in everyday items such as paper, paint, toothpaste and sun cream.[8] If TiO_2 should be the material of choice in the pursuit of renewable energy sources some fundamental questions arise about its physical properties. With a band-gap of 3.1 eV it will be sensitive to the ultraviolet, UV, part of the electromagnetic radiation spectrum. Approximately 95% of the UV light is blocked by the Earth's atmosphere, whereas at the Earth's surface approximately 40% for the electromagnetic radiation consist of visible light.[9] Since TiO_2 crystal is transparent and will therefore not absorb visible light. The physical properties of the TiO_2 crystal needs to be changed so it will absorb visible light. This can be done by adding a dye to its surface, and since dyes are colourful substances they will absorb some part of the visible spectrum. This phenomenon was discovered by Vogel in 1883 in his pursuit of changing the silver halide emulsions in photographic films to longer wavelengths.[10] In the late 1960s Gerischer *et al.* describes how electricity can be generated at oxide electrodes in an electrochemical cell by illuminating organic dyes,[11] but is was not until 1991 when Brian O'Regan and Michael Grätzel[12] introduced the modern high efficient dye-sensitized solar cell (DSSC) a true departure from the classic solid state junction device was taken. They presented a solar cell with a promising energy

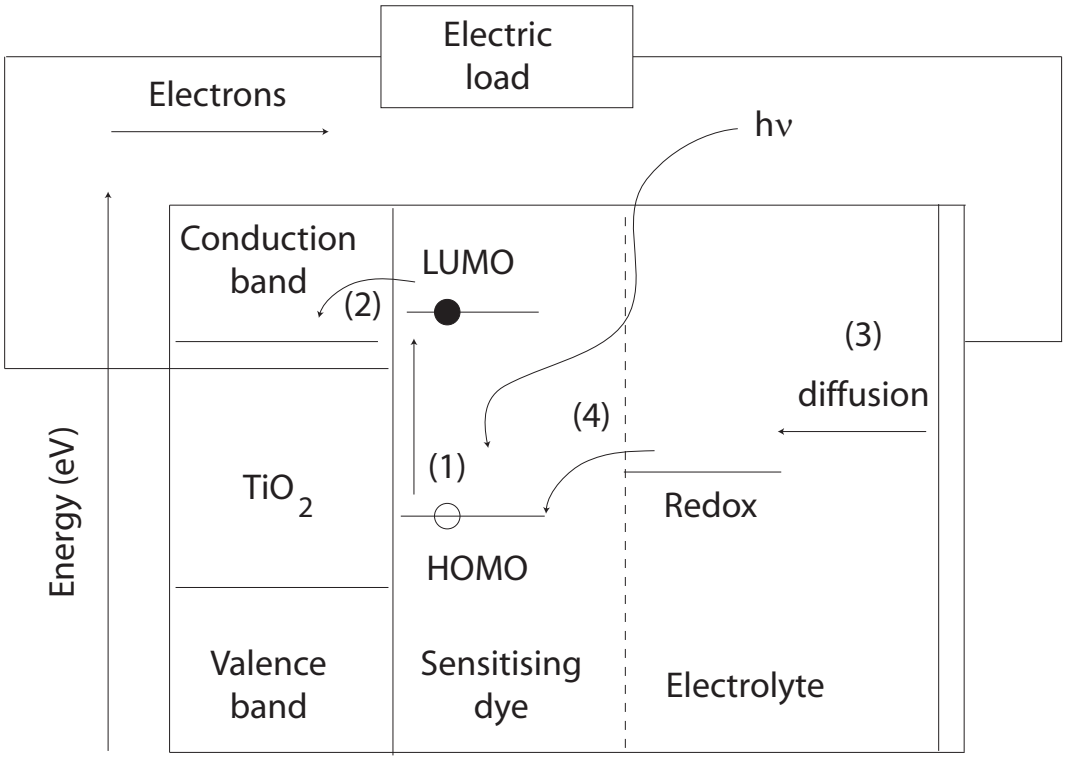

Figure 1.2: A schematic outline of an operating dye-sensitized solar cell. In situation (1) an electron will be excited from the HOMO to the LUMO by the incoming photon. Shortly after in situation (2) the electron tunnels into the conduction band of the TiO_2 substrate. The cathode of the dye-sensitized solar supplies electrons to electrolyte, and the electrolyte diffuses to the dye (3). By a redox reaction the molecule's HOMO is resupplied with electrons from the electrolyte (4). In between step (3) and step (4) the wanted electric load can be placed.

conversion efficiency due to the combination of a high TiO_2 surface area, provided by the porous network that connects the nano-particles, and a dye with ideal spectral characteristics.[12, 13] Unlike the conventional silicon based solar cells, where the silicon plays the role of absorbing the incoming photon, as well as providing the electric field to separate the charge and create a current, the DSSCs are divided into two functions. The photoelectrons originate from a photosensitive dye that is separated from the semiconductor bulk, which solely facilitates charge transport. In Figure 1.2 the schematics are laid out of the operating dye-sensitized solar cell.

Within the dye-sensitized solar cell the nanoparticles are immersed in an electrolyte, usually iodide/triodide and held in place between the transparent cathode and TiO_2 anode. The dye molecules absorb the incoming photon

labelled (1) in Figure 1.2. This absorption promotes an electron from the highest occupied molecular orbital (HOMO) to the lowest molecular orbital (LUMO).[12, 13] The electron tunnels into the TiO_2 substrate. If the anode and the cathode are connected in a circuit the electron will move towards (labelled (2) in Figure 1.2) the anode, thereby creating an electrical current. The consequential hole in the HOMO the electron left behind is filled via a reduction reaction with the electrolyte which is replaced via the cathode, this process is labelled (3) in Figure 1.2. Efficiencies as high as 11% have been achieved using a ruthenium based dye on titanium dioxide nano-particles measured under standard AM1.5G test conditions on solar zenith angle, solar light intensity and cell temperature.[13, 14] This high efficiency is comparable to the efficiency of conventional solar cells.

An intensively studied [15–22] molecule is bi-isonicotinic acid, shown in Figure 1.3A. It serves as a ligand for the highly important dye-molecule cis-bis(isothiocyanato)bis(2,2'-bipyridyl-4,4'-dicarboxylato)-ruthenium(II) commonly known as "N3", shown in Figure 1.3B, which has shown very promising results toward the establishment of high efficiency dye-sensitized solar cells. The N3 molecule forms a strong bond to the TiO_2 via deprotonation of the carboxylic acid group in the bi-isonicotinic acid ligand forming a 2-M bidentate bond.[16, 23] This chemical coupling allows for the charge transfer to occur between the N3 molecule and the TiO_2 surface in the nano-particles. The bi-isonicotinic acid consists of two molecules, the isonicotinic acid, shown in Figure 1.3C. Beside being a building block for the bi-isonicotinic acid, the iso-nicotinic acid derivative isoniazid is also used in the treatment of pediatric tuberculosis.[24]

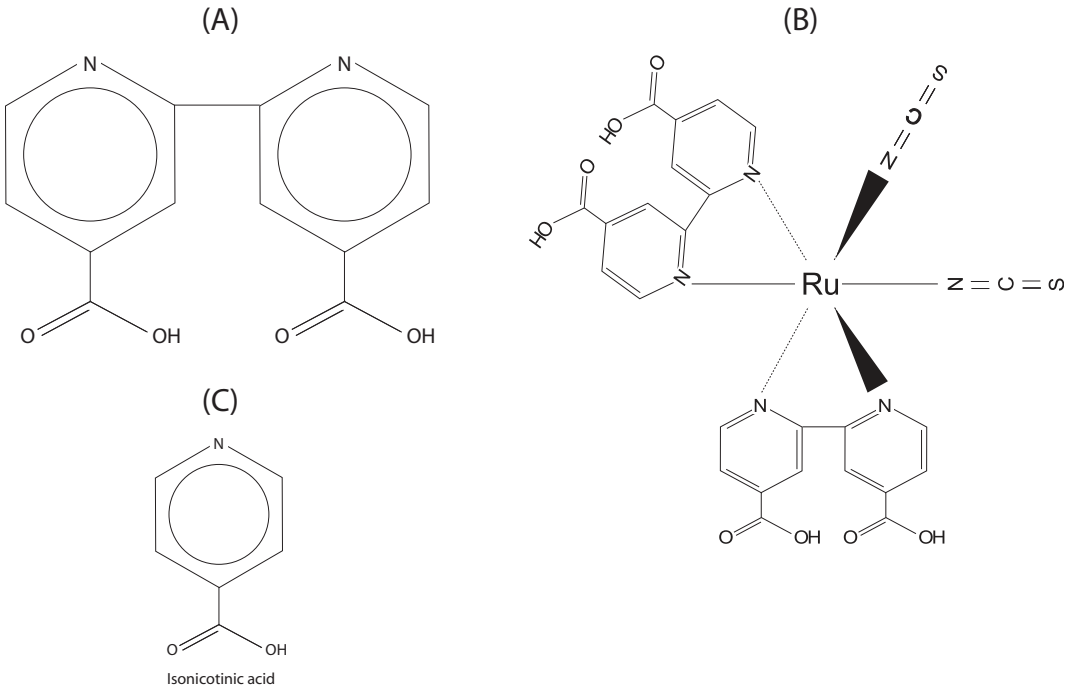

Figure 1.3: A diagram of the (A) bi-isonicotinic acid. The N3 molecule (B) bounds to the TiO_2 surface via the bi-isonicotinic ligand. The bi-isonicotinic consist of two isonicotinic acid (C) molecules.

The bonding and charge transfer properties of N3, and its constituent ligands, on TiO_2 have been studied within our research group using synchrotron-based radiation. A previous experiment by Schnadt *et al.*[18] used a combination of resonant photoemission spectroscopy (RPES) and X-ray absorption spectroscopy (XAS), both using synchrotron based radiation, to investigate bi-isonicotinic acid on rutile $TiO_2(110)$ to find a charge transfer time of under 3 femtoseconds. In a study within our group[25] the synchrotron-based technique of resonant inelastic X-ray scattering (RIXS)[26] has been employed where a similar charge transfer transfer time of sub-3-femtoseconds is found. In this study we revisit the system of bi-isonicotinic acid on the rutile $TiO_2(110)$ surface with the technique of RIXS, but this time with a much higher resolution. We do confirm the sub-3-femtosecond charge transfer time, but a range of new properties with the bi-isonicotinic acid are found. This is addressed in Chapter 5

Photon-induced electron transfer has taken place on earth for millennia in a

number of different biological systems. Of particular relevance is the large scale light-harvesting capabilities of photosynthesis. In 1959 that Kallmann and Pope [27] observed the photovoltaic effect from a synthetic organic compound, anthracene, in their laboratory, which has led into a vast variety of studies within photovoltaic organic compounds.

In the 1990s a number of research groups started creating conjugated porphyrin oligomers.[28–33] for using them as models for natural photosynthetic systems. An oligomer molecule is by the IUPAC definition: "A molecule of intermediate relative molecular mass, the structure of which essentially comprises a small plurality of units derived, actually or conceptually, from molecules of lower relative molecular mass." A conjugated system is the interaction of one p-orbital with another across an intervening σ-bond.[34]

The name "porphyrin" is derived from the Greek "porphura" meaning purple, and all porphyrins are intensely coloured.[35, 36] One of the highly important porphyrins is the one of haem, consisting of a Fe^{2+} ion in the centre of a large heterocyclic organic ring. Haem is a component of the red pigment hemoglobin in blood cells. In our studies the iron ions have been replaced with a Zn^{2+} ion. The oligomer has been bend to form a ring of 12 zinc porphyrin, hereafter referred as c-**P**12. The analogue linear porphyrin polymer has a center-to-center spacing of 1.33 nm,[37], and the c-**P**12 molecule has a diameter of 47 Å measured by small angle X-ray scattering.[38] A ball-and-stick model of these butadiyne-linked nano-rings with 12 porphyrin units are shown in Figure 1.4A. The solubility of the nanorings are promoted by the octyloxy side chains, which are attached to the porphyrin macrocycle via aryl groups. A diagram of the c-**P**12 molecule is shown in Figure 1.4B The chemical formula of the c-**P**12 is $C_{816}H_{984}N_{48}O_{48}Zn_{12}$ with a relative molecular wight of 13017.4. The zinc porphyrin derivative, zinc protoporphyrin shown in Figure 1.4C is known in medicine and biology where it is used as screening for lead poisoning, iron deficiency and other medical conditions.[39–41]

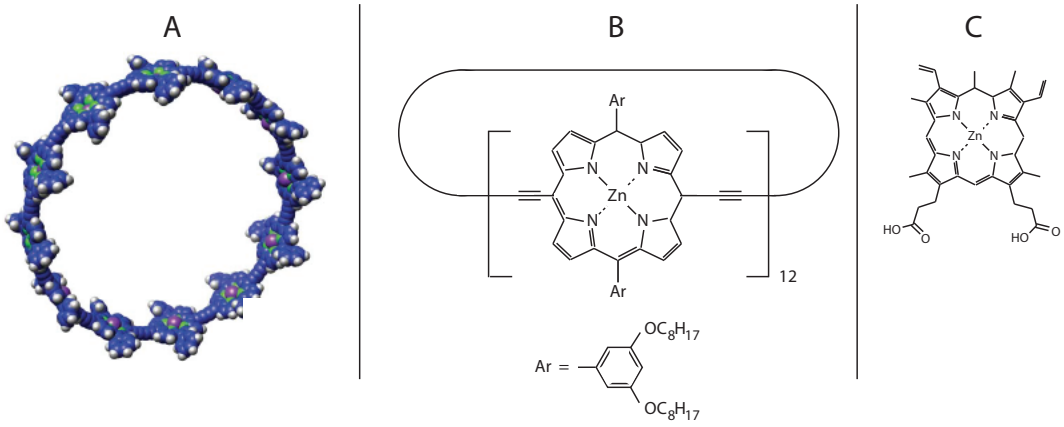

Figure 1.4: (A) Ball-and-stick representation of the c-**P**12 molecule. (B) The chemical structure of c-**P**12. (C) The chemical structure of zinc protoporphyrin. The ball-and-stick representation has been reproduced from [38].

Since the mid-1990s interest in π-conjugated systems has steadily increased. One of the motivations for this is that π-conjugation produces a small gap gap between the highest occupied molecular orbital (HOMO) and lowest unoccupied molecular orbitals (LUMO). This small gap can help to enhance the conductivity of the molecular system. Furthermore they have shown a great importance in application such as light-emitting diodes,[42–44] thin-film field effect transistors,[45–47] photo-voltaic cells,[44, 48–50] sensors,[47, 51, 52] displays[53, 54] and data storage devices.[47, 55] Devices that are polymer-based are flexible and lightweight and come in almost any size and shape that may be desired.[4, 49] In contrast to their inorganic counterparts, the production process is often cheaper, more environment-friendly and energy-efficient.[4, 5] In the work presented here, the type of porphyrin-derived nano-structure, polymer nanorings have been used.[38, 56] These new materials also show the delocalization of the molecular orbitals and their similarity to biological light-harvesting complexes LH1 and LH2 have enforced their popularity within the research communities.[57, 58] These porphyrin-derived nano-structures are produced by the Vernier self-assemblies synthesis. This approach enables precise control over of the number of porphyrin groups with in cyclic polymer nanorings, where 24 porphyrin units have been made and studied[37, 38, 56]

and as many as sixty porphyrin units have been suggested.[59]

Within the realms of nanoscience it is not only the π-conjugated systems and dye sensitized solar cells which have attracted attention. The research towards nanoscale storage devices[60], spintronics,[61] and quantum computation[62–64] have recently focused on single molecule magnets, SMMs. Below a certain, known as the blocking temperature, the SMMs are able to retain magnetization at the molecular level.[65–68] These compounds currently elicit sustained research activity as their magnetic properties make them the ultimate storage bits of molecular magnetic memory, and as quantum objects they are envisioned as qubits for quantum computers. These hybrid molecules are made from metal ions bound together by various organic ligands, and numerous types of compounds have been reported to show SMM behavior: polymetallic cages,[69] 4f coordination compounds,[70, 71] and oxometallaclusters.[66–68, 72] Despite its poor stability against water and temperature, the so-called "Mn_{12}(acetate)" compound $Mn_{12}O_{12}(CH_3COO)_{16}(H_2O)_4$ is probably the most studied SMM for at least two reasons: its synthesis is cheap and easy, and it long held the record for the highest blocking temperature.[66] The Mn_{12}(acetate) magnetized at 2 K will keep 40% of its magnetisation after 2 months and by lowering the temperature to 1.5 K this will take 40 years.[73] Recent studies of the Mn_{12}(acetate) have shown that electrospray deposition[74–77] and tip-deposition[78] are ideal for deposition of the highly fragile manganese cluster on to various surfaces. The $Mn_{12}O_{12}$ core cluster is shown in Figure 4.1 in Chapter 4.

The possibility of the formation of a dodecamanganese (III, IV) cluster was proposed as early as 1921 by Weinland *et al.*[79] The ionic species of manganese with valence of +3 and +4 are found to be red and brownish black, respectively.[80] The mixed valence compound has the colour of reddish black. Manganese(III) and manganese(IV) are known to be quite powerful oxidizing agents. The manganese(III) are prone to disproportionation and can easily form manganse(II) and mangenase(IV) in solution. Disproportionation is a type of redox in which a species is simultaneously reduced and oxidized to

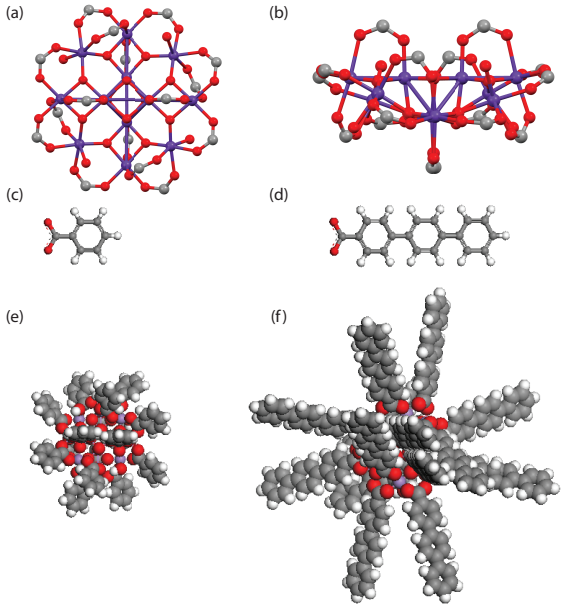

Figure 1.5: (a) and (b) views of the dodecamanganese (III, IV) cluster. The carbon within the carboxylate anchor of a ligand is shown as a grey sphere. Eight of these are shown around the perimeter of the molecular view in (a) and four above and below the molecular view in (b). The purple and red spheres represent the manganese and oxygen within the cluster respectively. The two ligands benzoate (c) and tpc (d) are also shown. The representations of (e) $Mn_{12}(benzoate)_{16}$ and (f) the larger $Mn_{12}(tpc)_{16}$ are shown in the space-filling representation.

form two different products. The most stable oxidation state of manganese is manganese(II), subsequently forming MnO_2.[81] The MnO_2 compound has been known from early human history as the red pigment in cave paintings[82] up to present day where it is still used as a pigment in ceramics and glass-making, but the main application of MnO_2 is found in the battery industry where it is a key component in dry-cell batteries.[80] The mixed valence dodecamanganese (III, IV) core contains four Mn^{4+} ions at the core and eight Mn^{3+} ions around the periphery. The four Mn^{4+} ions each have a down spin of 3/2 while the eight Mn^{3+} ions each have a spin up of 2, leading to a total spin of 10, giving rise to unusual magnetic relaxation properties.[67, 83] The Mn^{3+} ions show a strong Jahn-Teller distortion, which differentiates them from Mn^{4+}.[84] The large magnetic anisotropy D results in a reversal magnetization

barrier with the height of $-DS^2 = 6$ meV for the bulk. This allows the production of very long spin relaxation times at low temperatures.[85] Many studies have shown that the immobilization of the manganese clusters at surfaces are difficult, since their fragile nature is easily altered, resulting in changes in their magnetic properties.[74, 75, 86–89] In particular the thermal instability of the manganese cluster hinderers a successful in-vacuo deposition by thermal evaporation. In our studies we have used ultra high vacuum electrospray deposition, as described in Chapter 3. The most widely studied example[74, 76] is $Mn_{12}O_{12}(CH_3COO)_{16}(H_2O)_4$, herein referred to as Mn_{12}(acetate)$_{16}$, but the carboxylate ligands can be modified by conventional wet chemistry techniques, such as direct synthesis from the appropriate carboxylate reagents[90] or ligand exchange.[85, 91, 92] In this study we have replaced the acetate ligands by benzoate and terphenyl-4-carboxylate ligands, as shown in Figure 4.1(e) and Figure 4.1(f), in order to investigate the effect that modifying the protective shell around the magnetic core of the SMM has on preventing a change in the oxidation states of the Mn atoms when adsorbed on a surface. The results of these studies are presented in Chapter 4.

The rutile TiO_2(110) single crystal was employed for the investigations of the porphyrin nanorings, the single molecule magnets and the bi-isonicotinic acid. The rutile (110) surface is the most stable of the single-crystal surface for the TiO_2.[93] The structure of the rutile crystal is displayed in Figure 1.6. The surface titanium atoms are either five-fold or six-fold coordinated, and the surface oxygen atoms can be divided into in-plane and protruding on-top (bridging) species. The presentation follows that of Vogtenhuber *et al.*[94]

In the studies of single molecule magnets and the c-**P**12 molecule, the Au(111) surface has also been used. A schematic model of an Au(111) surface is shown in Figure 1.7

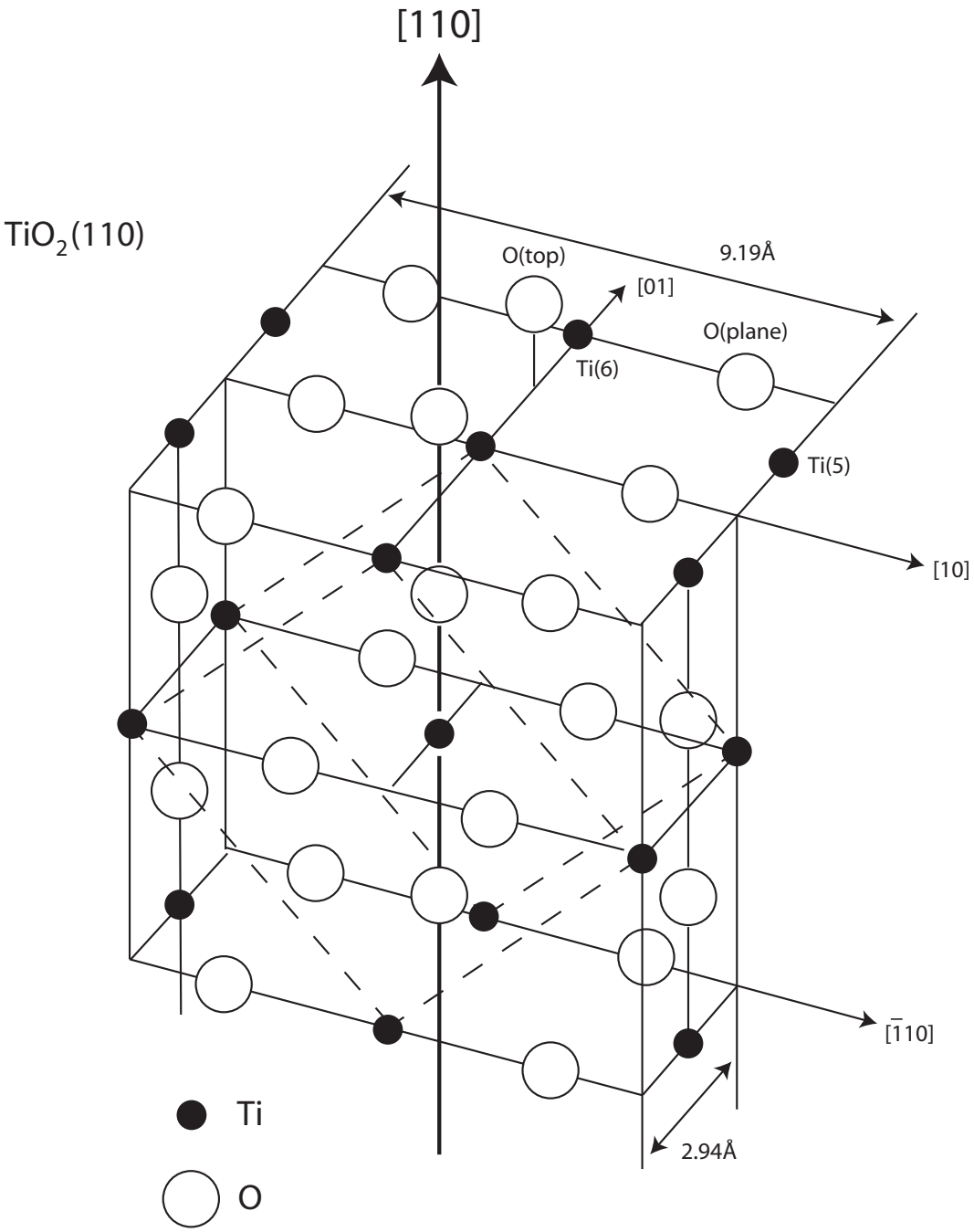

Figure 1.6: Geometrical structure of rutile TiO_2. The bulk unit cell is indicated by the dashed lines, while the (110) surface unit cell is given by the rectangle on top with dimensions 9.19Å$\times$ 2.96Å. The surface unit vectors are given. The dashed lines marks the rutile bulk unit cell. The presentation follows that of Vogtenhuber *et al.*[94]

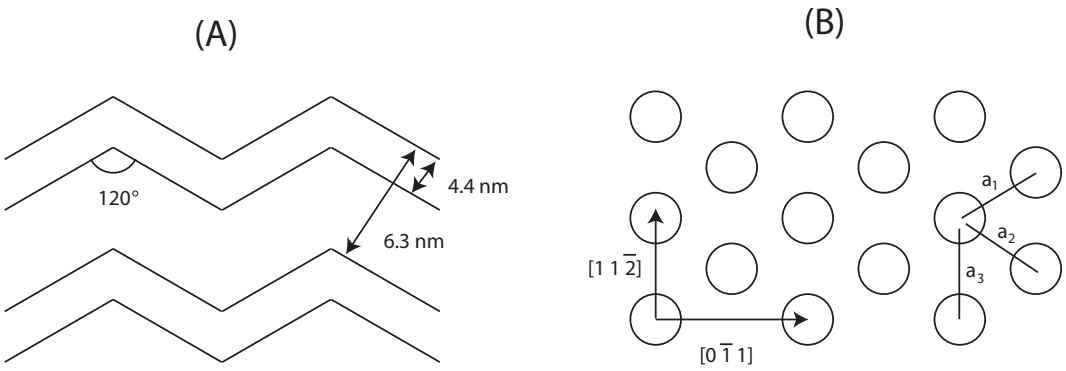

Figure 1.7: Schematic showing the herringbone reconstruction of the Au(111) surface. (A) Spacing and directions of the double bright lines of the herringbone reconstruction. (B) Atomic position of the Au atoms on the surface, $a_1 = a_2 = 2.85$ Å and $a_3 = 2.75$ Å which correspond to a lateral compressing of 4.55% of the [0 $\bar{1}$ 1] direction compared to the bulk.

In the bulk, gold has a face centred cubic, FCC, structure. However, the (111) plane of the surface reconstructs to give a "herringbone" structure with a unit cell $22 \times \sqrt{3}$ larger than that of the bulk.[95] This "herringbone" pattern can be observed using scanning tunneling microscopy, STM, and is present as pairs of bright, parallel lines which "zig-zag" their way across the surface. The reconstruction of the Au(111) surface is unusual as gold is the only coinage metal to undergo this process.

The top layer of atoms in the Au(111) plane are laterally compressed along the [0 $\bar{1}$ 1] direction which allows 23 rows of atoms to fit into the space normally occupied by on 22 rows in the bulk configuration. The compression leads to alternate domains of FCC and hexagonal close-packed, HCP, structure. Atoms which reside the boundaries between these domains sit in a energetically unfavourable position and appear brighter in a STM scan by approximately 0.2 Å.[95] Due to the three-fold rotation symmetry of the (111) surface the domain boundaries, represented by rows of raised atoms, may change direction with an angle of 120° relative to one another. This results in the classic "herringbone" pattern illustrated in Figure 1.7.

Chapter 2

Charge Transfer Theory

2.1 Molecule to molecule charge transfer

One of the major issues in molecular electronics is charge transfer between the molecules and the substrate. By illuminating the charge transfer dynamics between two molecules with no outside forces present a key stepping stone toward the understanding of charge transfer dynamics can be laid. In this simplified situation the exchange of electrons between two discrete molecular states will be covered. When this two-state situation has been elucidated the scheme will be expanded by introducing a surface to cover the extra electronic states that thereby need to be included.

We will start with the picture put forward by of May and Kühn[96], where charge transfer is defined as a spontaneous charge redistribution between two states via tunnelling processes. The charge is considered to remain in a bound state of the system, tunnelling between different physical regions and not transferred through activation above the ionisation threshold. The time-dependent solution to this problem becomes simple when approximating the electron transfer between the two states as a tunneling between two identical square-well potentials corresponding to the molecular states. This coupled system obtains two new eigenstates from the initial two individual eigenstates.[97] In Figure 2.1 this situation is shown. The wave functions within the wells will overlap each other. This overlap corresponds to the energy difference between

the two new eigenstates and is twice the electronic coupling. This becomes the tunneling matrix element and can be described by the an eigenfunction of the associated Hamiltonian.[98]

This scenario is time-independent and will have requirements of a stationary system with no charge. It does not take into account that the thermal motion of the system provides constant changes in the intermolecular distances and thereby changes the forces between the molecules which causes changes in the energy levels within the system.[97] The results of these constant changes of the system is that tunneling only can occur for short periods of time when the states are in resonance. The time-dependent Schrödinger equation[99] can be used to evaluate the actual rate of charge transfer:

$$i\hbar\frac{\partial\Phi}{\partial t} = \hat{H}\Phi \tag{2.1}$$

Setting three initial conditions of t = 0, the two energy levels being the same in each well and placing the electron in the donor well, the solution to Equation 2.1 becomes:

$$\Phi(x,t) = \exp\left(-\frac{i\epsilon t}{\hbar}\right)\cdot \left[\cos\left(\frac{Vt}{\hbar}\right)\phi\left(x+\frac{d}{2}\right) - i\sin\left(\frac{Vt}{\hbar}\right)\phi\left(x-\frac{d}{2}\right)\right], \tag{2.2}$$

where only a single state, $\phi(x,t)$ is considered for each well. The term ϵ is the site energy of the acceptor and d is the distance between the two quantum wells.[97] By increasing time the oscillations of the electron distribution between the two wells, having the period of, $\hbar/V$, would be damped when the motion of the atomic nuclei in the molecules drives the electronic levels out of resonance. The electronic coupling is thereby decreased and the energy levels are changed, thus equation 2.2 becomes:

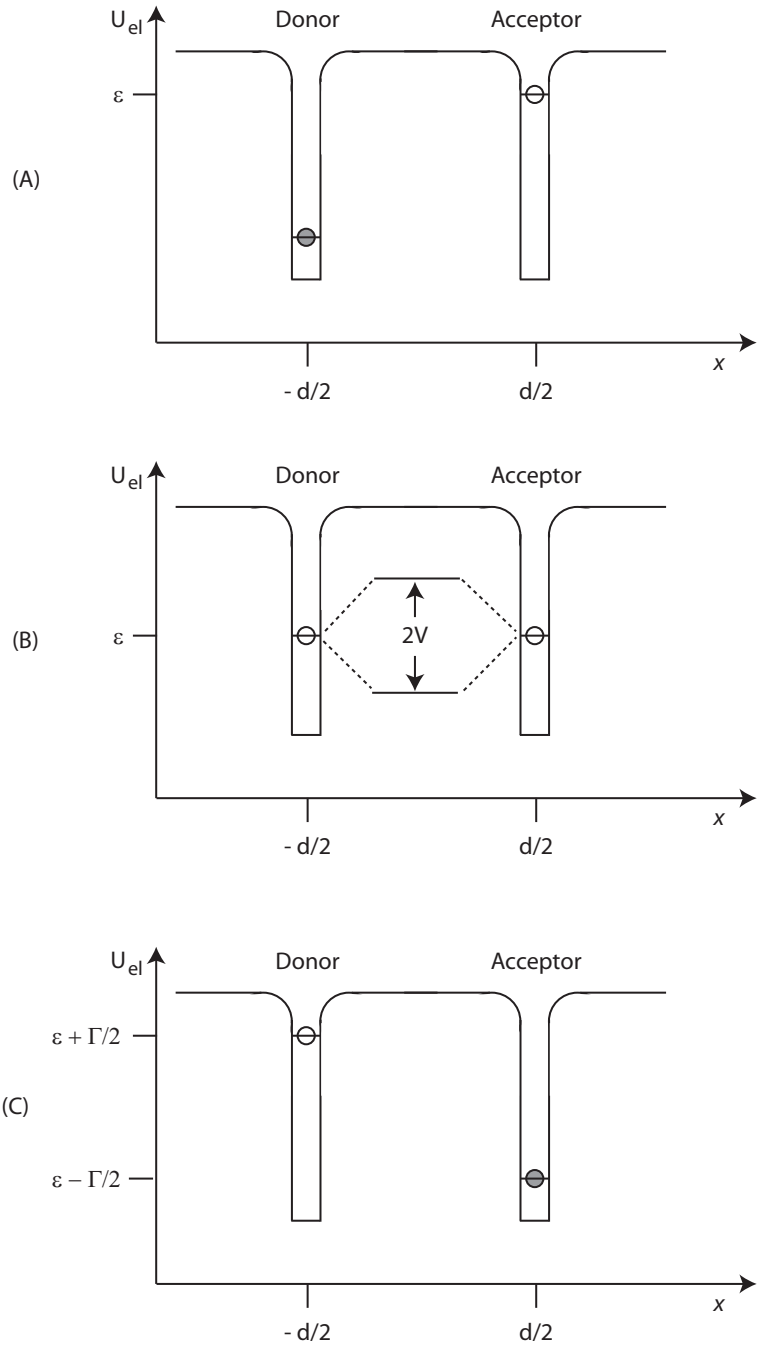

Figure 2.1: Square-well model representing the mechanics of charge transfer between two molecules through the mixing of discrete electronic states between the molecules. The displacement of the energy levels from resonance is caused by the motions of the nuclei in the molecules. In the top diagram, (A), the electron is localized on the donor molecule. In diagram (B) the two energy levels are at resonance, producing a mixed electronic state and allowing charge distribution between the two molecules. In the bottom diagram, (C), the levels have become out of resonance and the electron has become localized on the acceptor

$$\Phi(x,t) = \exp\left(-\frac{i\epsilon t}{\hbar}\right) \cdot \left[\left(\cos\left(\frac{t\Gamma}{2\hbar}\right) + \frac{i\Gamma}{\Delta}\right)\phi\left(x+\frac{d}{2}\right) - \left(\frac{2i\Gamma}{\Delta}\sin\left(\frac{t\Delta}{2\hbar}\right)\right)\phi\left(x-\frac{d}{2}\right)\right] \quad (2.3)$$

The variable Δ is defined according to $\Delta^2 = \sqrt{(\Gamma^2 + 4V^2)}$, where Γ is the energy mismatch between the equivalent isolated wells and all other quantities are as their previous definitions. As time increases, the electron is increasingly more likely to be found at the lowest energy site.[97] When the energy difference caused by nuclear fluctuations is much greater than the electronic coupling, the electron becomes localized at the lower energy site. The acceptor site ends up being lower in energy due to the movement of the electron. The electron distribution at the initial site is negligible and the electron can be said to have transferred from the donor site to the acceptor site.

An important massage in this discussion is that the decoupling of the molecules and the re-localization of the electron onto the acceptor molecule is the result of the energy gap arising from the thermal motions of the nuclei in the molecules. Providing the outcome that the charge transfer is dependent on the two competing processes of thermal nuclear motion and electron tunneling. The electron tunneling is dependent on the amount of coupling between the two molecules which in turn is dependent on the amount of separation between the molecules and the potential barrier. In the case of a strong electronic coupling the tunneling of the electrons usually occurs before the damping of the resonance by the nuclear motions sets in. The consequence of the charge delocalisation is that the surrounding medium becomes polarized with the resultant nuclear motion creating an energy gap between the two states that disrupts the resonance.[97] The upper limit for electron transfer is dictated by the nuclear relaxation and is called the adiabatic limit, which can be on picosecond time scale for metals and organic molecules.[97, 100, 101]

In the case of weak coupling, the motions of the nuclei disrupt the resonance between the two molecules before the electron has had time to tunnel between them. The electron very rarely transfers to the acceptor molecule. The elec-

tron transfer-time is determined by the probability of the system maintaining resonance between the molecules. This is called the non-adiabatic limit for charge transfer.[97]

The three factors playing the main role in the determination of charge transfer are the motion along the nuclear coordinate, the energetics and the electronic coupling. The motion along the nuclear coordinate is that which modulates the electronic energy levels and ultimately stabilises the charge in the acceptor state. This motion will define the barrier attempt frequency. It also determines the rate of passage through the transition state and the speed of charge localisation. To understand this requires knowledge of the shape of the potential energy surface of at least the dominant nuclear modes. The energetics simply pertains to the height of the barrier to attaining resonance, in order to cross from the reactant to the product surfaces. The probability of gaining the energy required to reach the top of this barrier is well described by Boltzmann statistics.[97] The energetics and nuclear coordinates are grouped as nuclear factors. Where the last electronic coupling is grouped as electronic factor, since it describes the degree of electronic wave-function overlap between states. By this the frequency at which charge transfer occurs once the transition state has been reached is obtained. This can be related to the matrix tunneling element and is highly dependent upon the physical separation of the states.

The potential energy diagram for the charge transfer between two molecules is shown in Figure 2.2 with the potential energy measured for a variety of nuclear reaction coordinates. A real potential diagram would be highly complex, but this is a reasonable approximation to describe the situation. The system has the lowest potential energy in position A, with the nuclear configuration of the electron being located on the donor. A similar situation is found in position C, but here the electron would be located on the acceptor. The position B is found in between A and C, and describes the situation when the two molecules' electronics levels are in resonance, allowing charge redistribution due to the mixed electronic state.

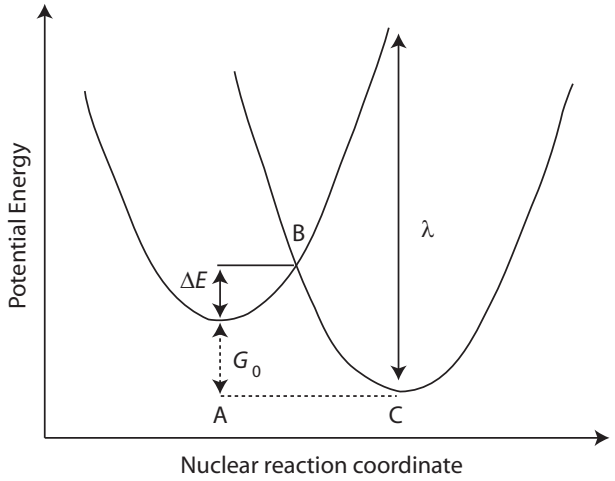

Figure 2.2: Potential energy diagram for movement along the electron transfer reaction coordinate. Position A and C is the lowest potential energy for the electron being on the acceptor and donor, respectively. At the intersection of the two potential energy parabolas, lies position B where the electronic states are in resonance and where electron transfer can take place. The difference in energy between the acceptor and the donor sites is G_0. The energy of charge transfer at site B is ΔE, and the λ denotes the reorganization energy required to transfer the electron.

The idea of electron transfer between two molecules was first proposed by Rudolph A. Marcus in 1956[102] and forms the cornerstone of homogeneous charge transfer theory. It was derived in response to the failure of Eyring's transition state theory to determine electron transfer in the situation where there is no structural change in the molecules. Marcus' theory specifically deals with the one electron redox reaction.[102]

$$D + A \rightleftharpoons D - A \rightleftharpoons D^+ - A^- \rightarrow D^+ + A^-$$

The classic example used by Marcus for this was iron in a solution[102–104] but electron transfer reactions involving two molecules are also very common in biological systems.[101] This means that the energy difference between point A and point B in Figure 2.2) represents the amount of energy required to arrange the atoms to bring the donor and acceptor into resonance. In other words, this is the activation energy in the classical potential energy picture used for elementary chemical reactions. The probability for attaining this condition comes from using Boltzmann statistics.[105] The movement into position C is influ-

enced by the explicit exothermicity of the charge transfer.[105] If the electron being on the acceptor has a lower potential energy than when it is on the donor, then charge transfer to the acceptor is much more likely. This difference in potential energy is mainly due to the difference in the relative energy positions of the highest unoccupied molecular orbital (HOMO) of the donor and the lowest unoccupied molecular orbital (LUMO) of the acceptor.[97] From the Arrhenius equation the charge transfer rate, k_{CT} can be written as:[105]

$$k_{\mathrm{CT}} = A \exp\left(-\frac{\Delta E}{k_{\mathrm{B}} T}\right), \tag{2.4}$$

where ΔE is the activation energy shown i Figure 2.2. In the adiabatic charge transfer case k_{CT} will take the value of 1, and less than 1 in the non-adiabatic charge transfer case. The term k_{B} is the Boltzmann's constant and T denotes the temperature. The prefactor A is given by:[97]

$$A = \nu_{\mathrm{eff}} \exp\left(-\beta(d_0 - d)\right) \tag{2.5}$$

where ν_{eff} is the effective frequency of sampling coupled to that reaction coordinate. The damping of the electronic wave function in the barrier region separating the the two molecules is denoted by the constant, β. The term d_0 is the direct contact distance, which is the optimal position for charge transfer.[97] We see from Equation 2.5 that with increasing distance, d, between the molecules the probability for charge transfer decreases, as we would expect.

Marcus[106] formulated a more explicit expression for the rate constant in the non-adiabatic limit, from which modern day theory has developed. The nuclear motions are treated classically and are assumed to lie within a harmonic approximation. A simple one-dimensional semi-classical derivation of his result is relatively straightforward. In this model, where two molecules are considered classically as two polarized spheres of charge in a solution, any amount of charge can pass between them. The Gibbs free energy, G, required to change the nuclear configuration to move a specific amount of charge, ΔE, was found to be:[103]

$$G = \left(\frac{1}{r_1} - \frac{1}{r_2} - \frac{1}{R}\right)\left(\frac{1}{\epsilon_{op}} - \frac{1}{\epsilon_s}\right)(\Delta E)^2, \tag{2.6}$$

where r_1 and r_2 are the radii of the two spheres, R is the separation between the two spheres, with ϵ_{op} and the ϵ_s being the high frequency dielectric and static constants of the medium respectively. Having a set distance between the molecules a simple harmonic approximation is thereby valid[103], but in reality the term ΔE is associated with the probability of electron transfer, not the actual amount. Nevertheless this model can be shown to portray a highly accurate picture both experimentally[107] and by using computer simulation.[108]

Using the simple harmonic model, the nuclear potentials can be considered as two intersecting parabolas.[104] This approximation is the reason for using parabolas in Figure 2.2. Assuming the bottom of the acceptor parabola in Figure 2.2, at position A, has the co-ordinates (0,0), and that the donor parabola at position C in Figure 2.2, has the coordinates (a,b); the equations of the two parabola are $y = x^2$ and $y = (x-a)^2 - b$. The y value at the intersection of the two parabolas is ΔE, which is the activation energy. To find the intersection, we must combine the equations to give $x^2 = x^2 - 2ax + a^2 - b$. By employing algebra and using $y = x^2$ we obtain $y = \frac{\left(a^2-b^2\right)^2}{4a^2}$ The coordinate b is $-\Delta G_0$, which is the potential energy difference between the electron being at the acceptor site or the donor site, and a^2 is λ, the amount of energy in the medium it would take to reorganize the nuclear configuration to allow for charge transfer to occur in the previous charge distribution.[104] This gives us an equation for the activation energy, ΔE of:

$$\Delta E = \frac{(\lambda + \Delta G_0)^2}{4\lambda} \tag{2.7}$$

Having obtained equation 2.5 and equation 2.7 we can combine them with equation 2.4 thus:

$$k_{\text{eff}} = \nu_{\text{eff}} \exp\left(\frac{(\lambda + \Delta G_0)^2 - \beta(d_0 - d)}{4\lambda k_{\text{B}} T}\right) \tag{2.8}$$

As mentioned previously the experimental evidence for the equation 2.8 is strong.[107] Under non-adiabatic conditions the size of the barrier determines the charge transfer rate, since the damping factor β is much smaller than 1. For molecules in solution the coupling is weak, and the charge transfer will therefore occur in the non-adiabatic limit.[97, 98] If strong couplings are present chemical and structural changes to molecules will most likely occur, and in this situation Marcus's theory will not provide a satisfactory answer. The average charge transfer time for two molecules in solution can vary significantly from picoseconds to hours, due the vast range of possible barrier heights.[97]

In the adiabatic limit the frequency of sampling, ν_{eff}, becomes the dominating factor since term $\exp(d_0 - d)$ is close to 1. The outcome of this is that the physical properties underplaning the dielectric relaxation time of the medium will dominate the scenario.

2.2 Incorporating surfaces

In the previous section charge transfer between two strongly localized discrete states placed on two different molecules was discussed. This discussion can be used to elucidate the charge transfer between a molecule and a surface when a solid-state surface in introduced to the system. A solid-state surface is characterized by having its electronic states delocalized and the states can be described by their hole or electron momentum $\mathbf{k}$.[99] The textbook example[99, 109, 110] of describing electrons in a crystalline lattice is by the simple quantum mechanical approach where a free electron wave moving through the solid interferes with a periodic potential with the same periodicity as the crystal lattice. The periodic potential arises from the interaction with the atoms in the potential. The Bloch function describes the one-electron wave function, which has the propagation vector of $\mathbf{k}$ modulated by a periodic potential and takes the form of a plane wave.[99, 109, 110]

$$\Psi_{\mathbf{k}}(r) = \exp\left(i\mathbf{k} \cdot \mathbf{r}\right) U_{\mathbf{k}}(r) \tag{2.9}$$

where $\Psi_{\mathbf{k}}(r)$ is the Bloch function, $U_{\mathbf{k}}(r)$ is the periodic function of the crystal lattice, and $\mathbf{r}$ is the position vector of the atoms in the lattice as the crystal momentum. The propagation vector $\mathbf{k}$ characterizes the translational symmetry of the periodic potential with $\hbar\mathbf{k}$ and is a periodic function of the crystal lattice.[99, 109, 110] The Bloch function is a solution to the Schrödinger equation, and provides a range of forbidden and allowed energies.[99, 109, 110] If the propagation vector $\mathbf{k}$ takes a complex form the solutions to the Schrödinger equation become forbidden energies, and allowed in the real case. This approach is called the nearly-free electron model, and works best when the individual atoms interact very strongly and the potential energy of an electron is relatively small compared to its total energy.[97] This leads to smaller energy gaps and works well for metals with fewer electrons and semiconductors with small band gaps.

The approach of assuming that the wave function of the crystal is related closely to the atomic wave function is called the tight-binding approximation.[99, 109, 110] The energy levels of the solid will be similar to the discrete energy levels of the atoms at large interatomic distances. The discrete energy levels will spilt into a new set of energy levels, due to the overlap between the atomic orbital when they are brought together. When a bulk solid is present, hence a large number of atoms, the energy levels form a continuum with forbidden energy gap that are related to the original atomic levels of the atoms in the crystal. The tight-binding approximation becomes a powerful tool when insulators and transition metals are investigated, since here the allowed bands are smaller and have large energy gaps. The split into a new set of energy levels provides the forming of molecular orbitals when molecules are present.[97, 99, 109, 110]

The same result is obtained by both approaches, since they provide the knowledge of energy gaps which electrons can not be transferred into. Depending on where the Fermi energy is located the material is either semi-conducting or a metal, and by the Pauli exclusion principle the electrons will fill the energy levels up to the Fermi energy, meaning only a certain amount of electrons are allowed in each orbital.[99, 109, 110] The electrons can not move freely

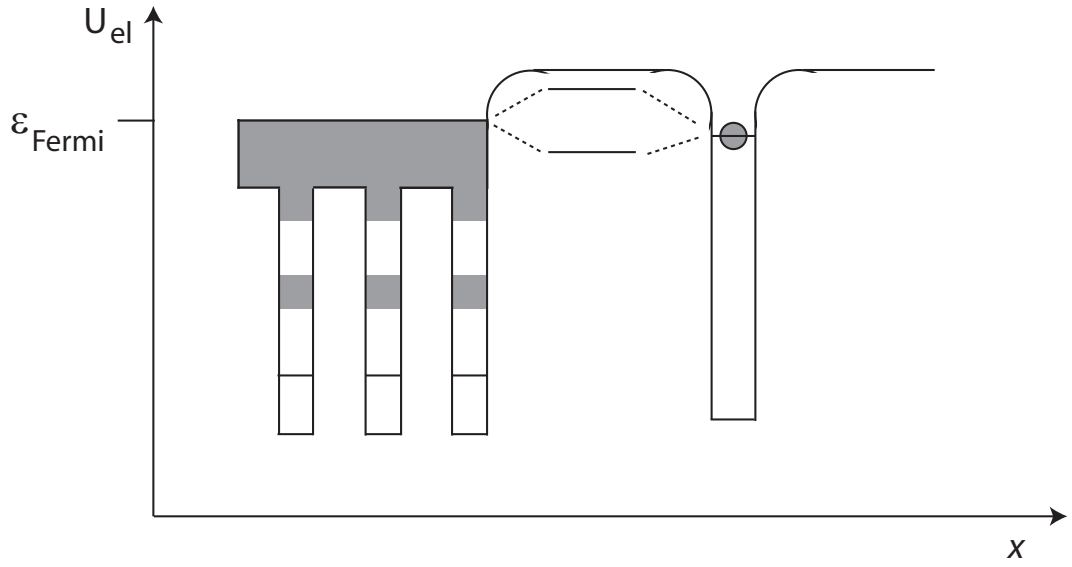

Figure 2.3: Quantum well diagram similar to Figure 2.1 for interfacial electron transfer. It shows the mixing of the molecular discrete state with the valence band orbitals of the solid state surface.

if the Fermi energy is located within the energy gap, and external energy is needed to promote the electrons into a conduction band above the energy gap. At room temperature and with a large gap, very few electrons will have the energy to be promoted to the conduction band, hence the material will be an insulator. In the case where the Fermi level lies within the allowed band, the electrons near the Fermi level need only minimal thermal energy to become free to move around the material.

When handling charge transfer between surfaces and molecules one must take all these different systems into account. A somewhat simple approach is to consider the problem by extending the number of atoms that are interacting with the molecules as shown in Figure 2.3. Here the the solid state electronic structure with the wide bands are considered in relation to the electron transfer coordinates. The crystal is formed by a large number of atoms and the valence orbitals produces a band of electronic states. The electronic states of the solid will overlap with some of the wave functions of the discrete molecular orbitals.[111] The distance between the molecule and the surface dictates the mixing of states and the amount of electronic coupling. Similar to the two-molecule situation this will drop off exponentially, and since the molecule

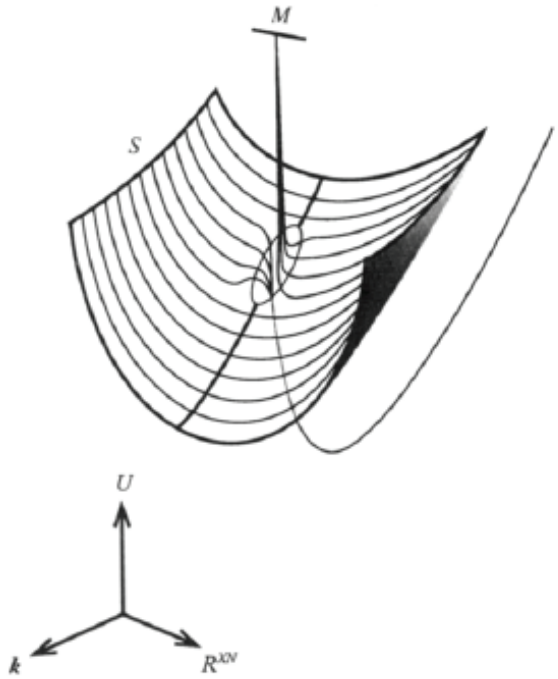

Figure 2.4: Potential energy diagram similar to Figure 2.2 except that it shows the transfer of charge between a solid-state semiconductor and a molecular orbital. The term R^{XN} is the reaction coordinate and represents a cross-section of the multi-dimensional neclear potential energy surface. The molecular and semiconductor states are denoted M and S, respectively. The diagram shows how the large manifold of k-states affects the transition probability at the crossing point. Reproduced from reference [111].

can overlap with many more atomic orbitals the electronic coupling would be significantly larger, compared to the two-molecule scheme.

A different approach would be to let Bloch wavefunctions define the atomic basis, where the wave-function would have the propagation vector $\mathbf{k}$. The sum over all $\mathbf{k}$ states of the lattice will the be the electronic overlap.[111] A diagram of the potential energy surface and the electronic degeneracy at the adiabatic crossing point is represented in Figure 2.4. The enhanced coupling sometimes results in chemical reactions in the strong coupling limit.

Something else that needs to be taken into account is that the number of states also affect the role of the nuclear coordinates. In the case of an electron initially located in a molecular state it will subsequently be transferred into the conduction band of a semiconductor if the system was prepared at the adiabatic crossing point. This electron will delocalize, existing in a mixed state where

it will coherently sample all coupled states. The presence of the vast amount of conduction band states will lengthen the recurrence of the electron on the molecular state. Through electron relaxation processes, such as dephasing and thermalization, the coherence with the initial state is lost on a timescale of the order of 10 femtoseconds[111, 112]. Therefore, the continuum of states is sufficient to localize the electron in the semiconductor and indeed does so faster than the nuclear coordinates which takes of the order of 100 femtoseconds for most molecular species[111, 112], which is significantly faster than the lower limit of picoseconds between two molecules, mentioned above. Conversely, for an electron in the semiconductor prepared at the adiabatic crossing point, charge transfer to a molecular state will require the nuclear coordinate to localise the charge in that state. By assuming sufficient electronic coupling it is the electron relaxation that sets an upper limit to the charge transfer time, when going from molecule to substrate. The nuclear coordinate becomes the upper limit when the charge transfer from the substrate to the molecule. These details have been shown explicitly through numerical simulations performed by J. M. Lanzafame *et al.*[111].

Within the context of solar cells, where injection of the electron from the molecule into the surface takes place, the limit for charge transfer can be much lower that 100 femtoseconds. This have been verified by many experiments, and the electron injection occurs on the lifetime of a core-hole excitation.[18, 23] The very large number of electronic states within the crystal provides a much faster nuclear relaxation compared to the molecule. It is entropically favourable for the charge to move from a discrete molecular species to such a large continuum of states. Therefore the electron is more likely to be found in the substrate than in the molecule during the mixing of resonances. This means that the charge transfer time is not effected significantly by the molecular relaxation. The rate of charge transfer is only dependent on the electronic density of states of the crystal and the electronic coupling.[111] Ultra-fast charge transfer on timescales smaller than the core-hole decay times (< 6fs) are theoretically possible and have been verified experimentally.[18, 23]

Chapter 3

Instrumental Techniques and Methods

When systems are investigated though the absorption and/or emission of photons the general technique that is applied is called spectroscopy. In response to electromagnetic radiation, electrons spectroscopy techniques are those that specifically monitor the emission of electron from a system. The system properties such as chemical compositions, molecular orientations and charge transfer dynamics can be deduced by considering the kinetic energy distribution of the emitted electrons, within the context of the applied radiation. In this section the main spectroscopic techniques and sample preparation methods in the work presented in later chapters are discussed.

3.1 Deposition methods

Thermal evaporation

The deposition of molecules onto solids and surfaces in ultra high vacuum surface is usually done via a Knudsen cell (K-cell).[113, 114] In this technique, the substance for deposition is placed in a crucible, secured by the K-cell's housing. Under vacuum conditions, the crucible is heated by passing an electrical current through a wire coiled around the crucible. The heating facilitate the

molecules to eventually sublime or evaporate, and, if unperturbed, they can travel in a straight line toward the sample surface. Deposition by sublimation is widely used since it gives the user a high degree of control over the deposition rate. The adsorbate can be deposited methodically and gradually on the substrate. Furthermore, as it's a UHV deposition technique, the sample remains clean for UHV measurements. K-cells are for these reasons commonly used in molecular beam epitaxy.[115] Depending on the molecule, it is sometimes possible to make sure there is a monolayer by keeping the surface heated. This relies on the bonding between the surface and the molecule being stronger than the intermolecular bonds. The bi-isonicotinic acid were deposition on the rutile $TiO_2(110)$ by the thermal evaporation. The results of the experiment are found in Chapter 5.

Ultra-high vacuum electrospray deposition

The main drawback of using a thermal evaporation deposition technique comes to light when the intramolecular binding energies are smaller that the energy of sublimation, and dissociation will occur. This is typically the case for larger molecules.[34] To facilitate the deposition of larger molecules and prevent dissociation, an alternative method is required. There are different techniques that addresses this requirement. In the technique of pulsed valve deposition, the molecule of interest is dissolved in a solution. The solution is introduced to the UHV chamber by means of a small aperture valve, in the dimensions of $\approx 50\mu$m diameter. The technique takes its name from quickly opening and closing the valve on the order of a micro-second, and in that time frame exposing the chamber to the solution.[116] A different sublimation technique is that of "rapid heating", where the sample is heated quickly and the molecules may be sublimed before fragmentation occurs, using the fact that the rates of desorption and fragmentation are not the same.[117] In this work the technique of electrospray ionisation has been chosen as the deposition method.

In 2002 John B. Fenn became a Nobel laureate in chemistry with his pioneering work on electrospray ionisation.[118, 119] The technique was devel-

oped to introduce fragile, thermally labile, or non-volatile species into the vacuum for mass spectroscopy analysis.[120] The technique of ultra high vacuum electrospray deposition, UHV-ESD, has with great success been employed to introduce highly fragile and complex molecules for studies using sensitive UHV techniques from scanning tunneling microscopy to synchrotron based techniques [23, 74, 75, 121–129]

The electrospray ionisation process

The electrospray ionisation process may be considered as having three distinct stages.[130] In the first stage charged droplets are formed. These droplets carry the molecules for deposition. In the second stage the solvent will evaporate, and the droplets will start to shrink. In this stage the droplets will undergo fission leading to very small and highly charged droplets ending up as gas-phase ions. The charged droplets are formed by the electrospray ionisation event, which is central to UHV-ESD, and allows molecules which have been suspended or dissolved in a solvent to be volatilised. The solvent is passed through a narrow hollow stainless steel capillary which is termed the emitter. The flow rate through the emitter is in the order of 0.5 mL per hour. If no high voltage is applied to the emitter a droplet of liquid containing solvent and solute will form at the end of the emitter or applying a high voltage the behavior of the system changes radically. Figure 3.1 shows a schematic diagram of the electrospray process.

The counter-electrode is regarded as significantly larger and planar compared to the emitter. With this approximation we can write the electrical field, E_{emitter}, at the tip of the emitter as:

$$E_{\text{emitter}} = \frac{2V_{\text{emitter}}}{r_{\text{emitter}} \ln\left(\frac{4d}{r_{\text{emitter}}}\right)} \tag{3.1}$$

where V_{emitter} is the applied high voltage. The term r_{emitter} denotes the outer radius of the emitter, and d is the distance between the counter-electrode and the emitter, providing a strong electrical field at the tip of the emitter. In

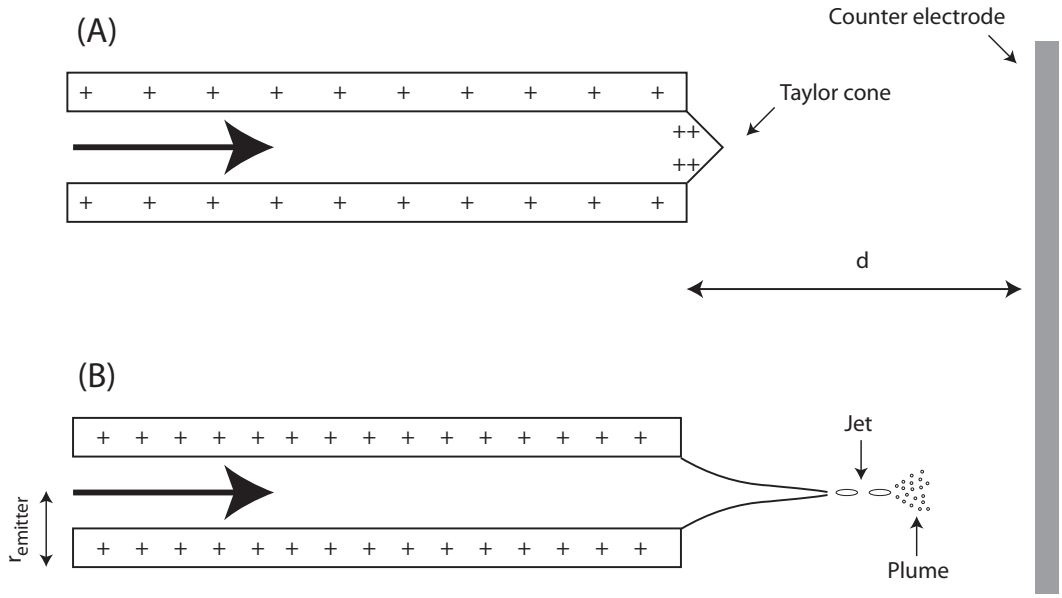

Figure 3.1: Diagram showing an electrospray event whereby a solvent containing the molecule is converted from a liquid into a plume of droplets.

the case of a positive electrical field the negative charged ions will be drawn to the emitter, whereas the positive ions are repelled by the emitter, but they cannot escape the liquid.[130] This repulsion between the positive charged and the emitter results in the formation of a Taylor cone at the end of the emitter.[131] At a certain threshold voltage, the Coulomb repulsion overcomes the surface tension of the liquid and the solvent is emitted in a jet of small droplets from the end of the Taylor cone. This jet is propelled forwards by the emitter's electric field. The jet consist of small droplets that are eventually transferred into the ultra high vacuum, with the initial radius of these droplets increasing approximately in proportion to $(\text{flow-rate})^{\frac{2}{3}}$.[132] The radius of the emitted droplets also increases with decreasing conductivity, implying that the smallest droplets will be obtained for operating conditions with low flow rates and high conductivity solutions.[133] The charge density will meet a threshold called the Rayleigh limit, and the droplets will break up in what is called a Coulomb explosion. The Rayleigh limit is defined as a function of the charge and diameter of the droplet by the equation:

$$q_{\mathrm{R}} = 8\pi\sqrt{\epsilon_0 \gamma D^3}, \tag{3.2}$$

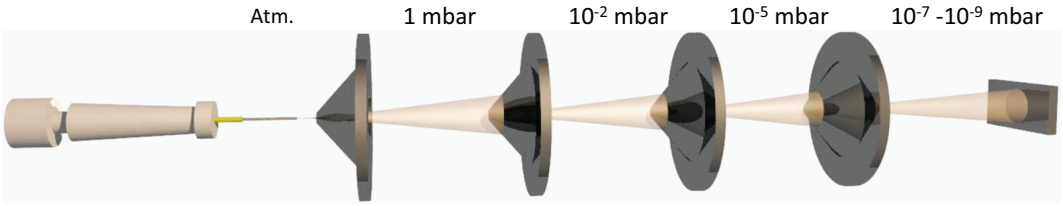

Figure 3.2: Schematic of the electrospray system showing the molecular beam traveling as it leaves the high voltage emitter, passes via apertures through differentially pumped chambers and is incident on the sample. Reproduced with permission from reference [23].

where q_R is the total charge within the droplets, ϵ_0 is the permittivity of vacuum, γ is the surface tension of the liquid and D is the droplet diameter. The Coulomb explosion leads to the production of several smaller droplets. This repeated splitting results, under optimal conditions, in a fine plume of very small droplets, some of which contain only a single molecule. The emitters used in these studies had an outer diameter of 0.32 mm and an inner diameter of 0.1 mm and can deliver 0.1 to 0.30 mL/hour of liquid. In order to reach the sample from the air outside the chamber, the droplets pass through an entrance capillary and through a series of differentially pumped chambers until they impinge upon the sample held in the vacuum chamber. A schematic diagram for this process is shown in Figure 3.2.

The entrance capillary will act as the counter electrode. The surface area of the entrance capillary is still large compared to the emitter as so equation 3.1 will still be valid. To ensure a clear path of travel for the molecules toward the surface, an optical alignment was preformed, by shining a light through the electrospray chamber and into the main vacuum chamber and the light would be reflected on the sample. This procedure also provided the sample's position for deposition. The molecular coverage is controlled by the deposition time. In practice, the molecular flux is not always constant. The molecular flux can be indicated by either the change in pressure in the preparation chamber, which in these studies were in the mid-10^{-7} mbar or by the electronic current on the sample which were in the order of 0.1-0.2 nA. The molecular coverage can be verified by studying the photoemission spectra. The molecules deposited by this technique were the single molecule magnets and the porphyrin nanorings.

For both molecules 1 mg where dissolved in 10 mL of solvent. For the single molecule magnets the solvent where either pure methanol or a 1:1 mixture of methanol-dichloromethane. In the case of the porphyrin nanorings the solvent where a toluene-methanol in a 3:1 concentration. The results of these experiments are addressed in Chapter 4 and Chapter 6, respectively.

3.2 Synchrotron radiation

When charged particles travelling at relativistic speeds change momentum they will emit radiation. Radiation produced by this process is called synchrotron radiation. Synchrotron radiation is extremely intense light and provides a very wide range of electromagnetic radiation from microwaves to hard X-rays. In 1947 the General Electric Research Laboratory in Schenectady, New York[134] reported synchrotron radiation and first considered it as a nuisance. This idea was soon abandoned when it was realized how useful a tool it would be in spectroscopic studies. Even so, it was not before 1981 when the Synchrotron Radiation Source in Daresbury, England was opened as the first dedicated light source. The main synchrotron facilities located around the world are now mostly third generation light sources designed specifically to improve the brightness and polarization of the light.[134]. Currently fourth generation synchrotrons are under development and mainly make use of free electron lasers.[134]

At third generation synchrotron facilities the electrons are accelerated by the synchrotron and they are injected into a storage ring where they circulate in a closed loop, and maintained in their orbit by bending magnets. Along the path of the electrons insertion devices called wigglers and undulators are placed to increase the amount of produced light. This light is projected at a tangent from the ring where it is collected by what are termed beamlines. Undulators consist of an array of magnets that alternate in polarity. When the electrons enter the undulator they travel between these magnets and are forced into a sinusoidal trajectory,[135] where this vast amount of small oscillations

creates cones of radiation. The amount of force the electron beam is exposed to is the only difference between the two types of insertion devices. Where the wiggler introduces a greater deviation of the electron beam, the undulator exposes the beam to much gentler changes, resulting in radiation cones which overlap – interfere – and then add up to coherent light. Through a set of mirrors the synchrotron radiation is funneled down the beamline toward the sample of investigation. Along the path towards the sample the light will meet a monochromator, that enables the selection of a specific energy that will correspond to the measurements in question. This ability to choose particular X-ray energies out of a continuous range is the key advantage of synchrotron radiation, and why it is an invaluable tool for spectroscopy.

Developing of such a vast research facility as a synchrotron light source, which usually take up's large building complexes, is obviously a time consuming highly and costly affair. Commercially available X-ray sources normally produces X-rays by electron bombardment of a metal, which causes a core-hole decay, giving very specific discrete energies. Using synchrotron radiation it is possible to sweep across a range of photon energies, which expands the amount of information that is possible to collect in XPS studies of surfaces and it enables other ways of investigations such as X-ray absorption spectroscopy (XAS), resonant photoemission spectroscopy (RPES) as well as resonant inelastic X-ray scattering (RIXS). Since it is possible to tune the synchrotron radiation to wanted energies it is possible to conduct highly surface sensitive measurements at those facilities. Electrons with high kinetic energy can travel quickly through the materials of investigations and are therefore less likely to interact with the atoms. If the electrons have low kinetic energies they do not have the ability to excite the electron within the atoms and will therefore move easily through the bulk. The mean free path of the electron is dependent on the kinetic energy of the electrons, therefore optimizing the surface sensitively and only record the electrons with a low mean free path guarantees that only electrons originating from the surface will dominate the spectra. In 1979 M. P. Seah and W. A. Dench[136] published what became later known as the uni-

versal curve, a data base for the electron mean free path through solids. From this curve, displayed in Figure 3.12, the optimal surface sensitivity occurs for electrons with a kinetic energy of around 40 eV. With the synchrotron the X-ray energy can now be set at a 40 eV above the binding energy peak that we wish to observe. The universal curve is discussed in greater detail in section 3.7

3.3 Photoelectron Spectroscopy

For the investigation and characterization of matter the powerful tool of photoelectron spectroscopy (PES) can be employed. In 1887 Heinrich Hertz[137] reported the effect of light-matter interaction in his experiment on arc discharge in the presence of ultraviolet radiation. In the beginning of the 20^{th} century Albert Einstein used Planck's quantum formalism of the black-body radiation to explain why only photons of certain energy or light with the right frequency could knock electrons out of the matter. He presented his elegant formulation in 1905[138] for which he became a Nobel laureate in 1921. It was given the name of the photoelectric effect and has the general description as of the following equation:

$$E_{\text{kin}} = \hbar\omega - E_{\text{B}}^{\text{v}} \tag{3.3}$$

The term E_{kin} is the kinetic energy of the electron emitted as a result of the photoemission process – a photoelectron. Planck's constants is term $\hbar$ and ω is the radiation frequency. $\text{E}_{\text{B}}^{\text{v}}$ is the binding energy of the electron. The work function ϕ is used to relate the vacuum level to the Fermi level of a solid. This is highly useful for metals, but ϕ is not necessarily explicitly included in equation 3.3. Thus the interpretation of equation 3.3 can be as follows: An electron from the matter can only be excited if the incident photon has an energy of $\hbar\omega$ that is greater than the binding energy of the excited electron. If monochromatic radiation of known energy is used for production of photoelectrons, equation 3.3 allows to establish a unique relation between the

kinetic energies of the photoelectrons and the corresponding binding energies, which is the basis for photoelectron spectroscopy. Using Koopmann's Theorem, that assumes that the the experimental measured binding energy is directly related to the orbital energy of the emitted electron, allowing a deduction of the approximate electronic structure of the sample. If the binding energy is found with respect to the Fermi level, $E_{\mathrm{B}}^{\mathrm{F}}$, then Equation 3.3 takes the form:

$$E_{\mathrm{B}}^{v} = E_{\mathrm{B}}^{\mathrm{F}} + \phi \tag{3.4}$$

In the experimental situation it is often easier to reference the binding energy to the Fermi level rather than the vacuum level. The Fermi level acts, at least for metals, as a reference point in the XPS spectrum since it is the highest occupied energy state seen in the spectrum. If one were to use the vacuum level as a reference point knowledge of the experimental systems work function, ϕ, is required.

Figure 3.3 is a diagram showing the photoemission process and other consequent processes. Starting out in the ground state all the electronic energy levels below the Fermi level are filled. A photoelectron can be emitted if a photon of sufficient energy is incident upon the system. The probability of absorption of the photon depends on polarisation and the magnitude of the photon's electric field vector, the initial and final electronic states of the atom or molecule, and the energy density of final states for the transition.

A valence or core-hole remains once the photoelectron has left the molecule or atom. If a core-hole is present the system will be in an unstable excited state with a finite lifetime. The system will be stabilized when a electron drops down from the valence band and fills the core-hole, since it is more energetically favourable. In this step a loss of energy will occur due to conservation of energy, and it will be done by either emission of a photon, fluorescent decay, or emission of an electron, Auger decay. Auger decay is the dominant process for elements with low atomic mass, and makes it easier to detect than X-ray fluorescence. In reality the spectrum is affected by a number of factors, making this correspondence quite sophisticated, even though photoemission

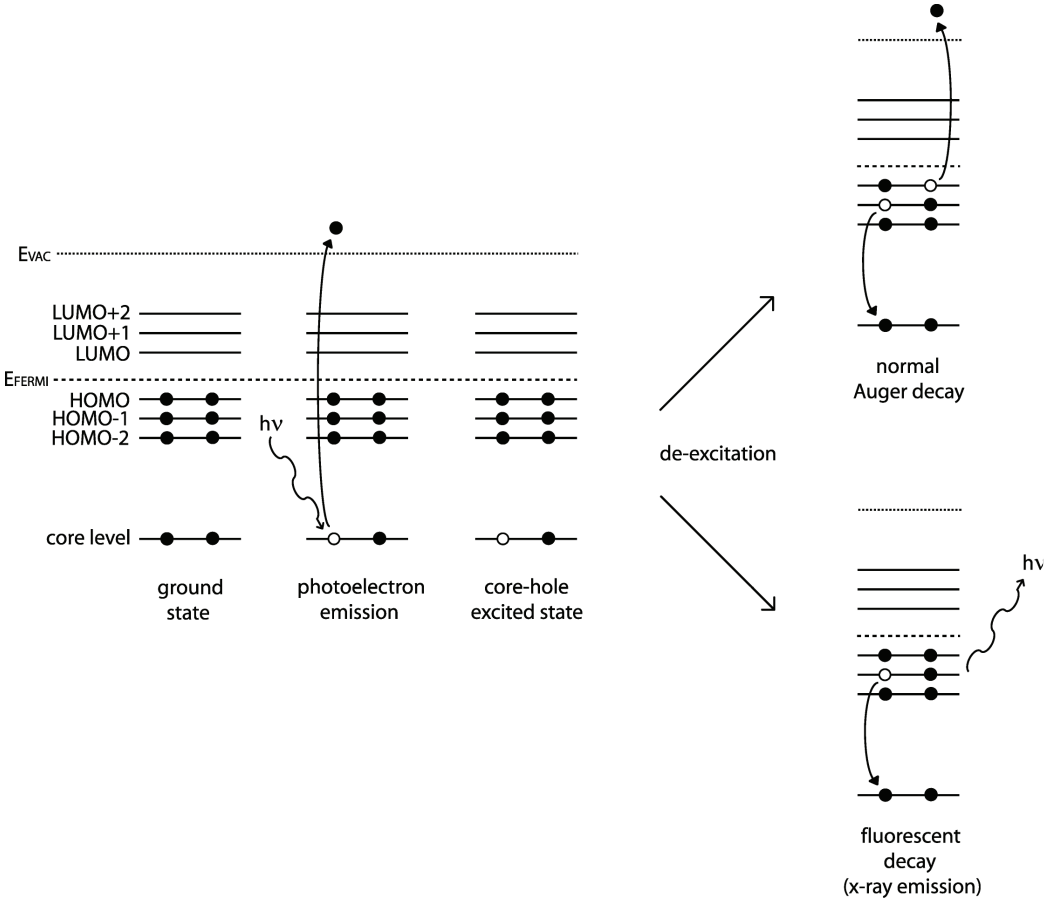

Figure 3.3: Diagram showing the electronic energy level for a photoemission process for a molecule. The molecule absorbs a photon with an energy of $\hbar\omega$ and photoelectron is emitted from the molecule. In the presence of a core-hole the molecule is left in an excited and unstable state. A electron drops from the valence band to fill the core-hole, and either an photon or electron is emitted. Reproduced with permission from reference [140].

spectroscopy, PES, remains as one of the basic spectroscopic tools of matter characterization.[139]

Within PES, there are two main types of techniques: (I) Ultraviolet photoemission spectroscopy (UPS), which is used mainly for studying valence bands close to the Fermi energy. In this technique noble gases are used to generate radiation in the ultraviolet. (II) X-ray photoemission spectroscopy (XPS). In this technique metals such as tungsten, aluminium or magnesium undergo an electron bombardment to produce X-rays specific to the core of the system in question. Using synchrotron radiation blurs the boundary due to the wide range of photon energies it can produce.[141].

In the scheme of soft X-ray photoelectron spectroscopy the energy range of

the excitation radiation employs photon energies of 150-2000 eV. Within this energy range the binding energies of the core levels for many interesting chemical elements, like gold, titanium, manganese, zinc etc. are found. Therefore soft XPS is also referred to as core-level photoelectron spectroscopy.

One of the main theoretical approaches to describe a process of photoemission from solids is the model suggested by Mahan[142] and further developed by Pendry[143] which considers an instant transition of an electron from its initial bound state in the crystal to a final free state in the vacuum as a result of a photoemission process. The transition probability, P_{if}, of an electronic transition, between an initial $|i>$ and a final state $|f>$ is defined by the Fermi Golden Rule, which yields:

$$P_{if} = \frac{2\pi}{\hbar} \mid \langle \psi_f, \mathbf{k}_f \mid H^{int} \mid \psi_i, \mathbf{k}_i \rangle \mid^2 \delta(E_f - E_i - \hbar\omega)\delta(\mathbf{k}_f - \mathbf{k}_i - \mathbf{G}) \quad (3.5)$$

The Hamiltonian H^{int} describes an interaction between an electron and an electromagnetic wave (photon) The terms ψ_i and E_i are the wave function and the energy of the initial many-electron state, while ψ_f and E_f refer to the wave function and the energy of the final state respectively. Taking a close inspection of equation 3.5 it becomes clear that $\mathbf{k}_f$ is the wave vector that describes the photoelectron in the final state inside the crystal. Likewise, $\mathbf{k}_i$ is the wave vector that describes yet bound electron in its initial state inside the crystal. The term $\mathbf{G}$ is the smallest reciprocal lattice vector. The energy conservation law is fulfilled by the two delta functions, so that the energy difference between the final and initial states equals $\hbar\omega$. Notably the momentum of the photon is not included into the conservation law, and equation 3.5 only describes a vertical or optical transition, obtained for sufficiently low photon energies. Both initial and final state many-electron wave functions can be factorized i.e. represented as a multiplication of one-electron wave functions: $\Psi(\mathrm{N}) = \mathrm{C}\phi_k\psi_R^k(\mathrm{N\text{-}1})$. Here k refers to the k^{th} electron and R to the remaining system, ϕ_k is the one-electron wave function $\psi_R^k(\mathrm{N\text{-}1})$ is the wave function for the rest and C is an antisymmetrizing operator. Using this factorization of the

many-electron wave function, where Ψ_i(N) = C$\phi_{i,k}\psi^k_{i,R}$(N-1) and Ψ_f(N) = C$\phi_{f,k}\psi^k_{f,R}$(N-1) will describe the initial and final state respectively, the matrix element of equation 3.5 becomes

$$M_{if} = \langle \phi_{f,k} \mid H^{int} \mid \phi_{i,k} \rangle \langle \psi^k_{f,R}(N-1) \mid \psi^k_{i,R}(N-1) \rangle \tag{3.6}$$

Therefore, the matrix element of the photo-ionization process consists of a one-electron transition matrix element and an overlap integral of the rest electron system.

The interaction Hamiltonian H^{int} in equation 3.5 can approximately be written as:

$$H^{int} = \frac{e}{mc}(\mathbf{A} \cdot \mathbf{p} + \mathbf{p} \cdot \mathbf{A}), \tag{3.7}$$

where $\mathbf{p}$ is the momentum operator of an electron and $\mathbf{A}$ is the vector potential of the electromagnetic field. The variable e is the electronic charge, m is the electron mass and c is the speed of light. If the spin of the electron is neglected, equation 3.7 can be simplified further to:

$$H^{int} = \frac{e}{mc}(\mathbf{A} \cdot \mathbf{p}). \tag{3.8}$$

The magnitude of the vector potential, A_0, is related to the magnitude of the electric field vector, E_0, via the equation:

$$E_0 = A_0 \frac{\omega}{c}, \tag{3.9}$$

where ω is the frequency of the light. Introducing a plane wave, the perturbation can then be derived as:[144]

$$H^{int} = \frac{eA_0}{2mc} \exp(i(\mathbf{k} \cdot \mathbf{r})(\hat{\mathbf{E}} \cdot \mathbf{p})). \tag{3.10}$$

In the dipole approximation the wavelength of the light is considered to be significantly larger than the atomic radius: $r << \frac{\lambda}{2\pi}$, then $\mathbf{k}\cdot\mathbf{r} << 1$ and hence $\exp(i\mathbf{k} \cdot \mathbf{r}) \simeq 1$. This allows the perturbation to be reduced to $H^{int} = \frac{eA_0}{2mc}\hat{\mathbf{E}} \cdot \mathbf{p}$,

and since the term $\delta(E_f - E_i - \hbar\omega)\delta(\mathbf{k}_f - \mathbf{k}_i - \mathbf{G})$ in equation 3.5 describes the density of states, ρ, for the final state[141, 144], equation 3.5 becomes

$$P_{if} = \frac{e^2 E_0^2 \pi}{2\hbar m^2 \omega^2}(< i \mid \hat{\mathbf{E}} \cdot \mathbf{p} \mid f >)^2 \rho. \tag{3.11}$$

To obtain the X-ray absorption cross section $\sigma_{\text{X-ray}}$, the transition probability has to be divided by the number of photons that travel through the unit area per unit time. The cross section is then:[144]

$$\sigma_{\text{X-ray}} = \frac{4\pi^2 e^2}{m^2 c\omega}(< i \mid \hat{\mathbf{E}} \cdot \mathbf{p} \mid f >)^2 \rho. \tag{3.12}$$

The binding energy E_B^v of a photoelectron escaping from a certain one-electron orbital k was defined as a negative value of the energy of the respective one-electron orbital. This is Koopmans' theorem.[139] In other words, this theorem assumes that the one-electron orbitals in the atom are not affected by the photo-ionization process or are "frozen". From this approximation we obtain $\psi_{i,R}^k(\text{N-1}) = \psi_{f,R}^k(\text{N-1})$ in the matrix element of equation 3.6, and the corresponding overlap integral becomes unity. Thus, in the frozen approximation binding energy of an orbital by definition equals its Koopmans' energy, and we write:

$$E_{\text{B}}^{\text{v}} = -\epsilon_{\text{k}} \tag{3.13}$$

However, in reality the orbitals are not frozen but rather react to the core hole created by the photo-ionization process and since the system tends to minimize the total energy, the final state effects need to be taken into account for a more accurate estimation of the binding energy. Usually Koopmans' binding energy ϵ_{k} is corrected by the addition of two terms:

$$E_{\text{B}}^{\text{v}} = -\epsilon_k + \Delta\epsilon_{relax} + \Delta\epsilon_{corr} \tag{3.14}$$

where $\Delta\epsilon_{relax}$ is a term describing the change in the binding energy upon atomic orbitals contraction around the core hole – relaxation – and the charge transfer of polarization screening. The term Δ_{corr} includes collective effects

of electron-electron interactions in the system – correlation in the electron motion. This term is often neglected as the correlation effects are rarely pronounced, but can be important in certain cases. Inclusion of the relaxation correction term into the calculations lowers the core-level binding energy and gives better agreement with experimental data. However, even the relaxation and correlation-corrected Koopmans' approximation only treats a sole final state of an atom, which is not necessarily true.

A slightly different approach to explain photo-excitation of an atom is by the sudden approximation. Here the excitation of the promoted electron is rapid and the inactive electrons do not relax before the excitation is complete. The total final and initial states can be separated into the single promoted electron ϕ and the inactive multiple electron Φ, this means that the dipole matrix element can be simplified to $\langle\phi_f|\mathbf{p}|\phi_i\rangle\langle\psi_f|\psi_f\rangle$, where the momentum operator $\mathbf{p}$ is specific to the active electron. This mean that equation 3.12 takes the form:

$$\sigma_{\text{X-ray}} \propto |\hat{\mathbf{E}} \cdot \langle\phi_f|\mathbf{r}|\phi_i\rangle|^2 \tag{3.15}$$

This shows that the intensity of a photoelectron peak is not just dependent on the density of states and number of molecules. Certain transitions are far less likely to occur and can affect the total absorption cross section. Also, as can be seen from equation 3.15, the direction of polarization for the incoming radiation is very important. If the molecules are not randomly oriented, then the cross section can change when the sample orientation to the incoming radiation is changed. In general the sudden approximation helps to explain the presence of additional features in the photoelectron spectrum, such as satellite lines. The presence of satellite lines in a photoelectron spectrum of an atom can be well exemplified with "shake-up" spectral structure, observed to the lower kinetic energies (higher binding energies) from the main photoelectron line. Shake-up processes involve excitations of valence band electrons, thus a latter are excited or are literally "shook up" to unoccupied valence levels. There are also so-called "shake-off" processes involving ionization of a valence electron

into the continuum, i.e. off the crystal, and resulting in the formation of broad spectral features at higher binding energies. The photoemission spectrum can consist of several lines as shown in Figure 3.4, the main line corresponding to the most relaxed state, or fully screened core hole, at lowest binding energy. The satellite lines are found at higher binding energies and involve different excited final states.

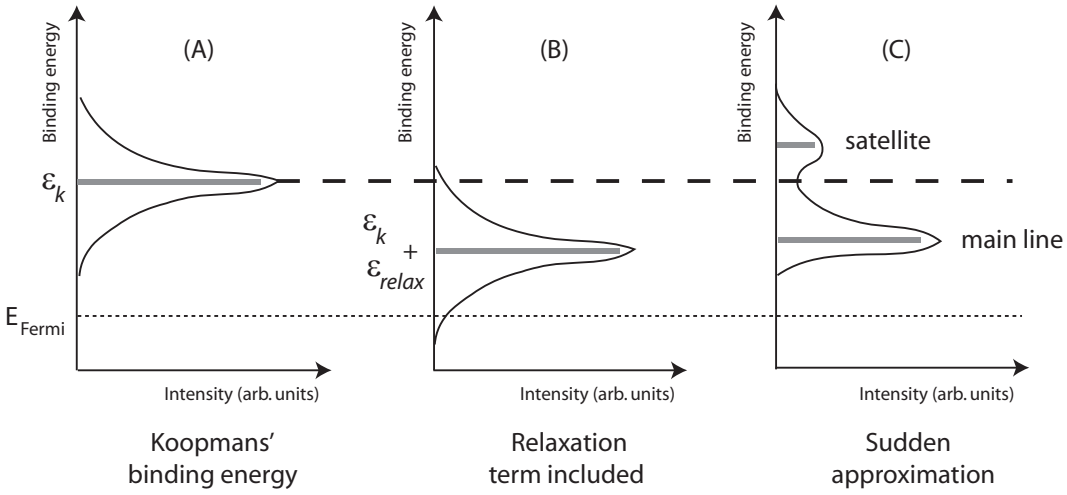

Figure 3.4: Schematic of the photoelectron line position calculated in frames of different approximations discussed: (A) Koopmans' frozen-orbital approximation, (B) with the relaxation correction term included, (C) Sudden approximation. The black solid line shows a schematic of a real photoelectron spectrum upon these approximations.

In the ideal case the photoemission spectra would consist of sharp peaks, broadened only as a result of their limited lifetime, but in the real case scenario several sources of broadening can affect the line shape of the main photoemission peaks. The instrumental limitations and the core hole lifetime will always be contributing factors.

The instrumental limitations are primarily monochromator resolution – the width of the X-ray source – accompanied with the resolution of the analyzer, makes essential contribution to the photoemission line width. The instrumental broadening is typically a Gaussian.[135] The natural line width, given by a Lorentzian distribution[145], also contributes to the broadening due to the finite lifetime of the core-excited system. Since the lifetime of the core-hole is finite, in the atto- to femtosecond region[146], Heisenberg's uncertainty prin-

ciple ($\hbar \leq \Delta E \times \Delta t$, where E is the energy and t is time) tells us there will always be a degree of broadening in the energetic levels. As an example the lifetime width of the core levels in the case of N $1s$, C $1s$ and O $1s$ are close to 0.1 eV.[146]

A split of the core-level peaks will also be present for orbitals other than s orbitals, due to the spin-orbit coupling. This arises from the coupling between the spin of an unpaired core electron with its angular momentum.[147, 148] The spin (s) of unpaired electrons can be either parallel or anti-parallel to the direction of its orbital angular momentum (l), whereas the paired electrons' cancel each out and have no over-all spin. When one unpaired electron is present, two discrete states will present with a total momentum of $J = l \pm \frac{1}{2}$. In Figure 3.5 a photoemission spectrum of a gold sample is shown. Here the photon energy used during data acquisition was 140 eV. The Au $4f$ state splits into to discrete peaks corresponding to the Au $4f\frac{5}{2}$ and Au $4f\frac{7}{2}$. In this case $l = 3$ and the intensity ratio between the spin-orbit peaks is given by the degeneracy of each state, $2J+1$, resulting in a ration of 6:8. The orbital angular momentum is proportional to the separation in energy of the peaks, meaning a strong spin-orbit coupling is the result of the atomic shell being close to the nucleus, and the energy splitting of the photoemission line will be large.

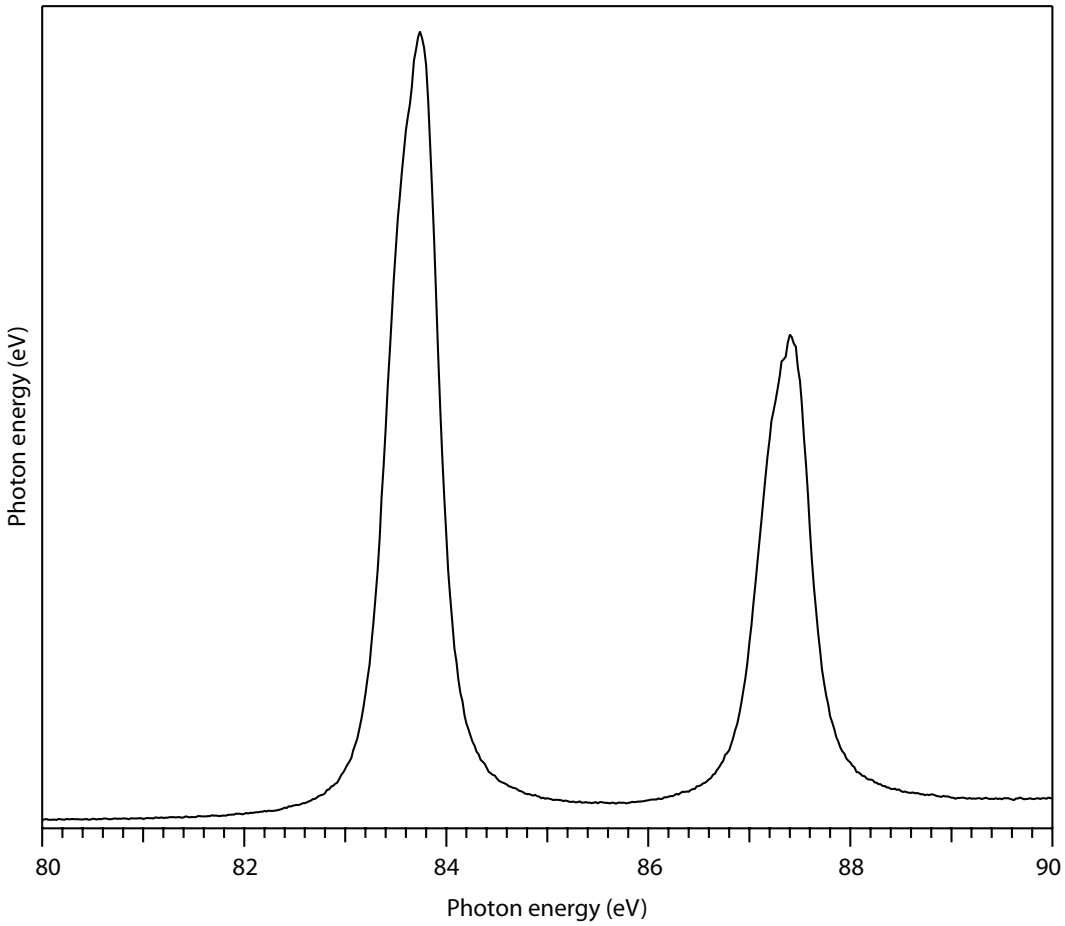

Figure 3.5: Au 4*f* peaks at a photon energy of 190 eV.

There are also other effects one may encounter when acquiring photoemission spectroscopy data. The spectra can be shifted in energy of the emitted electron, and can provide valuable information about the system. These shifts can be caused by the surrounding environment and are called chemical shifts. These shifts provide information about the functional groups in a compound and determine the bonding arrangements between molecules and surfaces. Here XPS is a powerful tool for identifying elements present in wide energy scans and for determining the chemical environment of the specific elements using narrow energy scans. The molecule of ethyl-trifluoroacetate, shown in Figure 3.6, is a widely used example to show the chemical shift since it exhibits a shift of more than 8 eV.

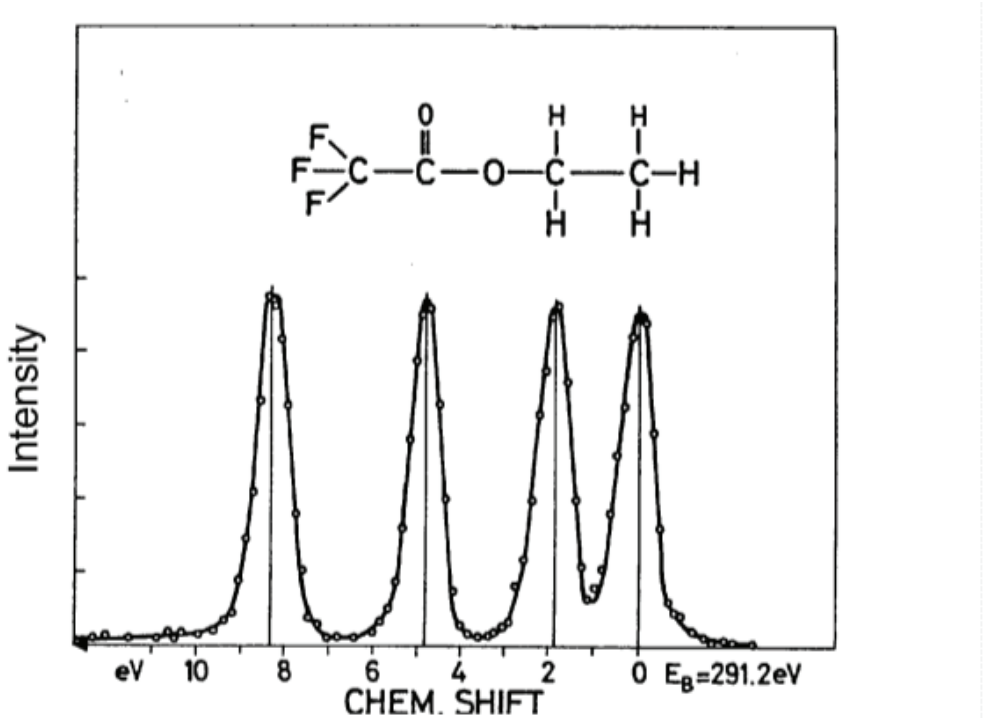

Figure 3.6: C 1s of ethyl trifluoroacetate. Reproduction from [149]

3.4 X-ray Absorption Spectroscopy

The versatile technique of X-ray absorption apectroscopy (XAS) is founded on the absorption of X-rays with different energy. The technique provides information about the unoccupied density of states by measuring the absorption probability of an X-ray photon as a function of the photon energy $\hbar\omega$, meaning that element-specific information about the energy distribution and symmetry of unoccupied electronic states can be extracted, (see equation 3.15). In the XAS scenario, where the energy of the X-ray photon is less than or equal to the binding energy of one of the inner shell, this is called a photo-excitation process. In this case intense, sharp and developed absorption structures will be present in the energy range 5-10 eV below the upper energy limit – the binding energy of the inner shell. This region is also called the pre-edge region. These characteristic structures will continue up to 30-50 eV above the edge. This structure is called X-ray absorption near-edge structure (XANES) or near-edge x-ray absorption fine structure (NEXAFS). In principle, both of

these abbreviations describe the same energy range. However, these are often referred to as NEXAFS for any pre-edge structure, and as XANES for near-edge structures, respectively. Lately, an unwritten rule regulating the terminology between NEXAFS/XANES is frequently obeyed, which can be stated as "NEXAFS refers mostly to pre-edge sharp and pronounced structure of X-ray $1s$ (K-edge) absorption spectra for low-Z elements (C, N, O, etc.) and probes its bonds to intra-molecular, and to a lesser degree, extra-molecular neighbors."[144] The technique of NEXAFS is commonly used when the molecular orientation of adsorbed molecules on a surface is wanted. The origin of the molecular orbitals in organic molecules are the result of the mixing between the atomic orbitals. When the molecules consist of atoms with a low atomic number they are very symmetrical and correlate very well with the spatial arrangement of atoms in the molecule [144, 150] The orbitals usually probed are the π^* and the σ^* orbitals. For organic molecules the π^* orbitals are a result of the overlap between of the two $2p_x$ and $2p_y$, where the σ^* is the outcome of the overlap between two $2p_z$.[144] Within these two molecular orbitals the electrons are likely to be found in certain directions. The σ^* orbital will mainly be exhibit along the intermolecular axis and away form the intermolecular axis, whereas the π^* orbital occurs above or below the bond[150], this is displayed in Figure 3.7.

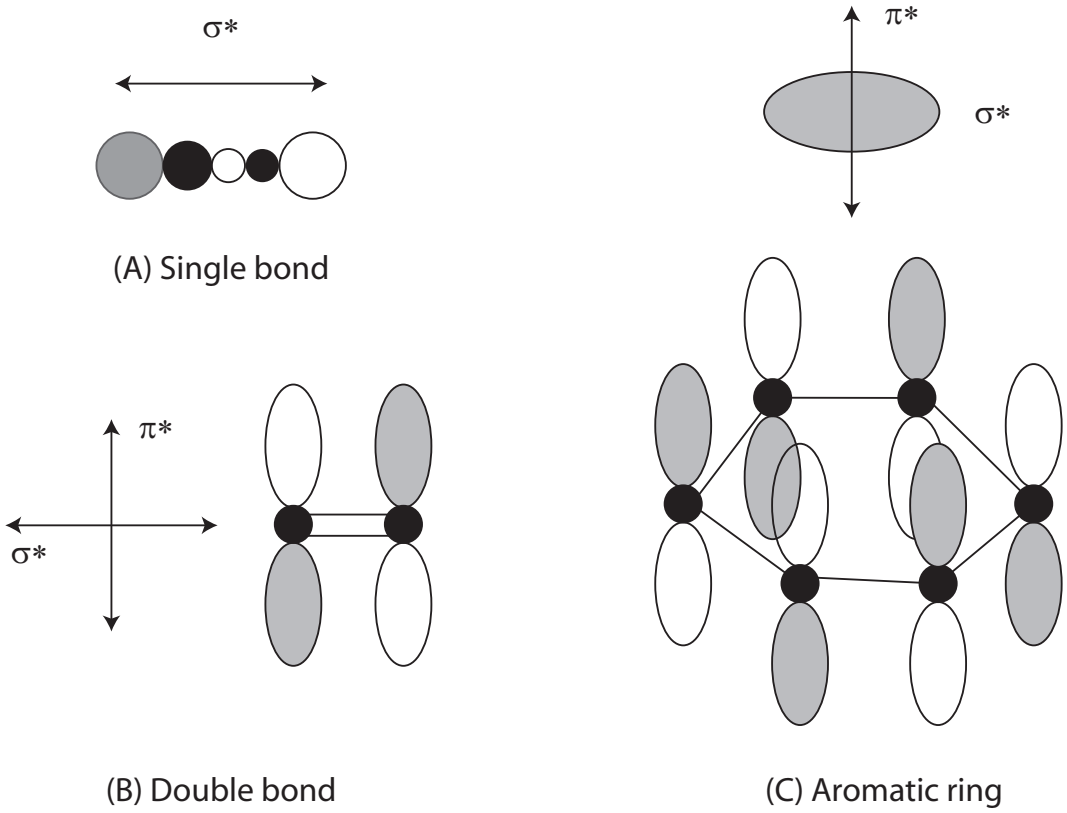

Figure 3.7: Schematic illustration of spatial orientation of π^* and σ^* orbitals in three important bonding arrangements. Molecules can be classified depending on whether the π^* or σ^* orbitals point in a specific direction or whether they span a plane.

These two unoccupied molecular orbitals and the angle, Θ, between them can be observed using NEXAFS. Figure 3.8 displays the coordinate system showing the angles of importance for determining the angular dependence of the resonances in a NEXAFS experiment. The orientation vector of the orbital, $\hat{\mathbf{O}}$, is aligned with the maximum amplitude of the final state orbital for the excited atom. Changing the x-ray incidence angle produces changes in absolute intensity of the resonances.

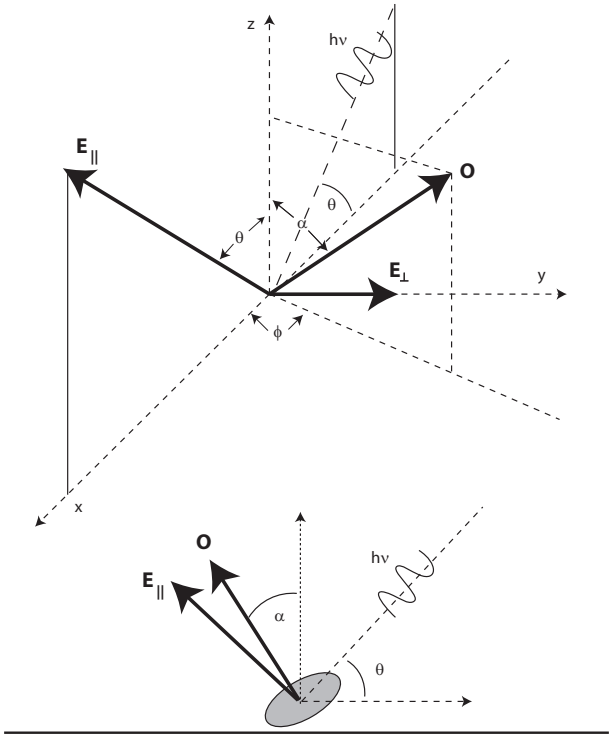

Figure 3.8: Diagram defining the angles used to determine the molecular adsorption geometry, with θ being the polar angle of the X-ray with surface. The term α denotes the angle between the molecule and surface normal and is the one in question. The azimuthal angle ϕ will be averaged out on highly symmetrical surfaces. The bottom figure shows a two-dimensional view, along the y-direction. The shaded area is representing an aromatic ring structure.

The changes in resonance intensity will be proportional to the changes in the X-ray absorption cross-section, and equation 3.15[150] can be written as:

$$\sigma \propto | \hat{\mathbf{E}} \cdot \hat{\mathbf{O}} |^2 \tag{3.16}$$

The size of the absorption cross section for each set of orbitals is determined by the incoming light. The relationship between the absorption cross section, the spatial arrangement of the orbital and the polarization of the light is not straightforward since synchrotron radiation is not completely linearly polarized.[144] By representing the elliptical polarization as a super position of two electric field vectors, $\mathbf{E}_{||}$ and $\mathbf{E}_{\perp}$, where $\mathbf{E}_{\perp}$ is 90° out of phase, the cross section becomes

$$\sigma \propto \mid \hat{\mathbf{E}}_{||} \cdot \hat{\mathbf{O}} \mid^2 + \mid \hat{\mathbf{E}}_{\perp} \cdot \hat{\mathbf{O}} \mid^2 \tag{3.17}$$

If we define the amount of linear polarization as:

$$P = \frac{|\mathbf{E}_{||}|^2}{|\mathbf{E}_{||}|^2 + |\mathbf{E}_{\perp}|^2}, \tag{3.18}$$

and since $\mathbf{E}_{||}$ is the dominant component, equation 3.17 takes the form:

$$\sigma \propto P \mid \hat{\mathbf{E}}_{||} \cdot \hat{\mathbf{O}} \mid^2 + (1+P) \mid \hat{\mathbf{E}}_{\perp} \cdot \hat{\mathbf{O}} \mid^2 \tag{3.19}$$

Using Figure 3.8 as a frame of reference, we can now write the NEXAFS signal intensity, I, as a fuction of the the angle of orientation of the molecule to the normal of the surface α, polar angle of the X-ray to the surface, θ, and the azimuthal angle ϕ

$$I \propto P|\sin(\alpha)\cos(\phi)\sin(|\theta)|^2 + (1-P)|\sin(\alpha)\sin(\theta)|^2 \tag{3.20}$$

If the intensity is considered as a function of the polar angle, meaning that the azimuthal variations have been averaged out, and introducing a threefold or higher symmetrical substrate equation 3.20 can be drastically simplified to

$$I \propto \cos^2(\theta)\cos^2(\alpha) + \frac{1}{2}\sin^2(\theta)\sin^2(\alpha) \tag{3.21}$$

Equation 3.21 only takes this form if the light source produces highly linearly polarized light, which is the case in the present work[151]. The motivation for deriving equation 3.21 is to obtain the angle α between the surface and the molecule, and this is straightforward, since θ is chosen by the user of the equipment and the intensity of final state orbital is given by the ratio between the σ and π intensities.

There is no question that high precision in the determination of the photon energy is required when monitoring XAS. The precise calibration of this is somewhat straightforward when using grating-based monochromators. These kind of monochromators will transmit a small fraction of higher diffraction order into the experimental chamber. The calibration method is called "2^{nd} order

light" calibration, and uses the fact that "second-order" photoelectrons possess the energy of $E_{kin,2} = 2\hbar\omega_1 - E_{bin}$. The "first-order" photoelectrons have the energy of $E_{kin,1} = \hbar\omega_1 - E_{bin}$, and the difference in kinetic energies becomes: $\hbar\omega_1 = E_{kin,2} - E_{kin,1}$. Proper normalization of the incident photon flux is also necessary, since the intensities of the spectral features in the XAS depends on this flux. Promotion of artifacts in the absorption spectrum can occur due to the structured energy-dependent flux of incident radiation. These artifacts will relate to features of the incident radiation rather than the properties of the sample. One issue of great importance to normalization are spectral contaminations and imperfections. An example is the so-called "carbon-dip" that arises from decomposition of carbon from the residual gas molecules when it is exposed to the high intensity synchrotron light. The optical elements controlling the guiding and focusing of the light will experience adsorption of this carbon leading of a characteristic dip in the carbon absorption spectra, hence the name.

At higher photon energies, beyond the absorption edge, the X-ray absorption intensity decreases monotonously as the cross-section for the corresponding process goes down. However, within the X-ray absorption spectrum, and up to several hundred electro-volts above the absorption edge, broad low-intensity oscillation can be found. These oscillations are the result of interference between the initial and scattered photo-electron waves arising from the photo-electron scattering by the atoms of the nearest coordination spheres.[152] The technique using this extended energy range where called Extended X-ray Absorption Fine Structure, EXAFS. This is especially interesting for collecting information about aqueous solutions, since EXAFS has proven to be sensitive even to hydrogen atoms[153, 154]. EXAFS spectroscopy is not discussed in detail here since it was not employed as an analysis technique in this thesis.

3.5 Resonant photoemission spectroscopy

Another technique found within the realms of photoemission spectroscopy is resonant photoemission spectroscopy, RPES. RPES shares a resemblance with NEXAFS in the sense that an electron is excited from the core-hole to unoccupied bound states of the system, but in RPES the kinetic energy of the photoelectrons and thereby the binding energy is determined during a subsequent Auger decay at the different photon energies. The decay mechanism of an adsorbate-surface interface can hereby be studied.

The technique of RPES plays an important role in the determination of charge delocalisation and charge transfer processes in organic photovoltaics and DSSCs. In similarity to optical excitation from valence states, the initially excited electron within the scheme of RPES will be promoted to a core-excited unoccupied molecular state. Charge transfer that occurs from either valence-hole excited states or core-hole excited states can be considered to be very similar.[155] In Figure 3.9 the different excitation and de-excitation situation are sketched out. The decay of the core-hole can occur via three distinct channels.

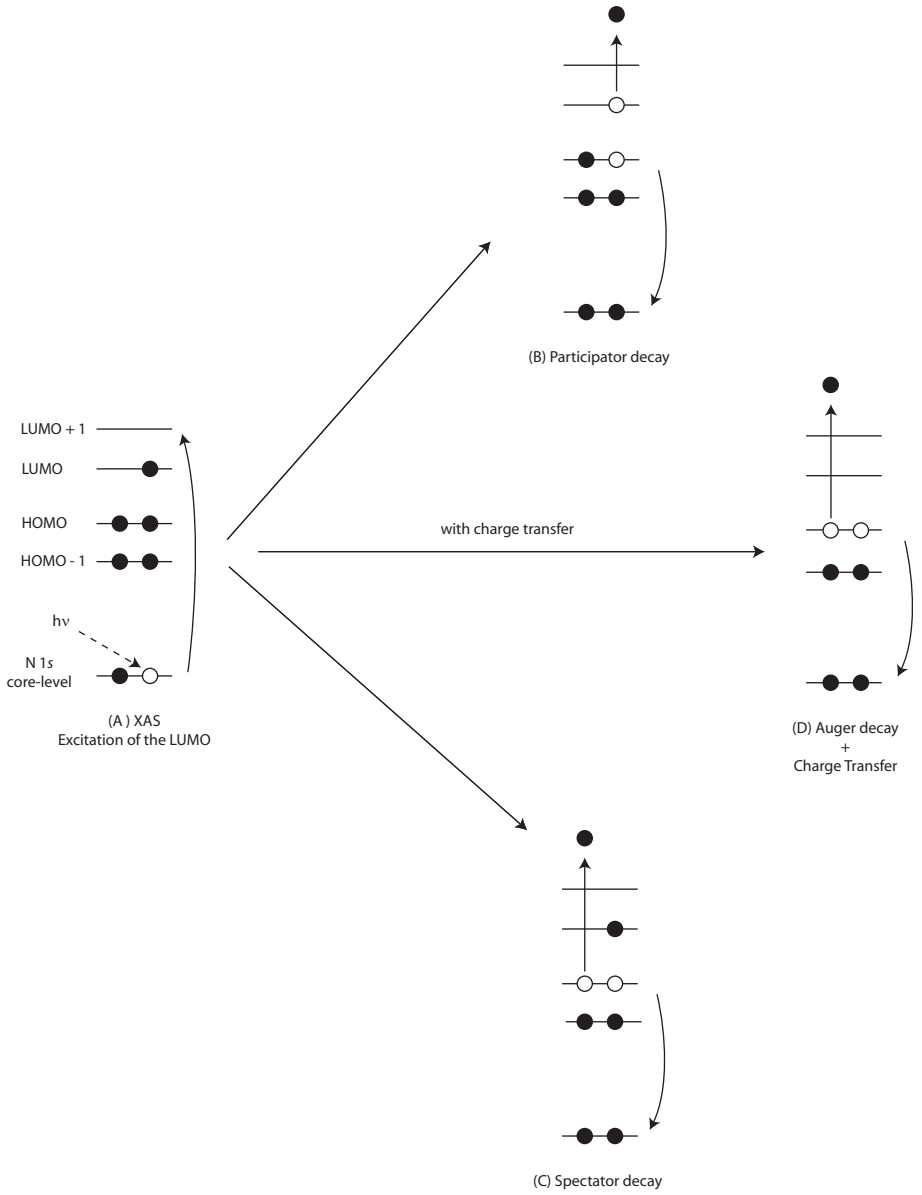

Figure 3.9: Diagram showing possible decay channels from a core-excitation seen in (A). Participator decay is shown in (B), where the originally excited electron is emitted as an Auger electron. Spectator decay is shown in (C), where the originally excited electron spectates the Auger decay of another electron from the occupied levels. In the presence of charge transfer to the surface, normal auger decay can occur, as seen in part (D).

When the auto-ionization processes occur, an Auger electron is emitted, and the leaves the system in a final state with an overall charge of +1. This can happen through two distinct channel, termed participator and spectator decay, respectively. They are labelled (B) and (C) in Figure 3.9. When the decay uses the participator channel, the originally excited electron is emitted

as an Auger electron. This process will show itself in the RPES spectra in the low end of the binding energy scale having high intensity. Depending on the electronic structure of the occupied valence band several points of high intensity can be observed, albeit a large amount of spectator decay can make them undistinguishable and therefore they can not be resolved from each other.

In participator decay, as seen in Figure 3.10, the originally excited electron is emitted as an Auger electron. This can be observed in the RPES as a point of high intensity with very low binding energy, as seen in the diagram of a typical RPES Spectra in Figure 3.10. Participator decay leaves the system in the same final state as valence band photoemission or PES of the highest molecular orbital, so according to the previous equations it is indistinguishable from PES and appears as a resonant enhancement of the state in photoemission, hence the name. Several points of high intensity can be observed depending on the electronic structure of the occupied valance band, although they may be undistinguishable fore a large amount of spectator decay.

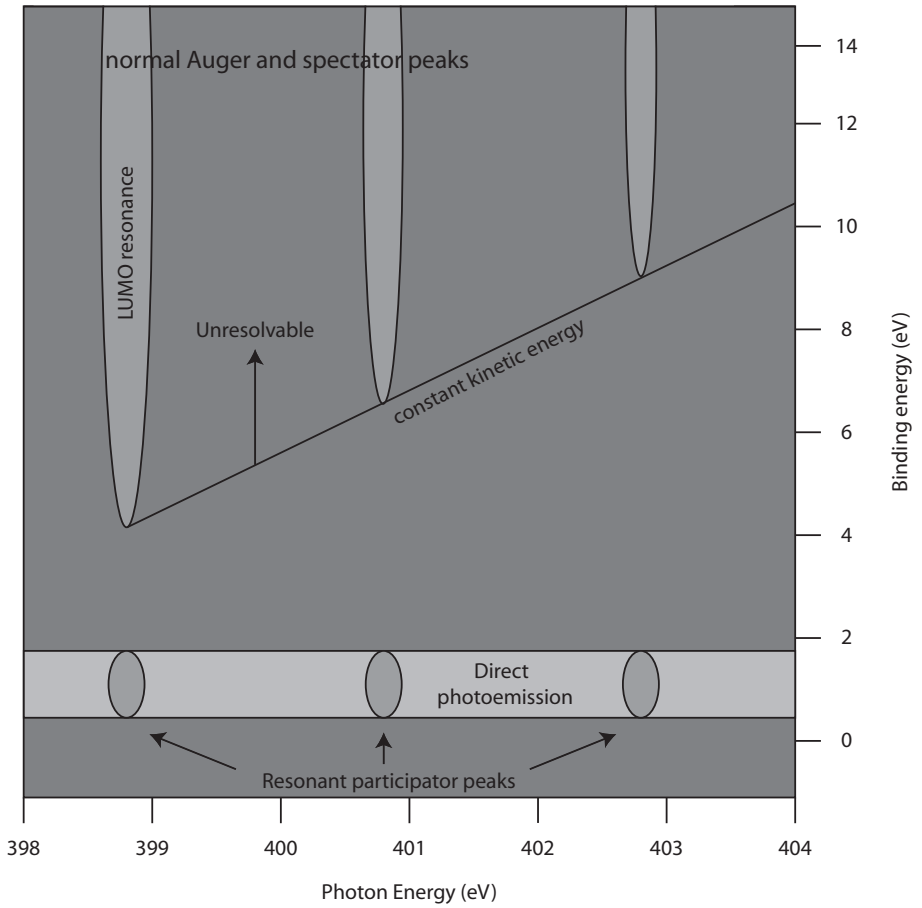

Figure 3.10: Schematic diagram of a typical two-dimensional RPES spectrum. The lighter areas represent areas of higher intensity. During the participator decay, the original excited electron is emitted from a higher level, resulting in participator peaks at lower binding energy in than of the normal Auger and spectator peaks. The Auger and spectator peaks can not be resolved from each other.

Figure 3.9 (C) shows the spectator decay. As the name of this channel indicates, the initial excited electron will take the role as a spectator, while an electron from the occupied molecular orbital is being emitted. This electron is only dependent on the valence-band electrons, and is found in a RPES spectrum at a higher binding energy than that of the participator decay at each resonance. The vast amount of electrons in the occupied valence band

compared to the number found in the core-excited state, and that the spectator decay depends on them, results in a much larger cross section for the spectator channel compared to the participator, even though some matrix element lowers the cross section[155, 156]

If charge transfer is present, which is illustrated in Figure 3.9(D), an electron will be transferred into other states coupled to the system, and the system relaxes via a normal Auger decay leaving it in an overall final state of +2. This type of decay cannot be distinguished from the spectator decay, because the spectator shift is in the order of 1 eV and the Auger peak/background itself is very broad. The qualitative argument for proceeding involves considering the two extreme cases of no charge transfer and maximum charge transfer. The former will be the case for a thick multilayer of molecules on the surface, where the molecules can be regarded as isolated form the surface. The latter case is when a chemisorbed monolayer of molecules is present on the surface. By monitoring the amount of participator decay in these two extremes it is possible to determine the amount of charge transfer. Since the charge transfer has to occur in the core-excited state – before the core-hole decay – the lifetime of the core-hole becomes an upper time limit for which the charge transfer can take place. This is also called the "core-hole clock" implementation, since the lifetime of the core-hole serves as the time measurement device.[156]

In the derivation towards obtaining an expression for the charge transfer some assumptions need to be laid out. The lifetime of the core-hole will always stay the same whether or not charge transfer is occurring, therefore these two processes will be regraded as independent. Since both of them are decay processes, their probabilities of taking place are assumed to display an exponential function of time, t, by the equation:[156]

$$N(t) = N_0 \exp\left(-\frac{t}{\tau}\right), \tag{3.22}$$

where N(t) describes the number of molecules remaining unchanged after time t. Before any other event can occur there are N_0 molecules in the excited state. The characteristic lifetime for the core-hole decay or the charge transfer

is denoted by τ. At the time X an event, such as core-hole decay, will happen. Then the probability density, p, of an event occurring at time t is $p(X = t)$dt $= |dN(t)|/N(0)$. The probability of corehole decay occurring before time T and the probability of no charge transfer event occurring before time T are then given by equations 3.23 and 3.24, respectively.

$$P_{chd}(t) = \int_0^T \frac{1}{\tau_{chd}} \exp\left(-\frac{t}{\tau_{chd}}\right) dt, \tag{3.23}$$

$$P_{noCT}(t) = 1 - \int_0^T \frac{1}{\tau_{CT}} \exp\left(-\frac{t}{\tau_{CT}}\right) dt \tag{3.24}$$

where τ_{chd} and τ_{CT} are the average time for a core-hole decay average time for charge transfer, respectively. One of the preliminary assumptions was that the two probabilities are independent, meaning the combined probability takes the form:

$$P_{noCTchd}(T) = \frac{\tau_{CT}}{\tau_{chd} + \tau_{CT}} \left(1 - \exp\left(\frac{T}{\tau_{CT}} - \frac{T}{\tau_{chd}}\right)\right). \tag{3.25}$$

When spectra are recorded the core-excited state has decayed, the limit $T \to \infty$ becomes valid, and the equations take the form:

$$P_{noCTchd}(\infty) = \frac{\tau_{CT}}{\tau_{chd} + \tau_{CT}}. \tag{3.26}$$

The ratio between the auto-ionization processes and the total combined intensity from resonant and non-resonant decay (including the normal Auger decay occurring when charge transfer to the surface is present) reflects the probability of the core-hole decay in the presence of no charge transfer. The probability of de-excitation when no charge transfer is present becomes:

$$P_{noCTchd}(\infty) = \frac{I_{\text{auto}}}{I_{\text{auto}} + I_{\text{Auger}}}, \tag{3.27}$$

where the variable I_{auto} is that of the auto-ionisation, the combination of spectator and participator decay, and the variable I_{Auger} arise from the normal Auger decay, that results from charge transfer of the excited electron. We note that the lifetime excited state can also be written in terms of an energy

bandwidth, Γ due to the uncertainty principle.[156] When the molecule couples to the substrate, more de-excitation channels will be available – decreasing the lifetime for the excited state – resulting in a broadening of the measured unoccupied states.

The final state of the normal Auger decay and the spectator decay are very similar, as displayed in Figure 3.9 The outcome of this is two similar components in the RPES spectra. In theory it should be possible to resolve them, due to the small off-set. This off-set arises from the excited electron that screens the core-hole and a shift to higher kinetic energy in the spectator signal is expected. In practise this spectator shift is too small to provide any meaningful accuracy.[156]

A more fruitful route to follow is monitoring the participator channel. The participator peaks consist of emitted electrons from the unoccupied bound states, and therefore they are separated in binding energy from the normal Auger peaks and spectator peaks. When the molecule is in the multilayer it is isolated from the substrate and no charge transfer can occur. Only when the molecule is coupled to the substrate in the monolayer is charge transfer present. This means we can associate the reduction of the participator intensity, $\left(I^{\text{participator}}_{\text{Multilayer}} - I^{\text{participator}}_{\text{Monolayer}}\right)$, to the charge transfer. The probability of charge transfer can, then, be considered as the fraction of the participator peak that has been reduced.

$$P_{CTchd}(\infty) = \frac{\left(I^{\text{participator}}_{\text{Multilayer}} - I^{\text{participator}}_{\text{Monolayer}}\right)}{I^{\text{participator}}_{\text{Multilayer}}}. \tag{3.28}$$

Core-hole decay always occurs eventually, whereas charge transfer can either happen or not happen. So, in the limit that $T \to \infty$, the sum of the probabilities becomes $P_{CTchd}(\infty) + P_{noCTchd}(\infty) = 1$. That means equation 3.26 can be written as:

$$P_{CTchd}(\infty) = \frac{\tau_{chd}}{\tau_{chd} + \tau_{CT}}. \tag{3.29}$$

and using equation 3.28 we obtain

$$\tau_{CT} = \tau_{chd} \frac{I^{\text{participator}}_{\text{Monolayer}}}{\left(I^{\text{participator}}_{\text{Multilayer}} - I^{\text{participator}}_{\text{Monolayer}}\right)} \tag{3.30}$$

If the lowest unoccupied molecular orbital (LUMO) is located below the conduction-band edge there will be no charge transfer from this state to the substrate since it is a forbidden transition. If this is the case, the participator peaks from the integrated RPES spectra can be normalized to the LUMO intensity. By normalizing the intensities to the total cross-section obtained by the NEXAFS measurements, the charge transfer can be written as a function of the intensities of the participator peaks for the multilayer and monolayer. The expression for the charge transfer time becomes:

$$\tau_{CT} = \tau_{chd} \frac{\frac{I^{\text{RPES}}_{\text{Monolayer}}}{I^{\text{NEXAFS}}_{\text{Monolayer}}}}{\frac{I^{\text{RPES}}_{\text{Multilayer}}}{I^{\text{NEXAFS}}_{\text{Multilayer}}} - \frac{I^{\text{RPES}}_{\text{Monolayer}}}{I^{\text{NEXAFS}}_{\text{Monolayer}}}}, \tag{3.31}$$

where τ_{chd} is on the order of femto-seconds for the elements with a low atomic number – 6 femto-seconds for the N $1s$ core-hole decay.[146]

To sum up, RPES provides information about whether a photo-excited electron has been delocalized into the substrate or if it is still localized on the adsorbate itself.[21, 156–158] The RPES spectra are produced by recording a valence band spectra for a range of photon energies above the lowest unoccupied molecular orbital. The outcome are two-dimensional spectra where the de-excitation channels are clearly visible. This allows us to quantify the charge transfer time and the timescale of the delocalisation,[18, 158–160] and since core electrons are involved in the process, atom specificity is ensured.

3.6 Energy level alignment

A crucial part of studying charge transfer between systems, is the alignment of the different energy levels. This provides information about which transitions are possible. Only transitions where the unoccupied levels of the two neighbouring systems overlap are allowed, thus electrons cannot tunnel into already filled energy levels or the band gap in the case of a semiconductor. In

Figure 3.11 an energy level alignment is shown. The technique of NEAXFS spectroscopy provides information about the unoccupied levels of the surface when molecules are adsorbed on it. Photoemission spectroscopy studies make it possible to locate the occupied levels of a surface with a layer of adsorbed molecules, as well as the clean surface. The energy alignment for a metallic substrate is somewhat easier than for the semiconducting counterpart. For the metallic substrate its conduction band will end with the start of its valence band, i.e. the calibration will set the Fermi level at zero binding energy. In the case of a semiconducting substrate a band gap will be present. The band gap can be found through optical studies and placed at the top of the measured valence band, which will in turn define where the substrate's conduction band starts.

The calibration of the photon energies for the PES spectra is done by measuring the first and second order light, and by moving the monochromator during the NEXAFS scan the calibration for this data set is obtained. The shift in kinetic energy gives the true photon energy. When these calibrations are done the key issue is to place the two spectra on a common axis. As mentioned, the NEXAFS spectra provide information about the unoccupied levels, but initially they are measured relative to the core-level. Placing the NEXAFS spectra on a binding energy scale relative to the Fermi level, together with the photoemission spectra will then provide the information about the allowed transitions between adsorbates and substrate.[20]

How to place the NEXAFS spectrum on a binding energy scale more or less falls directly out of the schematic outline for the procedure shown in Figure 3.11

The term Δ is defined as the binding energy of any point on the NEXAFS spectrum relative to the biding energy of the core hole, hence $E_{\text{NEXAFS}}^{\text{Bining energy}} = -\Delta$. The binding energy of the core-hole is calibrated to the Fermi level at 0 eV, and we obtain:

$$E_{\text{NEXAFS}}^{\text{Binding energy}} = -\Delta + E_{\text{Core-hole}}^{\text{Binding energy}}. \tag{3.32}$$

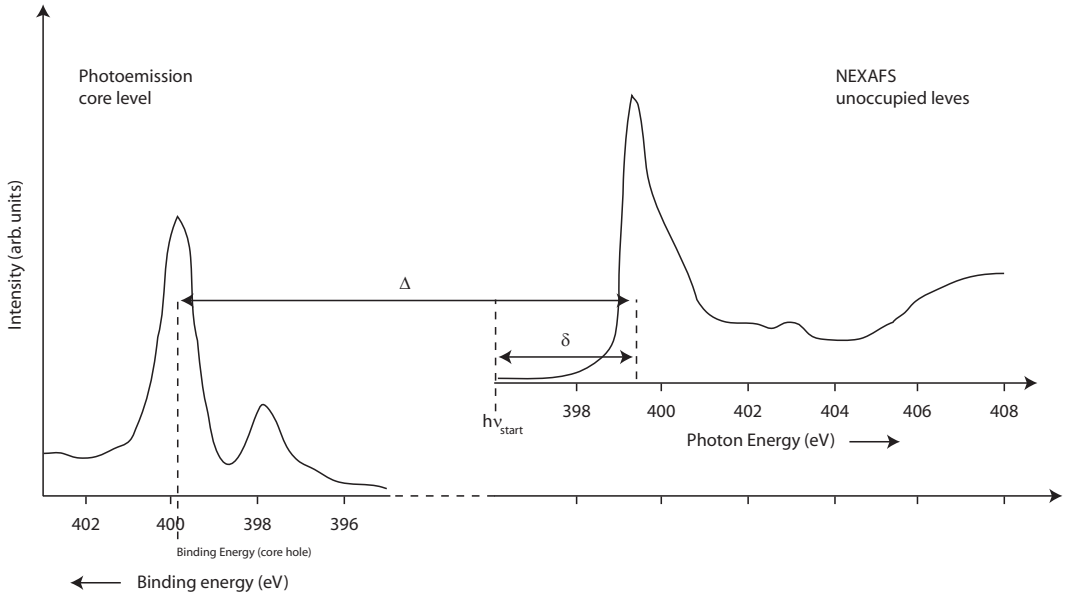

Figure 3.11: Schematic figure to illustrate how a NEXAFS spectrum is converted into a binding energy scale.

We note that $\Delta = \mathrm{h}\nu_{\mathrm{start}} + \delta$ by definition and therefore equation 3.32 takes the form:

$$E_{\mathrm{NEXAFS}}^{\mathrm{Binding\ energy}} = E_{\mathrm{Core\text{-}hole}}^{\mathrm{Binding\ energy}} - \mathrm{h}\nu_{\mathrm{start}} - \delta \tag{3.33}$$

In the case of the evaluation of charge transfer between an adsorbate and the surface, it is useful to have the lowest unoccupied level to overlap with the surface conduction band, since that gives rise to a forbidden transition. This means that this state can be used as a reference point for the higher lying states. These figures represent an energy alignment for the system in its core-excited state, in contrast to the their ground system. Hence, the unoccupied levels are shifted to higher binding energy in the order of eV, due to the Coulomb extraction between the excited electron and the core-hole.

3.7 Surface sensitivity

One of the key benefits of PES is the high surface sensitivity. The penetration of the incident X-rays are several microns[147] depth, but due to the high amount of inelastic scattering only the photo-electrons near the surface will

have the sufficient kinetic energy to leave the surface of the sample. The photoelectrons produced within the bulk will undergo so many inelastic scattering events that they will not escape the sample. Photoelectrons produced a few atomic layers under the surface, having reduced kinetic energy will be recorded as a broad background signal to any measurements taken.

The inelastic scattering processes may include energy transfer to other electrons, or the excitement of phonons and/or plasmons, within the surface. All of these interactions will reduce the kinetic energy of the photo-electrons. A measure of how far the electron may travel through a particular medium is given by the inelastic mean free path, $\lambda(E)$. Equation 3.34 shows the relationship between the initial and final intensities for a flux of electrons travelling a distance d through a metarial[136]

$$I(d) = I_0 \exp\left(-\frac{d}{\lambda(E)}\right) \tag{3.34}$$

where $I(d)$ is the intensity of an electron beam after travelling a distance d through a material with an initial intensity I_0. The inelastic mean free path of an electron is defined as the distance an electron beam travels before its intensity is reduced by $\frac{1}{e}(\approx 0.37)$ of its initial value.[136]

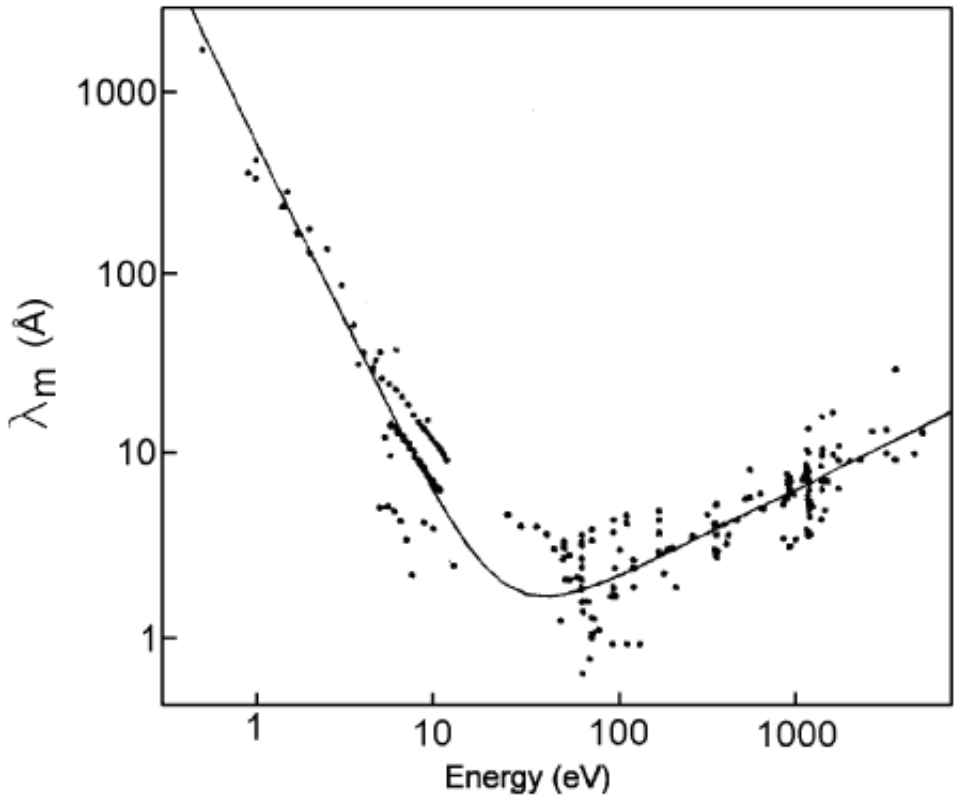

Figure 3.12: Graph of the mean free path of electrons in solids, plotted against electron energy. The data points are for a wide variety of different materials; the solid line is an empirical fit to those data points and is called the universal mean free path curve. This figure is taken from [161].

The inelastic mean free path is highly dependent on the kinetic energy of the electrons. It can be found from empirically derived "universal curve", showed in Figure 3.12 that the shortest mean free path at about 10 Å is given for electrons with kinetic energies between 40-100 eV. A high surface sensitivity is the outcome of a short mean free path, therefore producing photo-electron with a kinetic energy of 50 eV is ideal. Therefore the incident photon energy must be about 50 eV that of the probed binding energy level.

3.8 Experimental setup for Photoelectron Spectroscopy

A crucial part in a photoelectron spectroscopy experiment is the equipment that can measure or detect the kinetic energies of the photoelectron. The typical equipment of choice is an electron analyzer, and the most widespread type is the hemispherical electron analyzer. The schematic of a hemispherical analyzer is shown in Figure 3.13. The two conducting hemispheres, with applied different electrical potential will either guide the electron on it path towards the detector.

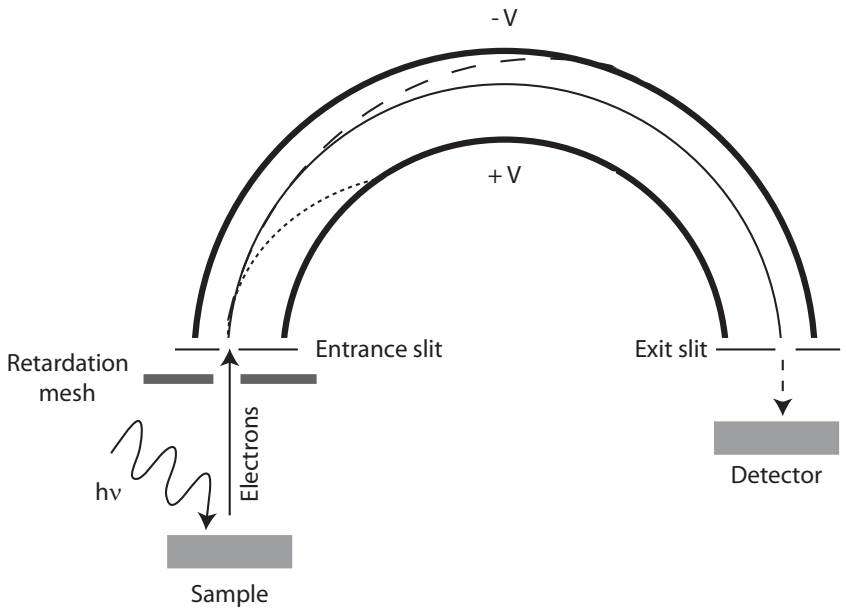

Figure 3.13: A schematic diagram of a hemispherical electron analyser. The solid line indicates the correct path towards the detector. The two other scenarios will either result in the electrons hitting the outer or inner hemisphere, depending on if there are too fast or too slow in their paths, respectively.

The outer hemisphere having a negative potential, thereby repelling the electron, and the inner hemisphere being at a positive potential, attracting

the electrons. The centripetal electrostatic, F_{cp} and the centrifugal F_{cf} forces the electrons experiences on their path, can be written as:

$$F_{cp} = \frac{e\Delta V}{\left(\frac{1}{r_{in}} - \frac{1}{r_{out}}\right) r^2}, \tag{3.35}$$

$$F_{cf} = \frac{mv^2}{r} = \frac{E_{kin}}{r^2} \tag{3.36}$$

respectively. Here r denotes the radius of the path of the electron through the analyzer. The potential difference between the hemispheres is ΔV. The two terms r_{in} and r_{out} are the radii of the inner and outer hemispheres, respectively. It is possible to determine the kinetic energy necessary for the passage through the analyzer by equating equation 3.35 and equating3.36, and we obtain:

$$E_{kin} = \frac{e\Delta V}{\left(\frac{r_{out}}{r_{in}} - \frac{r_{in}}{r_{out}}\right)} = E_{pass} \tag{3.37}$$

where the kinetic energy, E_{kin} now equals the pass energy, E_{pass}.

In Figure 3.13 the path of the electrons is also sketched out. After the electrons have been emitted from the surface of the sample, these photoelectrons enter the first lens group, which focuses them on the decelerator. The decelerator applies the desired pass energy – the mean kinetic energy of electrons traveling through the analyzer. At the second lens stage the photo-electrons encounter an aperture, which focuses them onto the entrance slit and into the the analyzer. If the electron energy is too low, marked with the dotted line, it will hit the inner hemisphere and if it is too high, dashed line, it will hit the outer hemisphere. Only the electron with the right energy, marked with the curved solid line, will have the right trajectory to make it all the way to through the analyzer and finally reach the detector.

Some detectors are position-sensitive, where they use a micro-channel plate. This enables the possibility to retrieve information about the photo-electron angular distribution, $\mathbf{k}_{||}$. This can be achieved by measuring the distribution of the number of electrons, $N(E)$, and scanning the kinetic energy by sweeping

the retardation voltage in the decelerator, while the hemispheres are kept at the fixed potential difference.

The energy resolution of the hemispherical electron analyzer can be calculated a $\frac{\partial E_{kin}}{\partial r}$ where $E_{kin}(r)$ is defined by equation 3.37:

$$\frac{\partial E_{kin}}{\partial r} = \frac{e\Delta V}{2\left(\frac{1}{r_{in}} - \frac{1}{r_{out}}\right) r^2} = \frac{E_{pass}}{\left(\frac{r_{in}-rout}{2}\right)} = \frac{E_{pass}}{r_{mean}}, \tag{3.38}$$

where E_{pass} and $\frac{r_{in}-r_{out}}{2}$ is the pass energy of the electrons. This means that the effective energy resolution of the hemispherical electron analyzer is given by:

$$\Delta E = \frac{\partial E_{kin}}{\partial r} \cdot \Delta r = \frac{E_{kin} s}{r_{mean}} \tag{3.39}$$

where s is effective slit width.[162] To increase the energy resolution the pass energy E_{pass} needs to be decreased or the radii of the hemispheres increased, where the latter is practically impossible since they are defined by the manufacture. The outcome of the this is at low E_{pass} the resolution is high, but there is a low count rate or poor throughput, since it is difficult to focus the electrons on the entrance slit at low energies. The reverse is present with high E_{pass}. This means, that during data acquisition a tradeoff between resolution and throughput of the electron analyzer needs to be determined in real time.

A purely experimental aspect of binding energy evaluation has to be mentioned in this section, namely the reference levels for the kinetic energy of the outgoing photoelectron and correct account and determination of the sample's work function. The excitation of electrons in vacuum from a metallic sample as a result of a photoelectric effect is sketched in Figure 3.14(A), showing also the energetics of the resultant photoelectron spectrum. The latter is a superposition of the primary electrons with kinetic energy E_{kin} defined by the equation 3.3, and the secondary electron continuum. The fastest electrons of this spectrum will be primary electrons emitted directly from the Fermi level ($\mathrm{E_{bin}} = 0$) having $\mathrm{E_{kin}} = \hbar\omega - \Phi_{\mathrm{s}}$, where Φ_{s} is the workfunction of the surface. The slowest electrons will be secondary electrons that just barely escaped from

the sample after having lost energy in inelastic scattering processes before arriving at the sample surface. These electrons have a kinetic energy of $E_{bin} = 0$. In order to determine the kinetic energy of the electrons they have to pass through the electron energy analyzer, as in Figure 3.13 to end up on the detector during the photoelectron experiment. A photocurrent flows from the sample to the detector of the electron analyzer. The analyzer/detector has its own specific work function Φ_a, which generally does not coincide with the sample work function Φ_s. Therefore, a contact potential of $V_c = \frac{\Phi_s - \Phi_a}{e}$ exists between the sample and the analyzer once these are connected electrically, and their Fermi levels are aligned as shown in 3.14(B). Usually the analyzer work function is smaller than the sample work function, i.e. the contact potential results in an acceleration of the electrons as they fly through the analyzer. Consequently, the kinetic energy of all the electrons – primary and secondary – increases by $\Phi_s - \Phi_a$, which yields

$$E_{kin} = \hbar\omega - E_{bin} - \Phi s + \Phi s - \Phi a = \hbar\omega - E_{bin} - \Phi_a \tag{3.40}$$

If the work function of the analyzer is bigger than that of the sample, the electrons photo-emitted from the sample would be decelerated while passing the analyzer, but equation 3.40 would be the same. The reason for that is that the kinetic energy of primary electrons is not influenced by the work function of the sample (which is a result of the contact potential between sample and analyzer that compensates any change of the substrate work function), but they are influenced by the work function of the analyzer. The problem is that the work function of the analyzer is generally not known. The other difficulty is that all the photoelectrons which passed through the analyzer generate a number of secondary electrons on the impact with the analyzer detector, these are shown as the dotted area in Figure 3.14(A)–(D). The presence of analyzer secondaries "cut-off" can make it very difficult to determine the precise position of the sample secondaries "cut-off", which is necessary for the determination of the sample work function. However, applying sufficient negative potential to the sample, usually 15-30 V, one separates the secondary edges of the sample

and the analyzer shown in Figure 3.14(C).

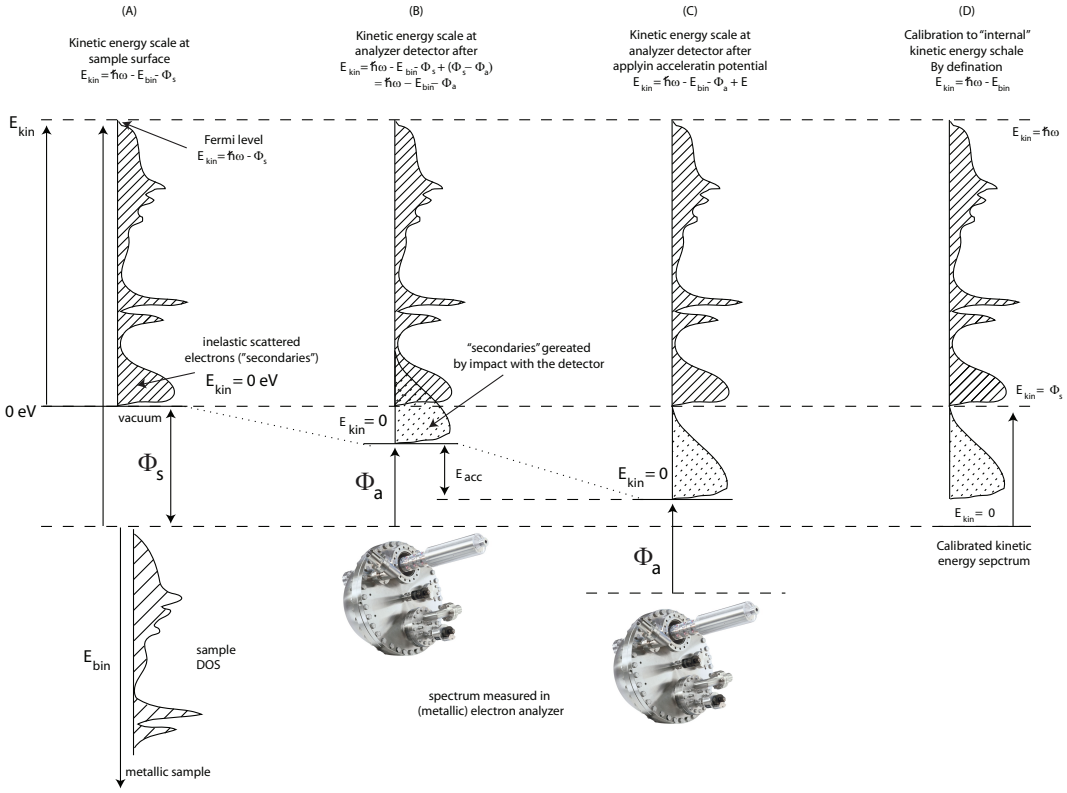

Figure 3.14: Schematic of the photoelectron process energetics. (A) directly at the sample surface. (B) at the analyzer detector. (C) at the analyzer detector in the presence of accelerating potential. (D) after definitive calibration by the Fermi level position.

Finally, the kinetic energy of the fastest electrons observed is set by definition as $E_{kin} = \hbar\omega$, which puts the binding energy axis origin onto the Fermi level with $E_{bin} = 0$. Upon such calibration, all features of the spectrum appear at their kinetic energies before the respective electrons left the sample, Figure 3.14(D). This process also shifts the sample secondary edge "cut-off" to a kinetic energy corresponding to the work function of the sample, since the "cut-off" represents the electrons that had just enough energy on arrival at the surface to overcome the sample work function. The binding energy of the secondary cut-off is then $E_{bin} = \hbar\omega - \Phi_s$. Therefore, the work function of the sample can be easily determined by subtracting the binding energy of the cutoff from the photon energy.

Last but not the least, setting the binding energy of the Fermi level to zero,

one also avoids the errors in determination of photon energy (hence binding energy) provided by a monochromator, if non-monochromatic (e.g. synchrotron) radiation is used. In the present work such calibration was performed by measuring the position of the Fermi level of the sample with the same photon energy as for the core-level.

3.9 Beamlines

The synchrotron radiation used in this work has been monochromatized and delivered to the experimental end-station and focused on the sample. This is done by the beamline, containing the monochromator, X-ray optics and sets of precision slits.

Beamline D1011

Beamline D1011 is a MAX II bending magnet beamline, designed for probing the core-levels of light elements, such as carbon, nitrogen, oxygen, silicon, etc. and covering the photon energy range from 30 to 1500 eV with high energy resolution. The monochromator is a modified plane grating Zeiss SX-700 with a groove density of 1200 mm^{-1}.[163, 164] The degree and type of the radiation polarization at this beamline can be controlled by the extra pair of quadrupole magnets fitted on the bending magnet, allowing vertical tilt of the electron orbit within the magnet. In the tilted orbit the emitted radiation takes an elliptical polarization, while in the non-tilted electron orbit it can be regraded as linearly polarized. The degree of polarization is dependent on the actual tilt. This facility promotes the investigation of magnetic properties of material within the technique of X-ray magnetic circular dichroism. This technique is founded in the presence of different absorption cross-section in magnetic materials for deferent light polarization. This technique was not employed in this work, so will not be discussed in further detail.

The two end-stations of beamline D1011 are both designed for spectroscopy, and the back chamber can also facilitate magnetic studies. In this work only

the front chamber was use. The front end-station is equipped with a Scienta SES-200 hemispherical electron spectrometer, and a MCP detector for measuring XAS partial electron yield. Furthermore a mass-spectrometer and a unit for observing low energy electron diffraction pattern is fitted. There are no refocusing optics between the exit slit of the beamline and the front end-station chamber, resulting in a relatively large spot size of the beamline, around 2 mm $\times$ 1mm. Highly homogeneous samples are therefore desired before experiments can be conducted at this beamline. The energy resolution of the beamline depends on the exit slit, where the monochromatized radiation is focused. The back end-station chamber was not employed in this work, and will therefore not be discussed.

Beamline I311

Beamline I311 also features the "two end-station design", where the first end-station is a conventional UHV set-up for spectroscopy studies, and in the greater perspective similar to the equipment and design found at beamline D1011. The energy range covered by beamline I311 is similar to that of D1011, and beamline I311 also consists of a modified plane-grating SX-700 monochromator form Ziess. The modification allows interchangeable gratings for different photon energy ranges. The insertion device that deliver the X-ray radiation at beamline I311 is from a hybrid-permanent magnet type undulator. This beamline can deliver a much higher photon flux to the sample, and thereby increase the energy and spatial resolution. This is done by the refocusing optics at the exit slits. The energy resolution depends on a number of parameters like slit widths, undulator gap and photon energy. Normally they are of the order of $\frac{E}{\Delta E} \approx 2000$ to 20000. At a photon energy of 340 eV this provides the best energy resolution for the C $1s$ of around 20 meV. The refocusing optics in the front chamber provides a spot size on the sample of 500 μm $\times$ 100 μm.

Beamline SEXTANS

The undulator beamline SEXTANS at the French national synchrotron facility, SOLEIL, Paris, consists of three experimental work areas. An inelastic scattering branch, and two elastic scattering branches. Only the inelastic scattering were employed in these studies. This branch is designed for detailed analysis of radiative decay channel following a resonant excitation and for the investigation of low-laying excitations associated with the ground state, analogous to optical spectroscopy, with element selectivity (intermediate state core-hole). Furthermore it strongly correlated – magnetic – materials can be investigated.

The SEXTANS beamline covers the photon energy range from 50 to 1700 eV with high energy resolution, with an estimated sample at 1×10^{14} photons per second, providing a beam spot size of 80 μm$\times$2μm. The branch line is equipped with a high-efficiency 1024$\times$1024 13 μm pixel back-illuminated CCD detector held in a fixed position. The energy range is selected by adjusting the grating angle using an encoded sine-bar drive, resulting in precise and straightforward energy calibrations.

3.10 Resonant Inelastic X-ray Scattering

There are other relaxation processes possible in the core excited state that we have not discussed yet. So far we have treated the core-hole decay as an emission of an Auger electron, but an emission of photons is also possible – a photon-in-photon-out process. This emitted photon will be a scattered photon and it is in principle possible to determine the momentum, energy, and polarization of this photon.[26] In the experimental setup it is possible to chose the momentum, energy, and polarization of the incident photon, so it will resonate with one of the atomic X-ray transitions of the system. Measuring the difference in these physical properties to the emitted photon provides information about the system. Choosing the correct resonance it is possible to enhance the inelastic scattering cross section by many orders of magnitude, and infor-

mation about charge, magnetic properties, and orbital degrees of freedom of the system can be gathered.[165] This synchrotron based technique is called resonant inelastic X-ray scattering, RIXS.

The first step in RIXS shares a resemblance with the aforementioned techniques of RPES and XAS. The incoming photon will be absorbed and the system will be in the highly energetic and unstable state, due to the presence of a core-hole, and shortly after the system will decay and fill the core-hole. Here the similarities more or less end. In the RIXS process the core-hole will be filled with an electron simultaneously emitting a photon. The decay process becomes a fluorescent decay. In this picture the electron that provides the core-hole decay can originate from a different state within the valence band decay. For this to happen, both the photoelectric transition – the initial one from the core to the valence state and the succeeding one from the valence state that annihilates the core-hole – must be possible. Consequently RIXS leaves the system in a neutral final state, while PES ends in a final ionized state. In PES the binding energy of the electron is therefore shifted and the orbitals in the ground states are not represented at the correct energy position. In this technique the emitted Auger electron from anywhere on the molecule provides the information of the complete density of states for the occupied valence band. This is contrasted by RIXS where the initial and final state are neutral and the state are much better represented by RIXS compared to the technique of PES[26]. The highly localized core-hole on the atom, can only be filled by valence electrons if a spatial overlap between the valence band orbitals and the orbitals of the core-hole is present. This provides the element specificity of the RIXS technique. These photo-electric transitions between the core, the core excited state and the succeeding core-hole decay must be possible before applying the RIXS. This means that only certain transition are allowed. Within the constraint of conserving spin and angular momentum during the decay (dipole selection rule) $\Delta = \pm 1$ and $\Delta S = 0$ need to be fulfilled. As an example the initial dipolar transition of $1s \rightarrow 2p \rightarrow 1s$ in the wide band-gap insulator is possible, and happens at the K-edge of oxygen, carbon, nitrogen,

and silicon.[165] Within the study of organic molecules RIXS therefore become a very useful tool to employ. By monitoring the N $1s$ resonance RIXS spectra information about the σ and π orbitals for the atom can be provided.

It has been shown[25] that the core-hole clock implementation can be adopted within the technique of RIXS. This allows a new refined way to study the charge transfer dynamics between semiconductor surfaces and organic molecules. A reduction of the intensity of the elastic peak between the multilayer and the monolayer is present if an electron is transferred into the substrate. Comparing the intensity of the elastic peak for different photon energies, corresponding to the bound states resonances between the multilayer and the monolayer, thereby provides the information of the charge transfer. It is the elastic peak for the monolayer that will experience the reduction. Along the lines of retrieving the charge transfer information of RPES spectra, the intensity of the participator decay is found in RIXS by considering the proportion of the decay the occurs due to elastic scattering instead of inelastic scattering. Normalising the areas, A, of the elastic peaks, and considering them in the same way as for the intensities of the participator decay we obtain by equation 3.30 the charge transfer time for RIXS:

$$\tau_{CT} = \tau_{chd} \frac{A^{\text{elastic}}_{\text{Monolayer}}}{\left(A^{\text{elastic}}_{\text{Multilayer}} - A^{\text{elastic}}_{\text{Monolayer}}\right)} \tag{3.41}$$

If the LUMO is located within the band-gap of the semiconductor, charge transfer is a forbidden transition and again we can use the state as a benchmark for normalization, since charge transfer must arise from higher laying LUMO+n states. Normalizing the areas for the LUMO+n states in equation 3.41 we obatain:

$$\tau_{CT} = \tau_{chd} \frac{\frac{A^{\text{LUMO+n}}_{\text{Monolayer}}}{A^{\text{LUMO}}_{\text{Monolayer}}}}{\frac{A^{\text{LUMO+n}}_{\text{Multilayer}}}{A^{\text{LUMO}}_{\text{Multilayer}}} - \frac{A^{\text{LUMO+n}}_{\text{Monolayer}}}{A^{\text{LUMO}}_{\text{Monolayer}}}}. \tag{3.42}$$

Chapter 4

XAS studies of single molecule magnets on TiO_2(110) and Au(111) surfaces

4.1 Introduction

The search for novel magnetic materials for the electronics industry has, in recent years, focused on single molecule magnets (SMMs) due to their potential as an active component within nanoscale information storage devices,[60] spintronics[61] and quantum computation.[62–64] Single molecule magnets are so-called as they exhibit a range of intrinsic magnetic properties which originate from a purely molecular basis.[85, 166] One of the properties that makes SMMs fundamentally different from traditional bulk magnets is their ability to show slow relaxation of the magnetization after application of a magnetic field. SMMs typically consist of a molecular framework of transition metal atoms arranged in such a way that their spin carrying atoms interact and allow description as a single large spin.[76]

The focus of this chapter is the single molecule magnet architecture based on the $Mn_{12}O_{12}$ core cluster, as shown in Figure 4.1. The mixed valence dodecamanganese (III, IV) core contains four Mn^{4+} ions at the core and eight Mn^{3+} ions around the periphery. The four Mn^{4+} ions each have a spin of

3/2 while the eight Mn^{3+} ions each have a spin of 2, leading to a total spin of 10.[76] This particular single molecule magnet core surrounded by acetate ligands has been widely studied in recent years.[75, 76, 86–88] One of the reasons for the great interest in this molecule arise from its property of showing bistability,[85] which makes it a potential candidate for magnetic storage devices.[62] The organic shell consisting of 16 ligands is crucial in maintaining the correct manganese oxidation states. The most widely studied example[74, 76] is $Mn_{12}O_{12}(CH_3COO)_{16}(H_2O)_4$, herein referred to as Mn_{12}(acetate)$_{16}$, but the carboxylate ligands can be modified by conventional wet chemistry techniques, such as direct synthesis from the appropriate carboxylate reagents[90] or ligand exchange.[85, 91, 92]

In order to make practical use of the intrinsic magnetic properties of these molecules it is important to be able to deposit them intact on suitable surfaces. Several studies have explored techniques for the transfer of SMMs onto various substrates. For example SMMs functionalized with sulfur containing organic ligands have been transferred from solution onto a Au(111) surface,[86, 91, 167–170] and carboxylate-terminated self-assembled monolayers have been used to bind SMMs to flat surfaces and polymer sheets.[171] An alternative route is to pre-functionalize both the substrate and the SMM to encourage electrostatic interactions[172, 173] which are used to attach the molecules to the surface. Pulsed laser deposition (PLD),[174] matrix assisted pulsed laser evaporation (MAPLE),[175] a pulsed vacuum spray (PVS) technique,[176] and a local mechanical method[177] have been implemented to facilitate the deposition of SMMs onto substrates held in ultra-high vacuum (UHV), although fragmentation and damage of the manganese oxide core is frequently observed.[174–176, 178]

From previous studies conducted by Saywell *et al.*[74] the Mn_{12}(acetate)$_{16}$ molecule and the related Mn_{12}(benzoate)$_{16}$ molecule have been investigated on the Au(111) surface. Here they employ the technique of XAS to investigate if any reduction of the magnetic core will occur when the two molecules are deposited on the gold surface. Their result are displayed in Figure 4.2

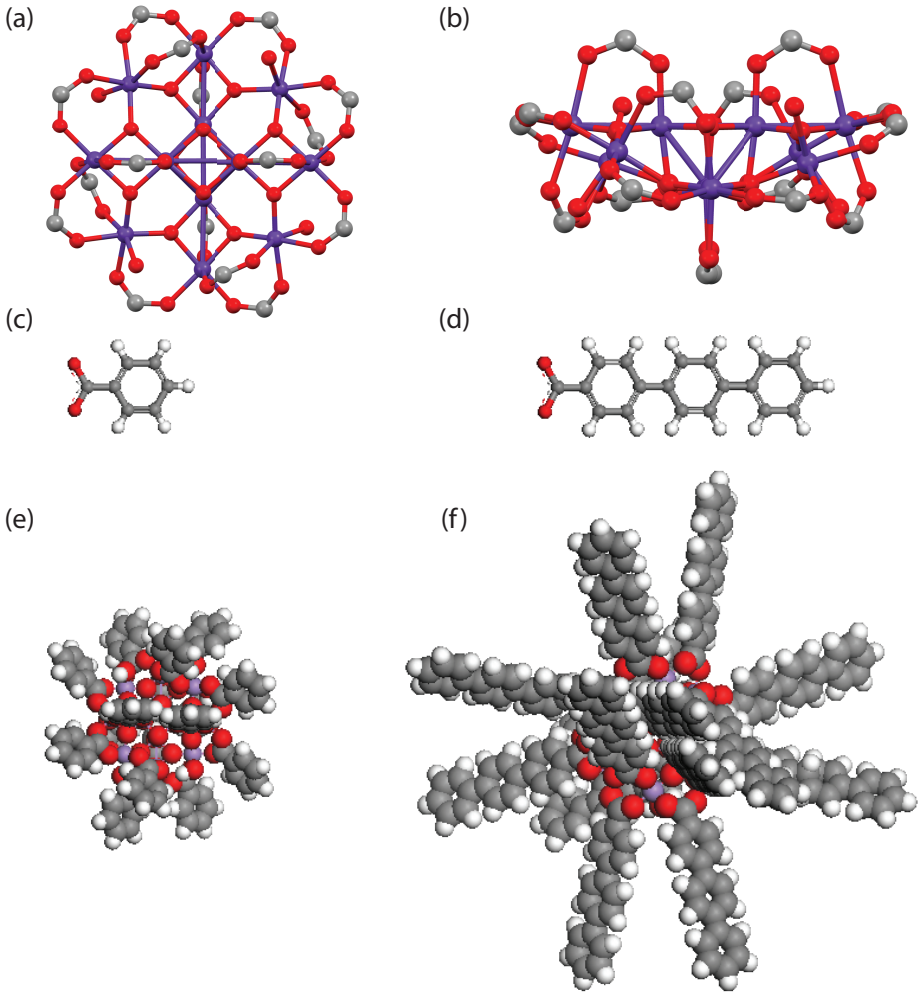

Figure 4.1: (a) and (b) views of the dodecamanganese (III, IV) cluster. The carbon within the carboxylate anchor of a ligand is shown as a grey sphere. Eight of these are shown around the perimeter of the molecular view in (a) and four above and below the molecular view in (b). The purple and red spheres represent the manganese and oxygen within the cluster respectively. The two ligands benzoate (c) and tpc (d) are also shown. The representations of (e) $Mn_{12}(benzoate)_{16}$ and (f) the larger $Mn_{12}(tpc)_{16}$ are shown in the space-filling representation.

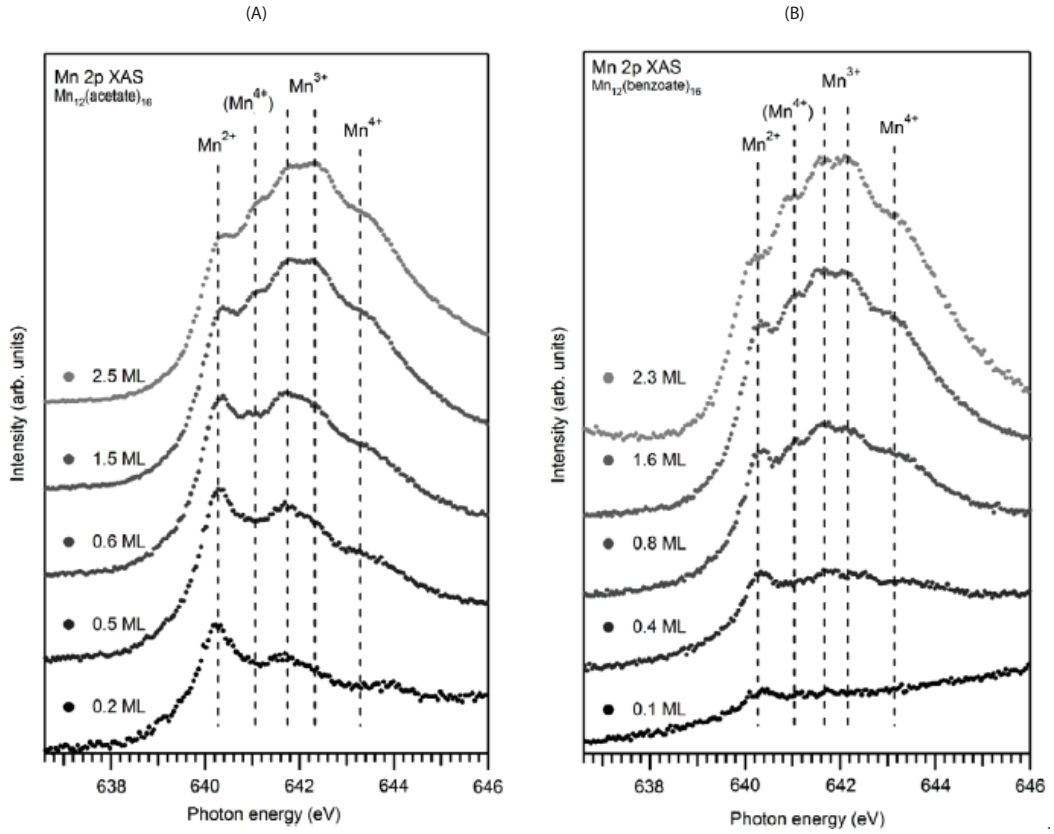

Figure 4.2: (A) Mn $2p$ X-ray absorption spectra measured for a range of coverages from 0.2 monolayer (ML) to 2.5 ML of $Mn_{12}(acetate)_{16}$ on the Au(111) surface. (B) Mn $2p$ x-ray absorption spectra measured for a range of coverages 0.1 ML to 2.3 ML of $Mn_{12}(benzoate)_{16}$ on the Au(111) surface. The positions of the peaks corresponding to the presence of the Mn^{2+}, Mn^{3+} and Mn^{4+} oxidation states are labelled. Reproduction after reference [74].

The results show that for both molecules the Mn^{3+} and Mn^{4+} oxidation states are not present in the sub-monolayer regime. They conclude that the acetate and benzoate ligands shells do not offer sufficient protection of the magnetic core when adsorbed on the surface. With their results, our motivation is therefore to introduce a bigger and more bulkier ligand in that of the terphenyl-4-carboxylate ligand, as shown in Figure 4.1d, in order to investigate the effect that modifying the protective shell around the magnetic core of the SMM has on preventing a change in the oxidation states of the Mn atoms when adsorbed on a surface. Furthermore we introduce a different surface in that of the rutile $TiO_2(110)$ described in Chapter 1.

Here we have used the non-thermal technique of UHV electrospray deposition (UHV-ESD), which our group[74, 75] and others[76] have previously

demonstrated for the deposition of Mn_{12}(acetate)$_{16}$ onto a Au(111) surface for synchrotron radiation based electron spectroscopy and scanning tunneling microscopy (STM). While STM and photo-electron spectroscopy data suggest that the SMMs were deposited intact on the Au(111) surface, the Mn^{3+} and Mn^{4+} oxidations state are not preserved at sub-monolayer coverage.[74, 75] Introducing the larger benzoate ligand,[74] shown in figure 4.1e, still results in a partial reduction of the magnetic core on the Au(111) surface. However, studies of Mn_{12}(acetate)$_{16}$ deposited by UHV-ESD on an insulating boron nitride (BN) surface[76] show that the magnetic properties of the molecule can be preserved, suggesting that electronic decoupling of the molecule from the surface is required. In this chapter we report on the deposition of Mn_{12}(benzoate)$_{16}$ and Mn_{12}(terphenyl-4-carboxylate)$_{16}$, herein referred to as Mn_{12}(tpc)$_{16}$ on the non-metallic wide band gap semiconductor surface of rutile TiO_2(110) and on the metallic Au(111) surface in order to assess the effect of changing the size of the protective ligand shell and the nature of the underlying substrate on the oxidation states of the magnetic core.

4.2 Experimental Method

Beamline D1011 at the MAX-lab synchrotron radiation facility was used to perform photoemission and X-ray absorption spectroscopy (XAS) measurements. The surfaces were in the form of a Au(111) single crystal (3 x 10 mm diameter) and a rutile TiO_2(110) single crystal (10 x 10 x 1 mm). The Au(111) crystal was cleaned by cycles of sputtering 1 kV Ar^+ ions followed by annealing at 900 K by passing a current through the tungsten wire mount.[95] Surface contamination was assessed by monitoring the C 1s core level photoemission peak. TiO_2(110) was cleaned using the same sputter procedure as Au(111) with annealing to 900 K using a pBN heater mounted behind the crystal. The monochromator exit slits of the beamline were set to give a resolution of 100 meV for photons of 640 eV energy. X-ray absorption spectra were measured using a partial yield detector (100 V retardation) and the photon energy scale

was calibrated from the separation between the Ti $2p$ or Au $4f$ peaks measured with 1^{st} and 2^{nd} order radiation.

The single molecule magnets were deposited using a commercial *in-situ* UHV electrospray deposition source (Molecularspray, UK). Mn_{12}(benzoate)$_{16}$ was deposited from a solution of 1 mg of molecule in 10 mL of pure methanol. Mn_{12}(tpc)$_{16}$ was deposited from a 1:10 solution of methanol and dichloromethane at the same concentration. The liquid is delivered under a sufficient pressure to a hollow stainless-steel emitter held at 1.9 - 2.5 kV. At this potential the liquid becomes ionized and a plume emerges consisting of multiply charged droplets. The plume enters a series of differentially pumped molecular beam skimmers via a grounded entrance capillary (5 cm long with 0.25 mm internal diameter), gradually losing solvent molecules through evaporation and a cascade of Coulomb fission events. This deposition technique is described in greater detail elsewhere[23] and has been successfully used to deposit a range of complex organometallic molecules (including SMMs) previously.[56, 74, 127, 129] A UHV gate valve separates the electrospray system from the preparation chamber. With the valve closed the base pressure of the preparation chamber was in the low 10^{-10} mbar range. With the gate valve open, but the emitter voltage off and thus no electrospray process occurring, the pressure in the preparation chamber was in the low 10^{-8} mbar range. When the electrospray process was carried out the pressure in the preparation chamber rose to the mid 10^{-7} mbar range, the additional pressure being due to residual solvent molecules in the molecular beam. The deposition spot from the electrospray source is circular shaped with a gaussian profile. With this profile it is possible to produce a surface coverage gradient, calibrated by comparing the attenuation of either the Au $4f$ or the Ti $2p$ to that of the respectively clean substrates, with the mean free path through the molecular magnets calculated using the Seah and Dench model.[136]

4.3 Results and discussion

Figure 4.3 shows the Mn $2p$ (L-edge) XAS spectra of the Mn_{12}(benzoate)$_{16}$ molecule adsorbed on the rutile TiO_2(110) surface. The figure demonstrates how the different absorption peaks develop as a function of the coverage, from 0.03 monolayers (ML) in the bottom spectrum, to 2.9 ML in the top spectrum. At low coverage the spectrum is dominated by a distinct peak at 640.3 eV, but as the coverage increases to 2.9 ML two peaks at 641.7 eV and 642.3 eV respectively grow in intensity and two shoulders develop at 641.2 eV and 643.3 eV. Based on the results of Voss *et al*[179, 180] we can assign the dominating peak in the sub monolayer regime at 640.3 eV to the Mn^{2+} oxidation state, the absorption energy of which has been identified by comparison with stoichiometric manganese oxide (MnO). At a coverage of 1.9 ML the magnetic core shows some indication of retaining the correct oxidation states for the Mn_{12}(benzoate)$_{16}$ cluster with relatively strong absorption peaks at the expected energies of Mn^{3+} and Mn^{4+} as indicated on the figure. These features dominate at a coverage of 2.9 ML suggesting that spectra at the two highest coverages comprise signals from the reduced molecules in contact with the surface in the first adsorbed layer, and pristine molecules in the second and third layers. These results are very similar to our previously published data for the Mn_{12}(benzoate)$_{16}$ molecule adsorbed on a Au(111) surface.[74] This data suggests that the first layer of adsorbed molecules is sufficient to protect subsequently adsorbed SMMs, but that the benzoate ligand shell itself is not large enough to protect the first adsorbed layer on either a TiO_2 or Au surface. The data does however suggest that a ligand shell bulky enough to emulate the first layer of molecule would be sufficient to allow us to deposit pristine SMMs on the surface.

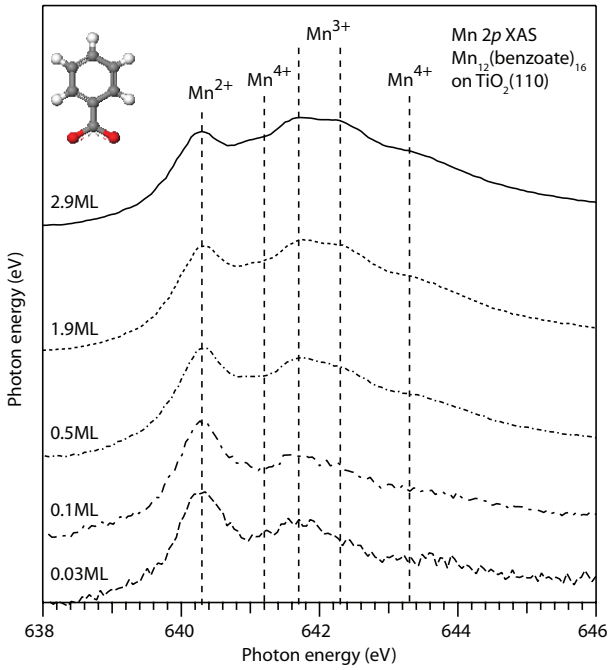

Figure 4.3: Mn $2p$ (L-edge) X-ray absorption spectra measured for a range of coverages (0.03-2.9 ML) of $Mn_{12}(benzoate)_{16}$ on the rutile $TiO_2(110)$ surface. The vertical lines indicate the peaks attributed to the presence of the Mn^{2+}, Mn^{3+} and the Mn^{4+} oxidation states at each coverage.

The effect of the ligand shell was explored by substituting the benzoate ligands for terphenyl-4-carboxylate ligands to form the $Mn_{12}(tpc)_{16}$ SMM as shown in figure 4.1. The Mn $2p$ (L-edge) XAS spectra for $Mn_{12}(tpc)_{16}$ on the $TiO_2(110)$ surface is shown in Figure 4.4 for surface coverages ranging from 0.4 - 2.8 ML. The spectrum for the highest coverage of 2.8 ML closely resembles the spectrum of bulk $Mn_{12}O_{12}$-based molecules with dominant peaks at the energies expected for the Mn^{3+} and Mn^{4+} oxidation states.[179, 180] At lower coverages the shape of the spectra do not change significantly compared to the previously discussed benzoate molecule. Even at the lowest coverage of 0.4 ML the spectrum is still dominated by the expected lineshape of the pristine single molecule magnets. These results strongly suggest that the bulkier tpc ligand is sufficiently large to protect the core, at least in terms of the oxidation states of the manganese atoms necessary for the magnetic functionality of this molecule, on the oxide surface. Furthermore we find the Mn^{3+} and Mn^{4+} oxidation states

at higher absorption energies, for the intact manganese core which may also be a result of isolation from the surface. The shoulder observed at the expected Mn^{2+} absorption energy might actually be an intrinsic feature from the Mn^{3+} and Mn^{4+} oxidation states similar to that seen for bulk $Mn_{12}(acetate)_{16}$.[179, 180]

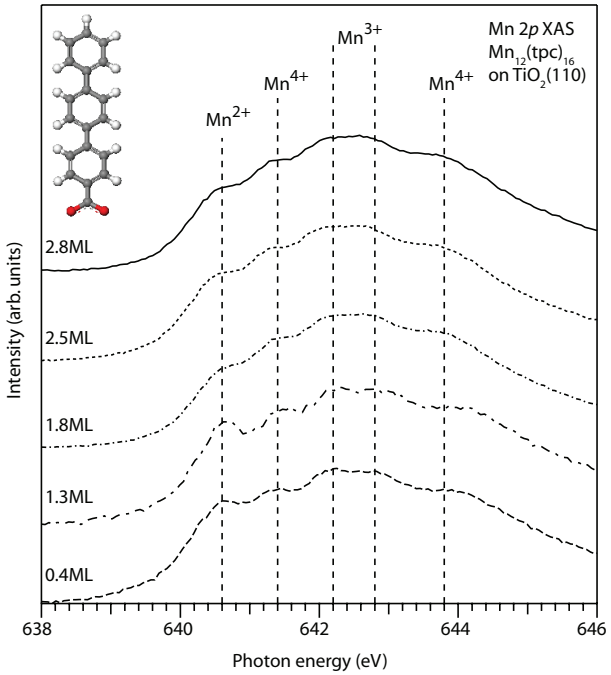

Figure 4.4: Mn 2*p* (L-edge) X-ray absorption spectra measured for a range of coverages (0.4-2.8 ML) of $Mn_{12}(tpc)_{16}$ on the rutile $TiO_2(110)$ surface. The vertical lines indicate the peaks attributed to the presence of the Mn^{2+}, Mn^{3+} and the Mn^{4+} oxidation states at each coverage.

To explore whether the protection afforded on the oxide surface by the larger tpc ligands can be extended to the metallic surface, analagous X-ray absorption spectra were measured for $Mn_{12}(tpc)_{16}$ adsorbed on Au(111), as shown in Figure 4.5. At all coverages (0.3 - 1.7 ML) we observe the dominant intensity in the absorption spectra at the photon energies expected for the Mn^{3+} and Mn^{4+} oxidations states. This suggests that the large tpc ligand has the ability to protect the magnetic core from substrate interactions even on the gold surface.

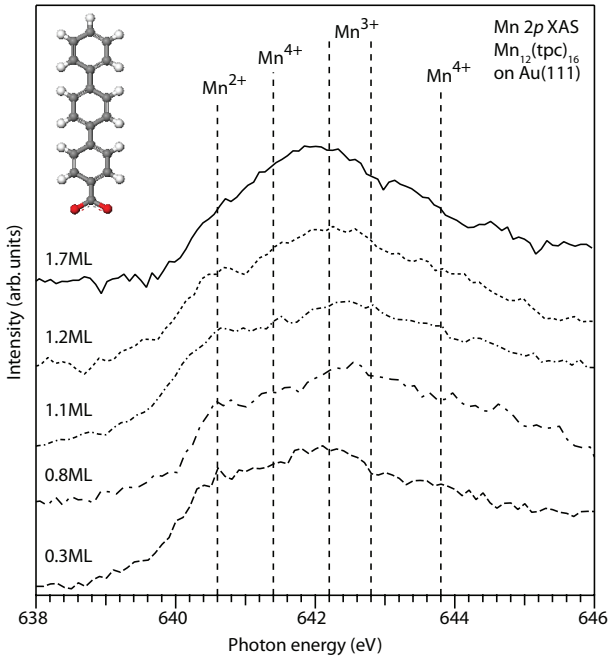

Figure 4.5: Mn $2p$ (L-edge) X-ray absorption spectra measured for a range of coverages (0.3-1.7 ML) of $Mn_{12}(tpc)_{16}$ on the Au(111) surface. The vertical lines indicate the peaks attributed to the presence of the Mn^{2+}, Mn^{3+} and the Mn^{4+} oxidation states at each coverage.

4.4 Conclusions

For a fully functional single molecule magnet adsorbed on a surface the magnetic core must not be compromised by any interaction (charge transfer or chemical) with the surface itself. In the case of the $Mn_{12}(benzoate)_{16}$ on the $TiO_2(110)$ surface we see a strong Mn^{2+} peak in the sub-monolayer regime, while for higher coverages the spectrum is dominated by Mn^{3+} and the Mn^{4+}. This is indicative of a chemical or charge transfer interaction between the directly adsorbed SMMs and the surface that cannot be prevented by the benzoate ligand shell on $TiO_2(110)$ as previously found for Au(111). Conversely, our results from the adsorption of $Mn_{12}(tpc)_{16}$ on both the rutile $TiO_2(110)$ and Au(111) surfaces exhibit clear signatures of the Mn^{3+} and Mn^{4+} oxidations states of the pristine SMMs. We conclude that the terphenyl-4-carboxylate ligand is large enough to provide a substantial degree of protection for the

oxidation states within the magnetic core when these molecules are adsorbed on gold and titanium dioxide surfaces. This is a necessary but not sufficient condition for the magnetic functionality of the molecules to be retained. Mannini *et al*[181] have shown that thin films of single molecule magnets might not always exhibit the magnetic properties of their bulk counterparts due to molecular distortions. Our studies continue to pursue further characterisation of the magnetic properties of these protected cores.

Chapter 5

RIXS of Bi-isonicotinic acid on a rutile TiO_2(110) surface

5.1 Introduction

In this chapter the system of bi-isonicotinic acid molecule adsorbed on the rutile TiO_2(110) surface is explored. This system is of particular importance as it acts as a model interface for the Grätzel solar cell [18], addressed in Chapter 1. The bi-isonicotinic acid and the "N3" molecule are shown in Figure 5.1A and Figure 5.1B respectively. The understanding of the electronic properties that enable the system to give the DSSCs such a high incident-photon-to-current conversion is a key step for further development within this branch of renewable energy. The system has been extensively studied with in the technique of resonant photoemission spectroscopy,[15–22] where one of the key discoveries is the bonding between the bi-isonicotinic acid and the TiO_2 substrate. The molecule will make a strong 2-M bidentate coupling obtained by the deprotonation of the carboxylic acid groups, which provides a suitable spatial overlap between the orbital of the molecule and the unoccupied density of states for the surface.[16] It has been shown that this efficient coupling between the molecule and the substrate facilitates an ultra-fast charge transfer in the low femto-second time scale.[18] The work presented here employs the technique of resonant inelastic X-ray scattering (RIXS) for an investigation of the bi-

isonicotinic acid on the rutile $TiO_2(110)$ surface. It should be mentioned that this is largely a re-exploration of this setup when this technique[25] is applied, but here we present measurements of much higher resolution, approximately an order of magnitude and enable the discovery of new and not yet uncovered properties for this highly important system in the pursuit of sustainable energy sources.

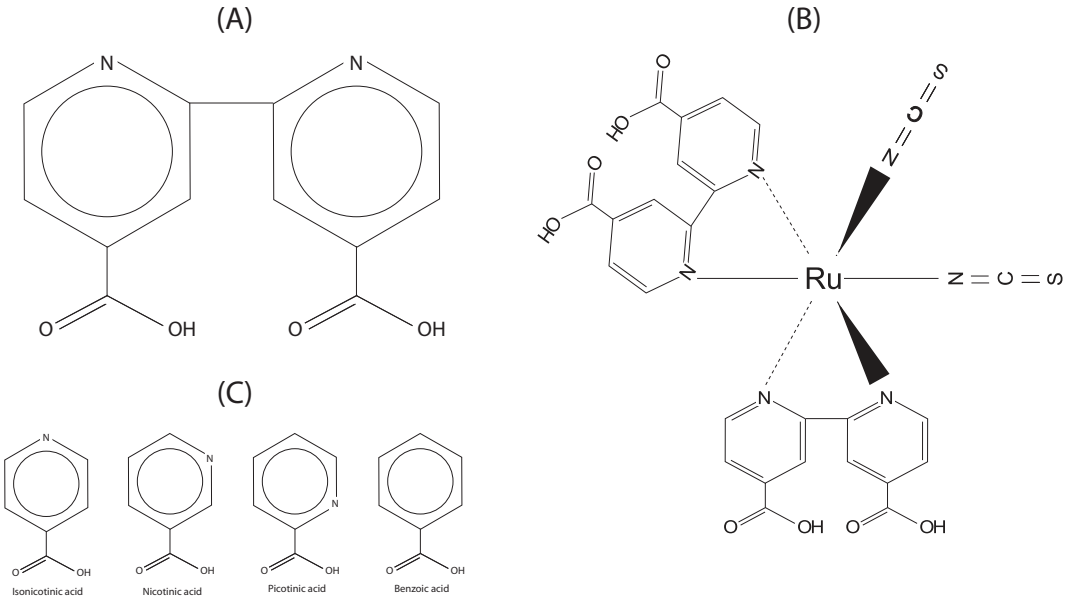

Figure 5.1: Schematic representation of the bi-isonicotinic acid (A) and the "N3" molecule (B) [128]. Note the "N3" molecule consists of two bi-isonicotinic acid ligand, which both can support as anchor groups.

5.2 Experimental Method

Experiments were conducted at the SEXTANS beamline located at the national French synchrotron facility SOLEIL in Paris. The beamline has a photon energy range of 50–1700 eV and is equipped with a high resolution grating X-ray spectrometer AERHA [182]. The radiation has a high degree of elliptical polarization and may be considered as linearly polarized for the purposes of this study. During measurements the pressure in the analysis chamber was in the low 10^{-10} mbar range.

During preparations the substrate, a rutile TiO_2(110) single crystal of dimensions 5mm×8mm×1mm, was mounted on a 25mm×25mm molybdenum sample plate, ensuring good electrical and thermal contact with the sample holder. X-ray photoemission spectroscopy (XPS) was used to monitor the development of the coverages of the bi-isonicotinic acid. During this process sample charging was likely to occur and to avoid this the sample was changed from a insulator to a n-type semiconductor by introducing bulk defects.[183] This was done through a series of sputter and anneal cycles with Ar^+ ion at 1 kV and heating to 800 K. Similar sputter and anneal cycles were used when the sample was cleaned. When the C 1s core-level signal from the sample, measured with XPS, were negligible the sample was deemed clean. All preparations and coverage calibrations of the samples were done in our own laboratory at the University of Nottingham, UK.

The bi-isonicotinic acid molecules were evaporated from a crystalline powder, in a Knudsen cell-type evaporator, at a temperature of 230 °C. Multilayers were prepared by exposing the sample to the evaporator for several minutes with the sample held at room temperature. The monolayer was estimated by the X-ray photon emission count rate normalized to the incoming photon flux and compared to the monolayer as previously reported in literature.[25]

During measurements at the SEXTANS beamline RIXS spectra where recorded between a photon energy of 360 eV and 420 eV. The RIXS spectra were acquired over a period of 300 seconds, while the sample was repeatedly

moved up and down within the 8 mm of the sample's length. This was done within a period of 12 seconds. After 300 seconds a new line on the sample was measured. The limitation of the RIXS acquisition time and the movement of the sample where employed to avoid beam damage of the molecule.[184] The beam damage was assessed by monitoring the spectra obtained by X-ray Absorption Spectroscopy measurements (XAS) in relevant positions. The XAS data were recorded in a fluorescence yield and the overall photon energy calibrated to the known energy of the bi-isonicotinic acid multilayer LUMO resonance at a photon energy of 398.8 eV.[21]

5.3 Results and discussion

Presentation of the XAS measurements

Within the core-hole clock implementation discussed in Chapter 2 at least one of the lowest unoccupied molecular orbitals needs to be located below the conduction band edge of the substrate. If this is fulfilled any charge transfer of these states will be forbidden and they will serve as a normalization point for when when potential charge transfer out of higher lying states are measured. In this particular study of the bi-isonicotinic acid molecule on the rutile TiO_2(110) the location of the substrate's density of states and the conduction band edge is found at a photon energy of 0.6 eV above the LUMO[18, 21], as shown in Figure 5.2. Therefore the LUMO state of the bi-isonicotinic acid cannot participate in the ultra-fast charge transfer.

Figure 5.3 displays the N 1s X-ray adsorption spectra for the monolayer and the multilayer of the bi-isonicotinic acid on the rutile TiO_2(110) substrate. In good correspondence to previous measurements[21, 25] the LUMO resonance is located at 398.8 eV, and LUMO+1 and LUMO+2 are present at 399.9 eV and at 402.7 eV respectively for the multilayer. In the case of the monolayer the LUMO, LUMO+1 and the LUMO+2 are found at similar photon energies. During measurements some off-resonance photon energies were chosen at 398.4

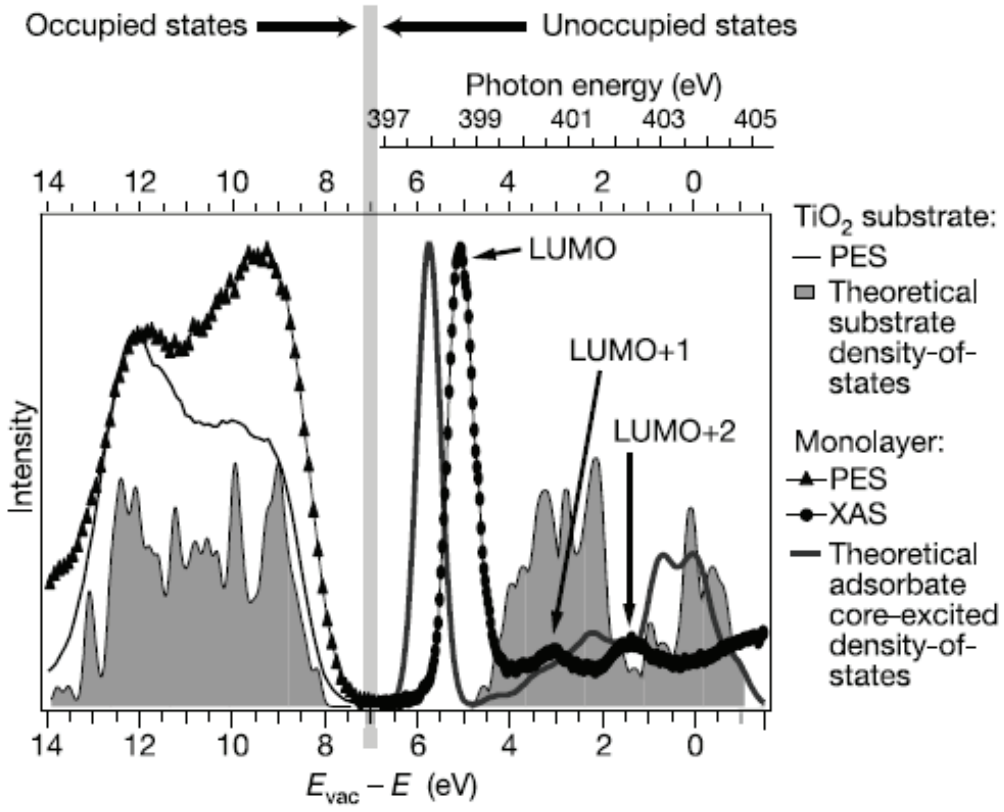

Figure 5.2: Density-of-states for bi-isonicotinic acid on TiO2(110): experimental monolayer density-of-states, experimental clean substrate occupied density-of-states, theoretical substrate density-of-states, and XAS calculation. Besides the common energy scale for XAS and PES[156], the photon energy scale for the experimental XAS is given. The LUMO of the excited system lies within the band gap, but the higher-lying states overlap the conduction band density-of-states. Electronic overlap is necessary for any electron transfer to take place. Reproduced from reference [18]

eV, 399.2 eV, 401.7 eV, and 405 eV respectively for the multilayer and at 405 eV in the case of the monolayer. All probed photon energies are indicated with red on the spectra.

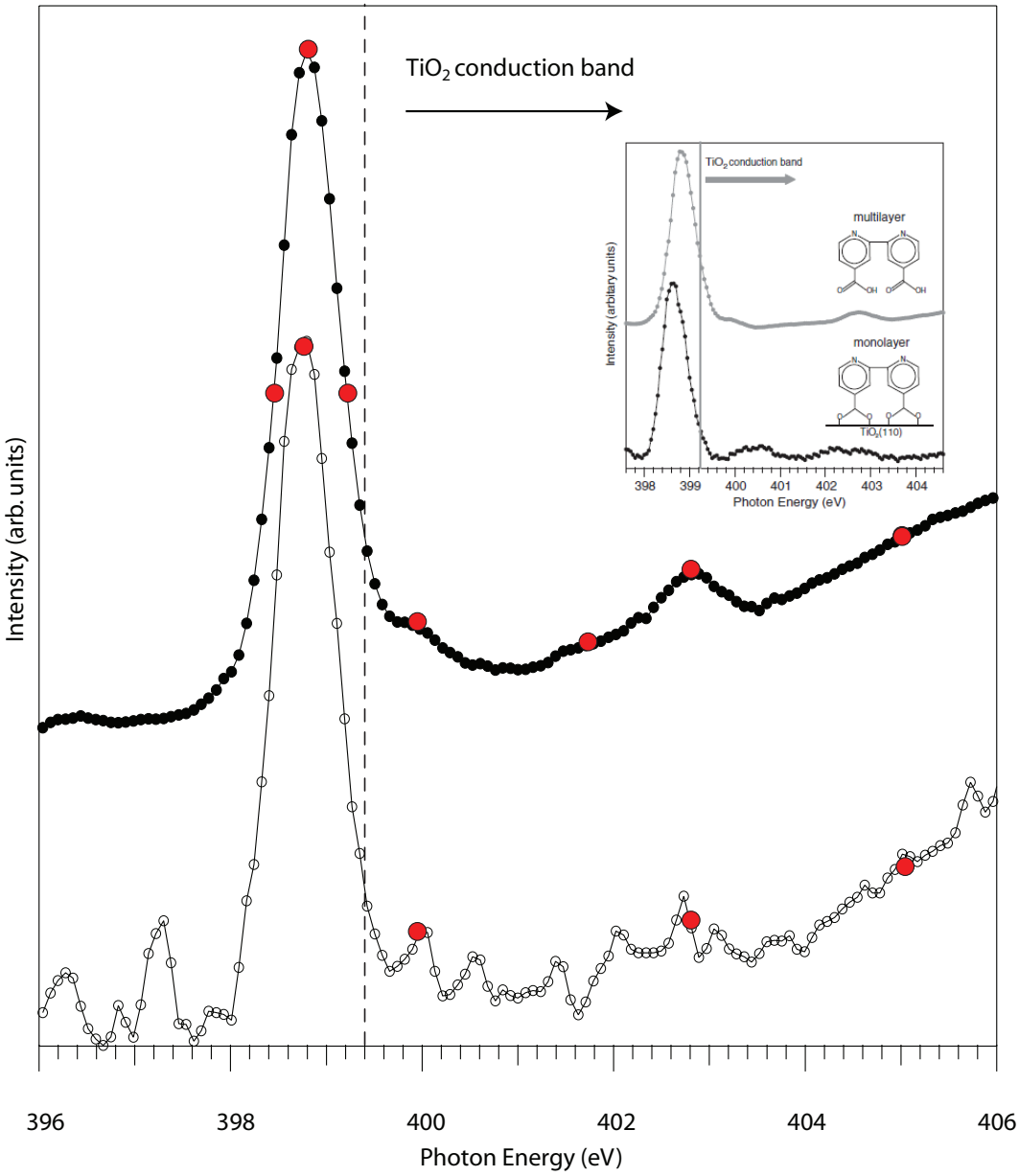

Figure 5.3: The N 1*s* *k* edge fluorescence yield X-ray absorption spectra for a multilayer and a monolayer of bi-isonicotinic acid, on the rutile $TiO_2(110)$ surface, normalized to the intensity of the LUMO resonance. The black dotted line shows the TiO_2 conductions band edge. The red dots on the multilayer spectrum indicates at which energies the system have been probed.

The dotted vertical line in Figure 5.3 is placed 0.6 eV above the LUMO resonance to indicate where the conduction band edge is located. Since the molecules are potentially isolated from the substrate in the multilayer none of the higher lying states (the LUMO+1 and LUMO+2) will participate in any

charge transfer. In the chemisorbed monolayer the LUMO+1 and LUMO+2 are overlapping with the unoccupied density of states of the substrate, and therefore ultra-fast transfer out of these states are expected in this experiment as previously measured in the related method of RPES.[18] The insert in Figure 5.3, that shows the N 1s XAS spectrum from the study of Britton *et al.*,[25] are shown to compare the good correspondence between our and those previous results.

Multilayer coverage and presentation of results

In Figure 5.4 the resonant inelastic X-ray scattering spectra are presented for each of the probed excitation energies. The dotted lines represent the off-resonance excitations energies, starting at 398.4 eV, 399.2 eV, 401.7 eV and ending at the top in 405 eV. The solid spectra represent as indicated the LUMO, LUMO+1, and LUMO+2 resonances. For the subsequent analysis all the spectra have been normalized to their total area. This enables us to compare the intensities of the peaks as a fraction of the total number of X-ray photons emitted in the core-hole decay.

The peaks present at a photon energy below 397 eV emitted photon energy originate from inelastic scattering, where the dominating peak at 393.8 eV represents the highest occupied molecular orbital (HOMO) of the bi-isonicotinic acid molecule projected out of the probed N 1s core-level. The HOMO at 393.8 eV might not be in the right position and might be projected onto the valence band. This will be evaluated further on. The peaks found at a lower photon energy than the HOMO resonance do not disperse with excitation energy, however intensity shifts within the inelastic scattering of the HOMO are present. This is being evaluated in Figure 5.5. This figure shows the resonant inelastic X-ray scattering only for the LUMO, LUMO+1 and the LUMO+2 to illustrate that the shape of the peak of the HOMO resonance clearly changes with excitation energy.

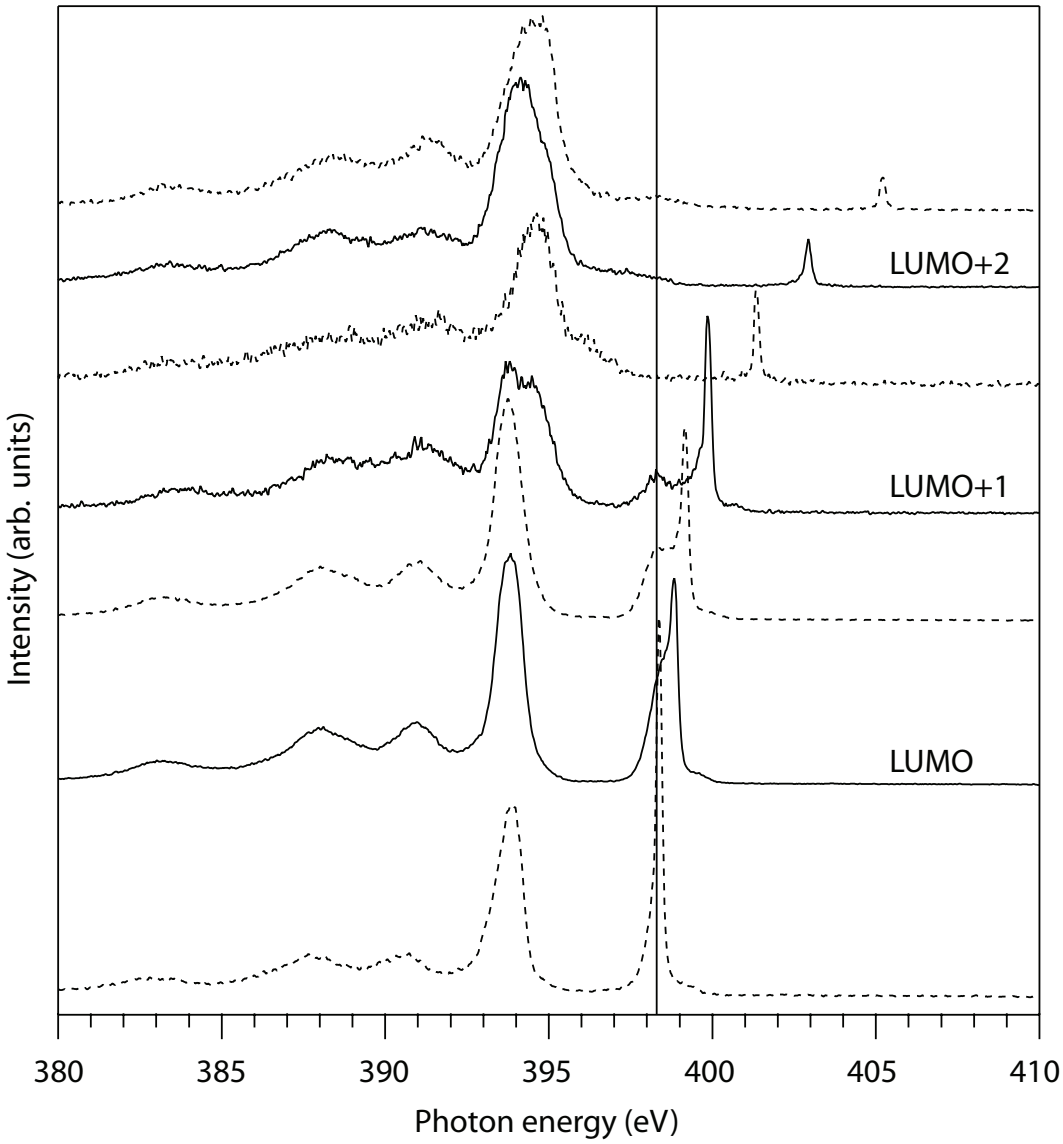

Figure 5.4: A montage of spectra for each of the probed photon energies. The LUMO (398.8 eV), LUMO+1 (399.9 eV) and LUMO+2 (402.7 eV) are indicated with solid lines. The measured off-resonance photon energies are 398.4 eV, 399.2 eV, 401.7 eV, and 405 eV respectively and are all indicated by dotted lines. The vertical solid is placed at a 398.4 eV to guide the reader's eyes. This feature at this energy will be discussed later on.

The spectrum for the valence band for the molecule has been projected on top of LUMO, LUMO+1 and LUMO+2 spectra and is indicated as a dotted line in Figure 5.5. The valence band were placed and calibrated along the lines as explained in Chapter 3. It is clear that the valence band does not line up with the peaks of the LUMO and LUMO+2 spectra. In the case of the LUMO+1 a split of the peak has occurred. One major part is still present at

393.8 eV and a second part is shifted 0.8 eV up to 394.7 eV, which lines up with the valence band. This split is still present when the LUMO+2 resonance is probed, but the ratio between the two peaks has changed. This split might be due to a different spatial overlap between the LUMO, LUMO+1 and LUMO+2 resonances and the occupied state involved in the resonant inelastic scattering process. Alternatively, it might be due to the two ring structure (shown in Figure 5.1A) of the bi-isonicotinic acid where a core-hole induced on one of the rings breaks the symmetry of the molecule leading to different orbital distributions and overlaps.

At higher photon energies well above the HOMO state, the elastic peak is found for each of the probed resonances. Regardless of the excitation energies each of the elastic peaks always displays a contribution at a higher energy then the probed resonance. This is especially notable at the low excitation energies from 398.4 eV up to the LUMO+1 resonance. This is not a real contribution to the measurements since nothing should be detectable above the emission energies and originates from the shape of the beam imaging profile emerging from the monochromator optics, and could potentially be filtered out by a series of small apertures. Applying the apertures in the attempt to remove this artificial contribution where done, but it resulted in severe losses of the wanted measurements, and was therefore left out for the final data acquisition. This artifact of the spectra was not included in the curve fits when the subsequent analysis where performed.

Discussion of the elastic peaks for the multilayer coverage

The elastic peaks disperses with excitation energy and displays the highest intensity near the LUMO resonance. The intensity of the elastic peak slowly decreases as the photon energy is increased. At high photon energies the system will be closer to the continuum and the probability for the photon to participate in the RIXS process will be low, therefore the decrease of the

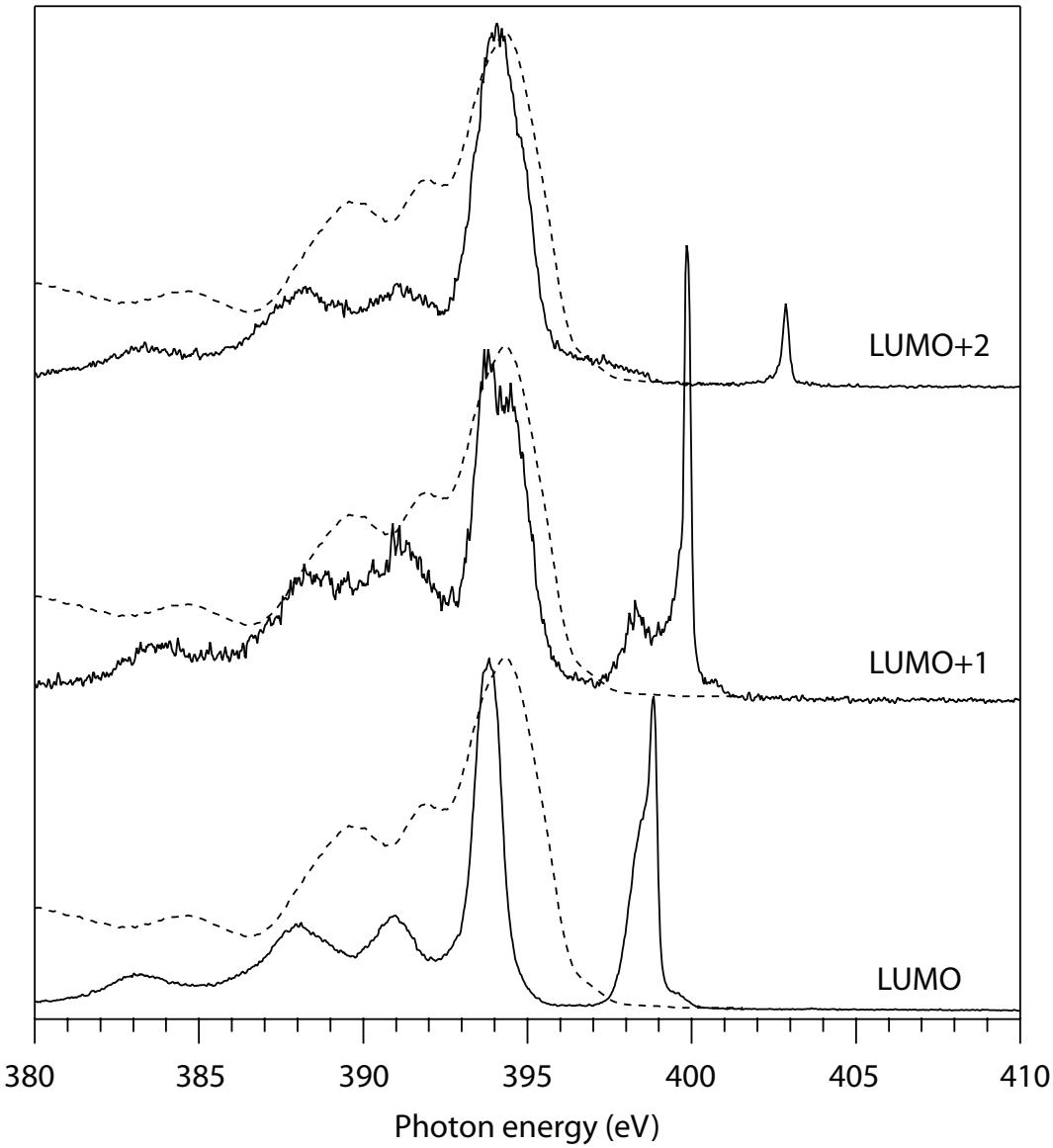

Figure 5.5: A montage of the LUMO, LUMO+1, and LUMO+2 resonances. The valence band, indicated by the dotted lines, for the bi-isonicotinic acid for the multilayer have been lined up with each of their spectra. In the top right corner the insert shown a close-up of the peak representing the HOMO resonance when the LUMO+1 state is probed. The bi-isonicotinic acid is shown in the multilayer and monolayer situations. For simplicity the hydrogen atoms have been left out.

elastic peak is observed. The strong elastic peaks especially for the LUMO and LUMO+1 resonance is due to the molecules being decoupled from the surface within the multilayer. The process is explained from the participator decay displayed in Figure 3.9. When electrons from the HOMO fills the N 1s core-hole in the radiative transition of inelastic X-ray scattering it will happen at lower photon energies compared to the elastic scattering, which are displayed by the peaks on the left hand side of the elastic peak. From Chapter 3 we know that only the states involving the nitrogen atoms of the molecule are probed, therefore these peaks represent the partial density of states of the valence band region.

Figure 5.6 shows a close up of the elastic regions obtained when the system is probed at four different excitation energies. Starting with Figure 5.6A, the excitation energy is 398.4 eV. The curve fit consist of two contributions, here marked with a line shaped pattern and with a dotted pattern. The former is the contribution from the elastic peak at 398.4 eV and the latter originates from the vibrational losses 0.23 eV away at 398.17 eV on the low photon energy side. In general, RIXS probes electronic and nuclear – i.e. vibrational – inelastic loss processes, therefore vibrational losses are to be expected RIXS measurements and in the nature of how RIXS is conducted the vibrational losses will disperse with the photon energy[26, 185–187].

Figure 5.6B shows a close up of the elastic peak for when the LUMO state at 398.8 eV is probed. The contributions from the elastic excitation and the vibrational losses are again marked with a line shaped pattern and the dotted pattern respectively. The difference in photon energy of the elastic and the vibrational contributions is 0.23 eV. The curve fit shows a clear distinct feature at 398.4 this contribution is left unmarked and will from now on be referred to a Virtual State A.

The spectrum shown in Figure 5.6C is obtained when the system is probed at an excitation energy of 399.2 eV. The contributions from the elastic peak at 399.2 eV and vibrational losses are again indicated with a line shaped and dotted patterns respectively, and with a photon energy separation of 0.23 eV.

The Virtual State A is also present at this excitation energy and noticeably it has not dispersed with the photon energy, hence it is found at a photon energy of 398.4 eV.

When the LUMO+1 state at a photon energy of 399.9 eV is probed the spectrum obtain is shown in Figure 5.6D. The elastic peak and the vibrational loss are found at 399.9 eV and at 399.67 eV respectively, and their contributions are marked with a line shaped pattern and a dotted pattern respectively. Again we find the Virtual State A at a photon energy of 398.4 eV. When a curve fit has been done a fourth component at a photon energy of 399.15 eV becomes present, this contribution will from now on be referred to a Virtual State B and is marked with an undulation pattern. The difference in photon energy between the Virtual State A and Virtual B is of 0.75 eV, which is highly comparable to the spilt of 0.8 eV photon energy found in the HOMO resonance when the LUMO+1 is probed.

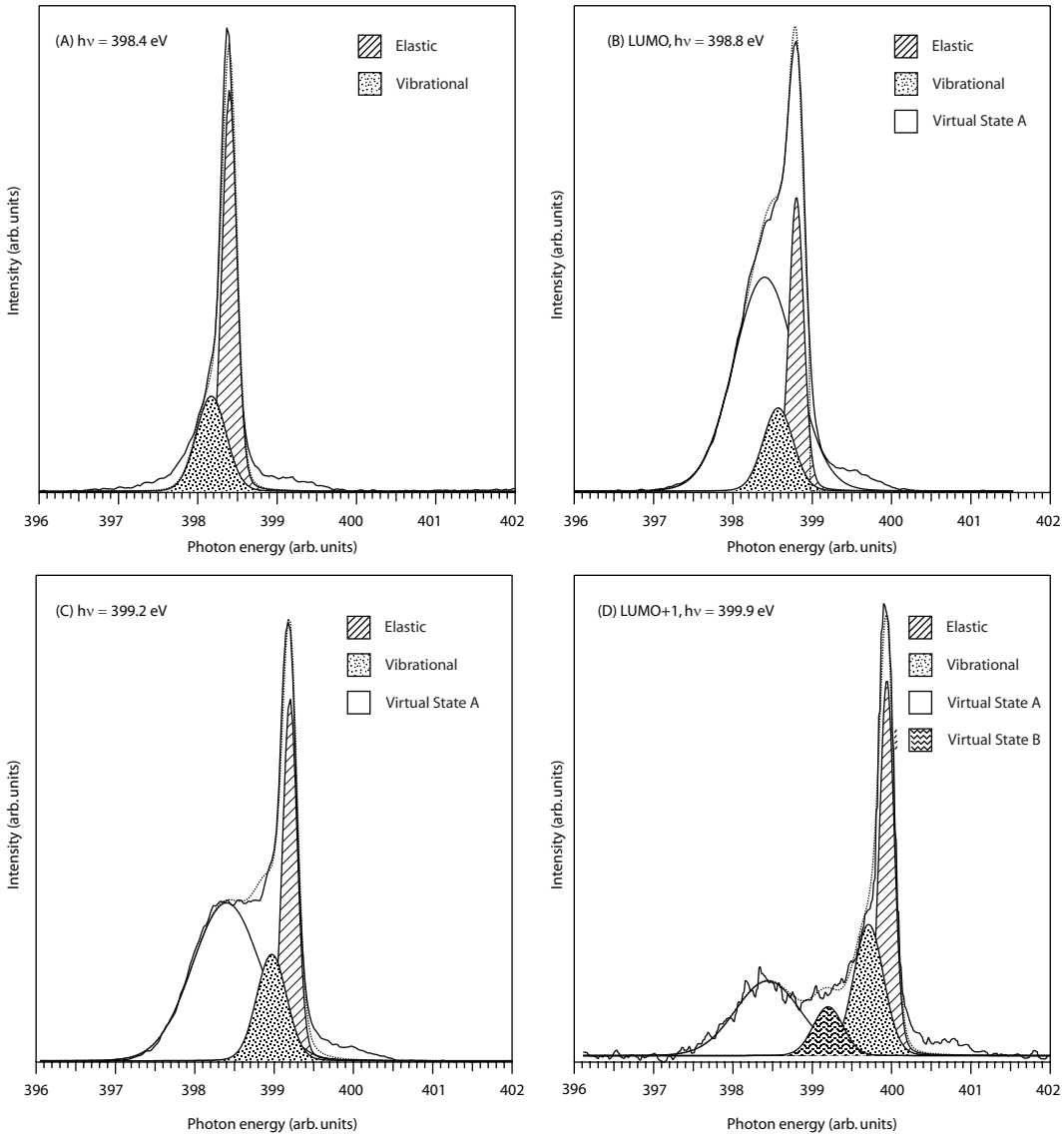

Figure 5.6: The four spectra shown a close up of each of the probed excitations energies, (A) 398.4 eV, (B) the LUMO state a 398.8 eV, (C) 399.2 eV, and the LUMO+1 state at 399.9 eV. The insert in (D) shown the spectrum obtained when the probed at a excitation energy of 405 eV, and the constant loss feature just below the LUMO excitation energy is clearly present.

The presence of the two Virtual States A and B when the LUMO+1 state is probed dictates an investigation of the LUMO+2 state in the search from similar features. In Figure 5.7 a noticeable shoulder on the main inelastic peak between a photon energy of 396 eV and 399 eV are clearly present. This shoulder probably contains the two Virtual States of A and B, but the contributions from these two state are masked in the contributions from the inelastic scat-

tering. Therefore fits for these two virtual states have not been done, due to the shape of the spectrum. If such a fit was done, other contributions from processes of non-relevance to these states might be included. The consequence of not making the fits for Virtual State A and B when the LUMO+2 resonance is probed will be discussed later on.

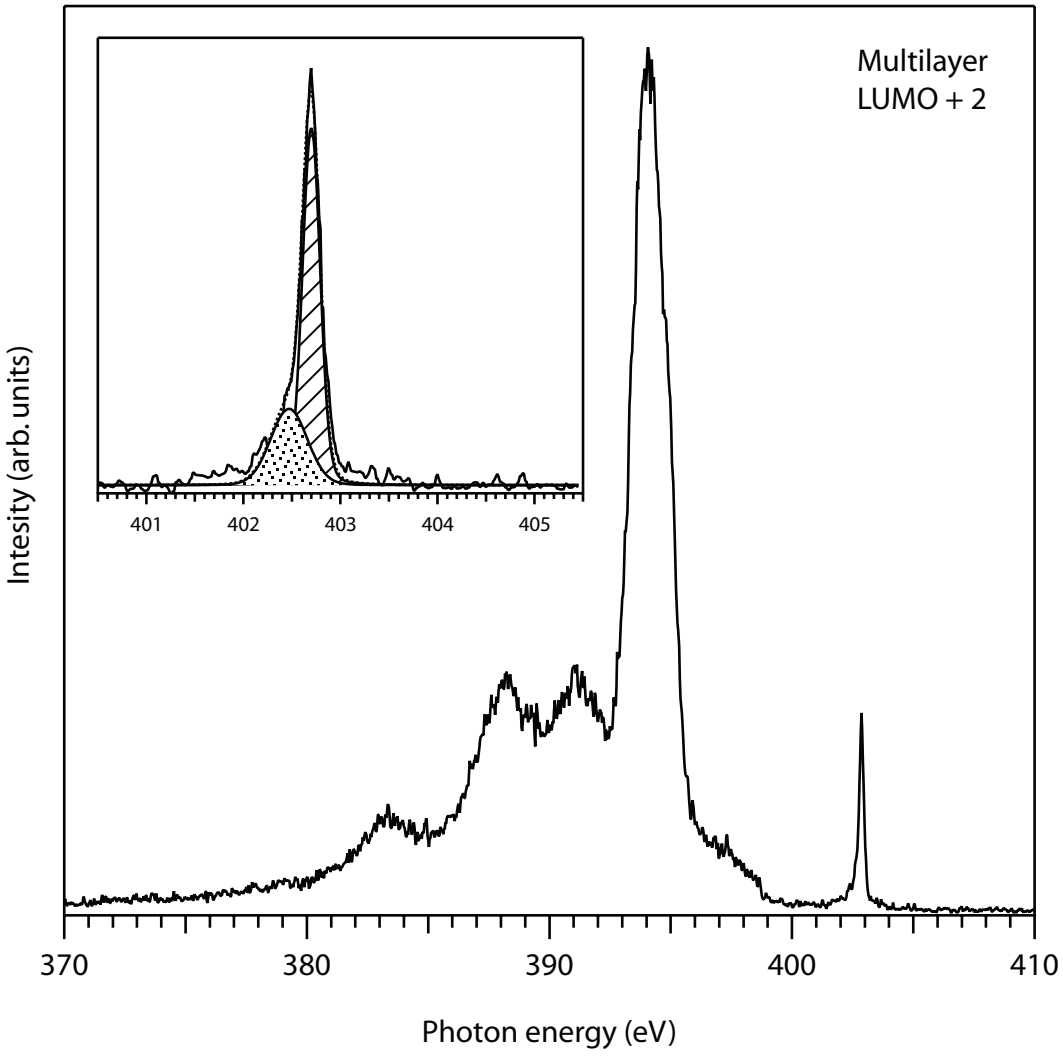

Figure 5.7: Resonant inelastic X-ray scattering for the multilayer at the LUMO+2 resonance at 402.7 eV in the rutile $TiO_2(110)$ substrate. The insert shows at close-up of the LUMO+2 resonance.

Discussion of the two Virtual States A and B for the multilayer

From Figure 5.6 it becomes clear that the Virtual State at 398.4 eV is not dispersing with photon energy. Since it does not disperse with excitation energy it can not be an elastic or vibrational contribution.[26] At a photon energy of 398.4 eV it is located 0.5 eV below the LUMO resonance, which is significantly above the highest occupied molecular orbital, therefore this virtual state must be a transition, implying that it describes a state that becomes occupied when the X-ray emission takes place and decays within the lifetime of the core-hole. With the close position to the LUMO resonance it is highly likely to originate from charge transfer from the higher lying states – e.g. LUMO, LUMO+1 and LUMO+2 – within the molecule. These states only exist in the core-excited state and are therefore not visible within the technique of XAS, hence RIXS provides a more complete picture of processes. The somewhat simple two-step approximation of the photon-in-photon-out process of RIXS, is illustrated by Figure 5.8(I), the incoming photon excites the electron to a higher lying state, in this case the LUMO+1 state, and decays into the final state, by emitting a photon. Within this description electrons can reach the final state by several scattering processes involving an intermediate state, giving rise to vibrational losses, which are present in this experiment. [26]

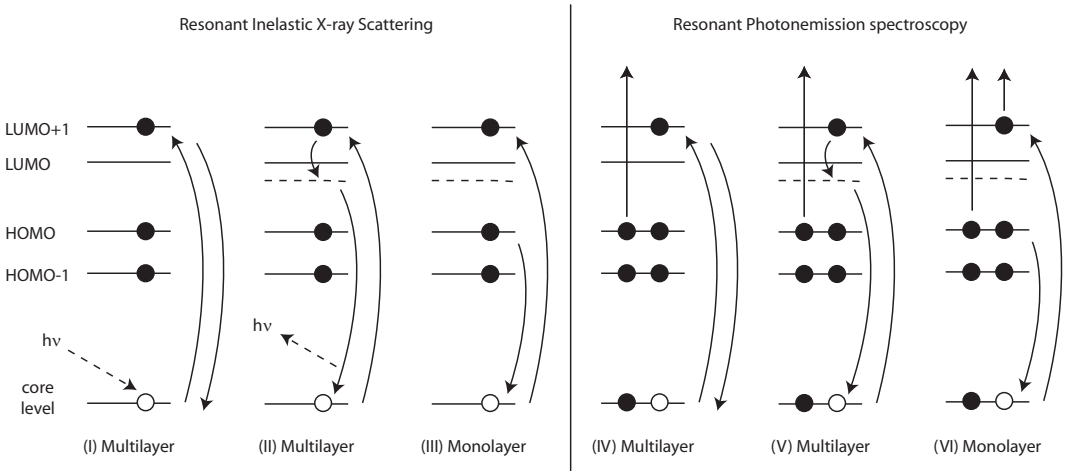

Figure 5.8: A schematic representation of the different processes within RIXS and RPES. (I) the classical photon-in-photon-out model. In (II) a states just below the LUMO resonance, illustrated by the dotted line, is introduced and is representing potential charge transfer within the excited molecule. The situation in (IV) describes the participator decay when RPES is taking place. Introducing charge transfer (V) with in the molecule, will not change the participator signal when RPES is measured.

In the situation of charge transfer within the molecule the situation is described by Figure 5.8(II). The initially incoming photon excited a core electron and thereby populating the higher laying states. When the X-ray emission is taking place, electrons from the populated excitation states are charge transferring into the Virtual State A just below the LUMO, which then decays into the the final state by emitting a photon. Regardless of the excitation energy, the charge transfer within the molecule ensures a constant transition between either the LUMO, LUMO+1 and the LUMO+2 and the Virtual State A and B and is only present in the core-excited state. The presence of Virtual State A and B are either a confirmation of charge transfer within the molecule due to the presence of a core-hole or they might be the result of ultra fast relaxation of the molecule.

Monolayer coverage and presentation of results

In Figure 5.9 the resonant inelastic X-ray scattering spectra for the different photon energies are shown ranging from the LUMO resonance, LUMO+1,

LUMO+2 and up to an excitation energy of 405 eV high above the LUMO+2 resonance. Immediately it becomes clear that the contributions from the inelastic scattering processes change dramatically when increasing the excitation energy to a level above the LUMO resonance. For the LUMO+1, LUMO+2 and for the spectra of 405 eV photon energy the inelastic contribution merges into one single broad peak. In the case of the LUMO resonance, the different contribution from the inelastic scattering processes are still able to be separated and the main peak which is centered around 393.8 eV, represents the highest occupied molecular orbital for the bi-isonicotinic acid molecule on the rutile TiO_2(110) surface for the monolayer. It is noticeable that the location of the HOMO has not shifted between the multilayer and the monolayer when the LUMO state is probed for both cases.

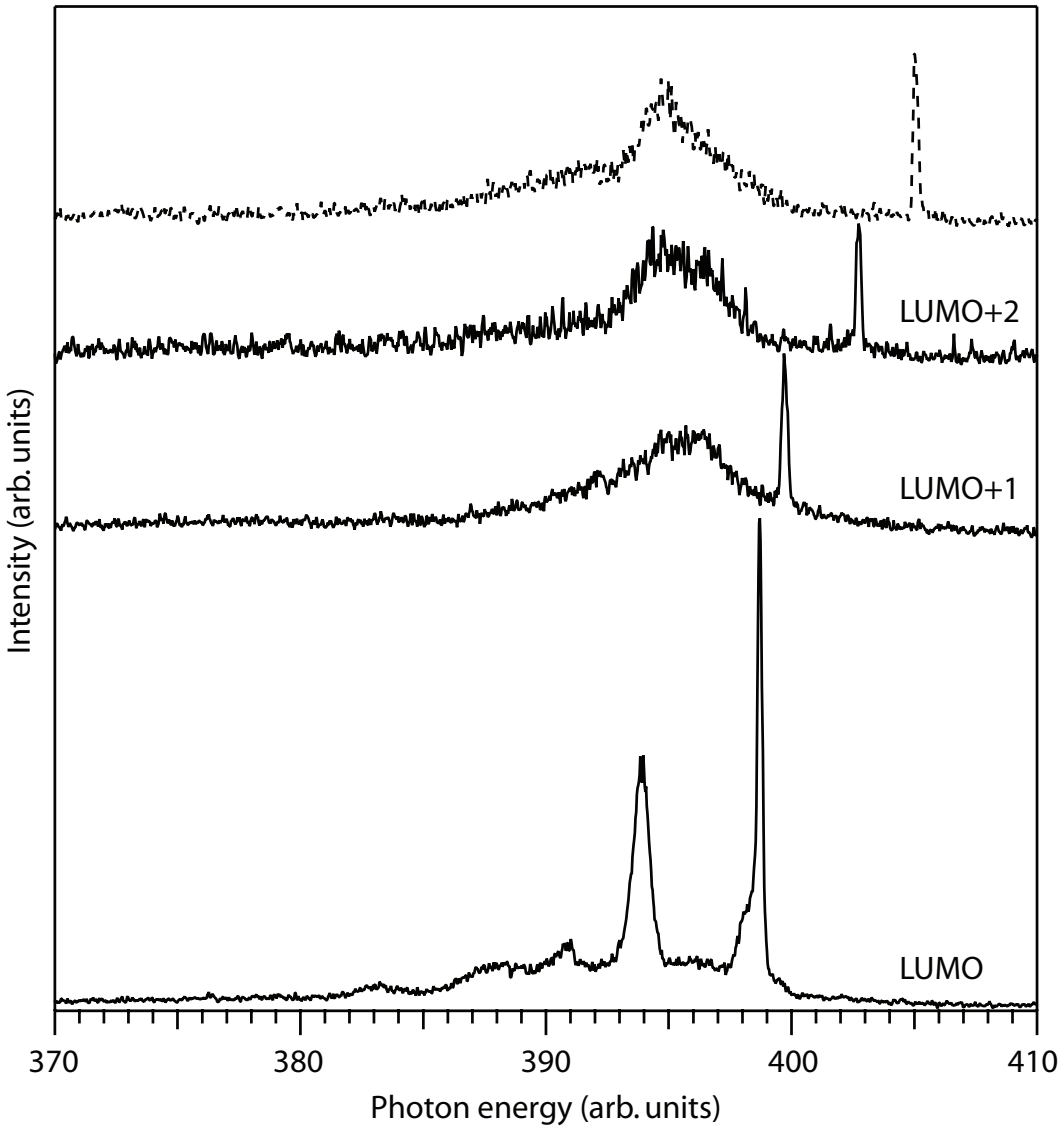

Figure 5.9: A montage of each of the probed excitation energies. The top dotted line is the off-resonance at a photon energy of 405 eV. The insert is a close-up of the peak representing the HOMO state the LUMO+2 resonance is probed.

The main broad peak obtained when the LUMO+1 resonance is probed is centered around a photon energy of 395.7 eV, whereas moving to the LUMO+2 state, the main broad peak in this scenario seems to be spilt into two peaks. Those two peaks are found at photon energies of 394.7 eV and 396.5 eV respectively.

When the LUMO state is probed for the monolayer of the bi-isonicotinic acid molecule on the rutile $TiO_2(110)$ surface, the elastic peak consists of

contributions from the elastic scattering processes, the vibrational losses and also a contribution from the Virtual State A at a photon energy of 398.4 eV.

The spectra for the LUMO+1 state, LUMO+2 state and the above-resonance state at a photon energy of 405 eV, all show a sharp peak at their respective excitation energies, which represent their elastic peaks. In the work of Britton *et al.*[25] such sharp peaks where not reported, since required resolution was not achievable at the time.

In Figure 5.10 a close up for each of the LUMO, LUMO+1 and the LUMO+2 resonances, lined up together with their multilayer and monolayer coverages are shown.

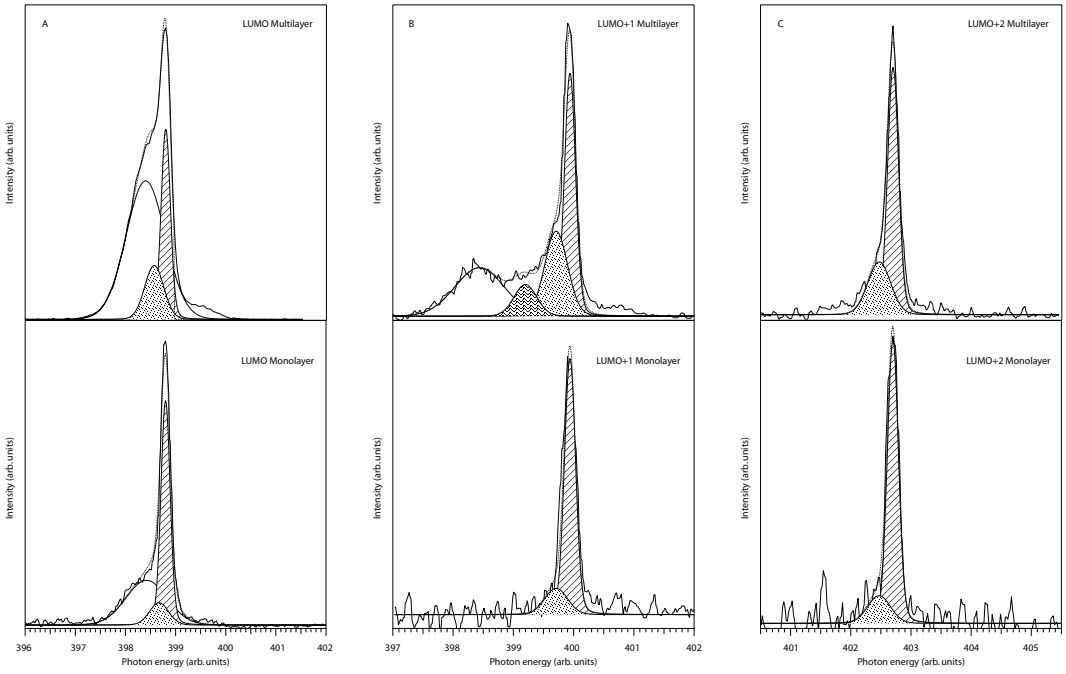

Figure 5.10: RIXS spectra showing the LUMO, LUMO+1 and LUMO+2 resonances for both the multilayer and monolayer.

In Figure 5.10B where the multilayer and monolayer for the LUMO+1 resonance are shown we note that Virtual State A and B are not present in the monolayer situation. The lack of the two virtual states is an indication of charge transfer out of the LUMO+1, and will be discussed in the next section.

Estimating charge transfer by the core-hole clock implementation

For comparison our results and the previously published results of the same system[25] are shown in Figure 5.11A and Figure 5.11B. In Figure 5.11A our measurements are displayed from when the LUMO resonance for the multilayer of the bi-isonicotinic acid on the rutile $TiO_2(110)$ surface is probed. The insert in Figure 5.11A show a close up of the elastic peak, where the contribution of the elastic scattering (line shape pattern), the vibrational loss (dotted pattern) and the virtual state A (not marked) are labelled. Figure 5.11B shows the results from the work of Britton *et al.* where the elastic peak is indicated.

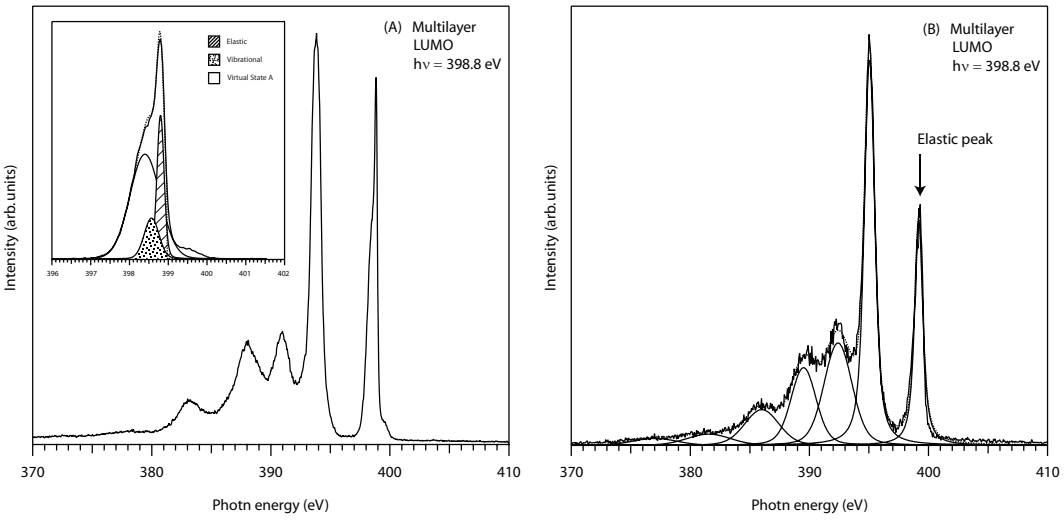

Figure 5.11: The LUMO RIXS spectra for the multilayer of bi-isonicotinic acid on the rutile $TiO_2(110)$ surface. The left hand side marked (A) shows our data obtain at SEXTANS beamline, SOLEIL, France. On the right hand side marked (B) shows the LUMO RIXS measurement publish by Britton *et al.* of the bi-isonicotinic acid on the rutile $TiO_2(110)$ surface.

When the different contributions in our cases are evaluated we find an area of the elastic contribution to be 0.04, the vibrational loss to contribute with an area of 0.02 and the Virtual State A have an area of 0.1. The full-width-half-maximum (FWHM) of our elastic contribution is $\mathrm{FWHM}^{\mathrm{A}}_{\mathrm{MultiLUMO}} = 0.2$ eV. Making the same evaluation of the elastic in Figure 5.11B we find an area

of 0.167, which Britton *et al.* also reports, $\mathrm{FWHM}^{\mathrm{B}}_{\mathrm{MultiLUMO}} = 0.6$. We note that adding the areas of the vibrational loss and the Virtual State A to our elastic contribution, we obtain the same area as of Britton *et al.*[25] It is clear from Figure 5.11A and Figure 5.11B that they did not have the resolution as of the SEXTANS beamline, this is further stressed by the factor of 3 in difference between the $\mathrm{FWHM}^{\mathrm{A}}_{\mathrm{MultiLUMO}}$ and $\mathrm{FWHM}^{\mathrm{B}}_{\mathrm{MultiLUMO}}$ since the $\mathrm{FWHM}^{\mathrm{B}}_{\mathrm{MultiLUMO}}$ consists of the contribution from the vibrational loss and the Virtual State A, which Britton *et al.*[25] could not extract in their measurements.

Probing the system of at the LUMO+1 resonance at a photon energy of 399.9 eV the spectrum obtained is shown in Figure 5.12A and we note a much higher intensity for the elastic peak compared to the peak representing the HOMO resonance, again a result of the high performance SEXTANS beamline. The insert in Figure 5.12A shows a close up of the elastic peak, the contributions from the elastic scattering process (line shape pattern), the vibrational loss (dotted pattern), and the two virtual states A (blank) and B (wavy pattern), are labelled. The areas of each of these are found to be 0.046 for the elastic contribution, 0.025 for the vibrational contribution, and 0.036 and 0.014 for the contributions of virtual state A and B respectively. Given a total area of 0.121. Extracting the same kind of information form Figure 5.12B we find that the area of the fitted elastic peak is 0.127, in good correspondence to Britton *et al.*.[25] The difference in the FWHM of the elastic peaks in the two data are still a factor 3. We note that from Figure 5.12B a spilt is present in the peak representing the HOMO resonance. This split is 3 eV in photon energy and the ratio between the two Gaussian fits is found to be 80%

When the LUMO resonance at a photon energy of 398.8 eV for the monolayer of the bi-isonicotinic acid on the rutile TiO_2(110) surface is probed the spectrum shown in Figure 5.13A is obtained. The insert shows a close up of the elastic peak, where the contributions from the elastic scattering processes (line shape pattern), the vibrational losses (dotted pattern) and the virtual state A (unmarked) fitted. Similarly as in that of the treatment of the multilayer, we extract the areas of the three contributions and find the to be 0.1, 0.02 and 0.04

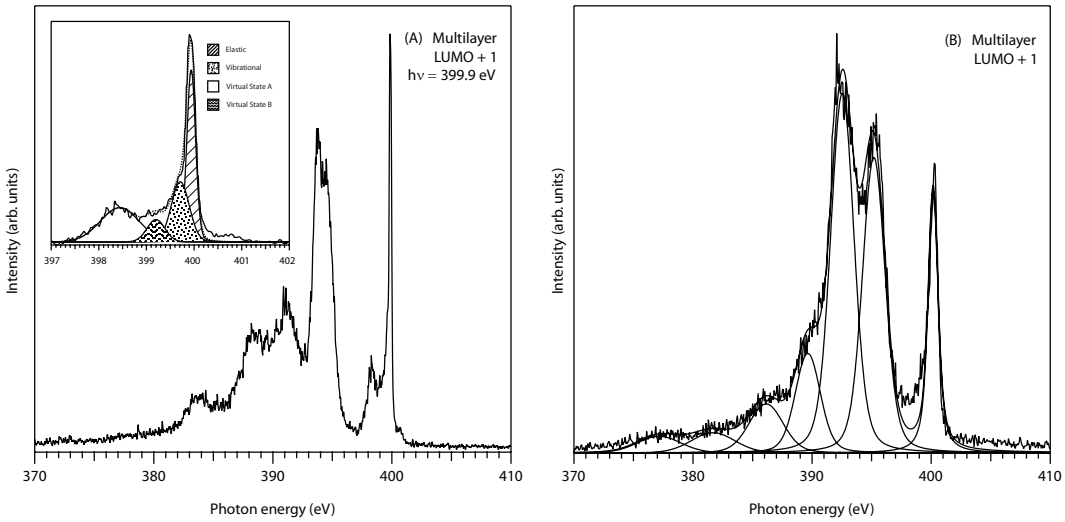

Figure 5.12: The LUMO+1 RIXS spectra for the multilayer of bi-isonicotinic acid on the rutile $TiO_2(110)$ surface. The left hand side marked (A) shows our data obtain at SEXTANS beamline, SOLEIL, France. On the right hand side marked (B) shows the LUMO+1 RIXS measurement publish by Britton *et al.* of the bi-isonicotinic acid on the rutile $TiO_2(110)$ surface.

respectively, given a total sum of 0.16, and FWHM for the elastic contribution is found to be $\mathrm{FWHM}^{\mathrm{A}}_{\mathrm{MonoLUMO}}$ 0.198. Noticeable is the strong intensity of the elastic peak compared to the peak belonging to the HOMO resonance. In Figure 5.13B the spectrum obtained in the studies of Britton*et al.* is shown. We immediately see that here the elastic peak is reduced to a shoulder on the broad peak displaying the inelastic scattering processes in their measurements. Extracting the information from Figure 5.13B the $\mathrm{FWHM}^{\mathrm{B}}_{\mathrm{MonoLUMO}}$ is found to be 0.6 and we find the same area as Britton *et al.* of the elastic peak to 0.136.

Moving up to a higher excitation energy as in that of 399.9 eV photon energy the LUMO+1 resonance will be probed. The spectrum here obtained is shown in Figure 5.14A. We note, as in the previous section, that all the processes from the inelastic scattering have merged into a single broad peak and the LUMO+1 resonance shows itself with a sharp peak at 399.9 eV. The inset in Figure 5.14A shows a close up of the elastic peak, where the contribution from the elastic scattering processes are marked with a line shape pattern and the vibrational losses with a dotted pattern. The areas of these two contributions are found to be 0.034 and 0.007 respectively, given a total sum

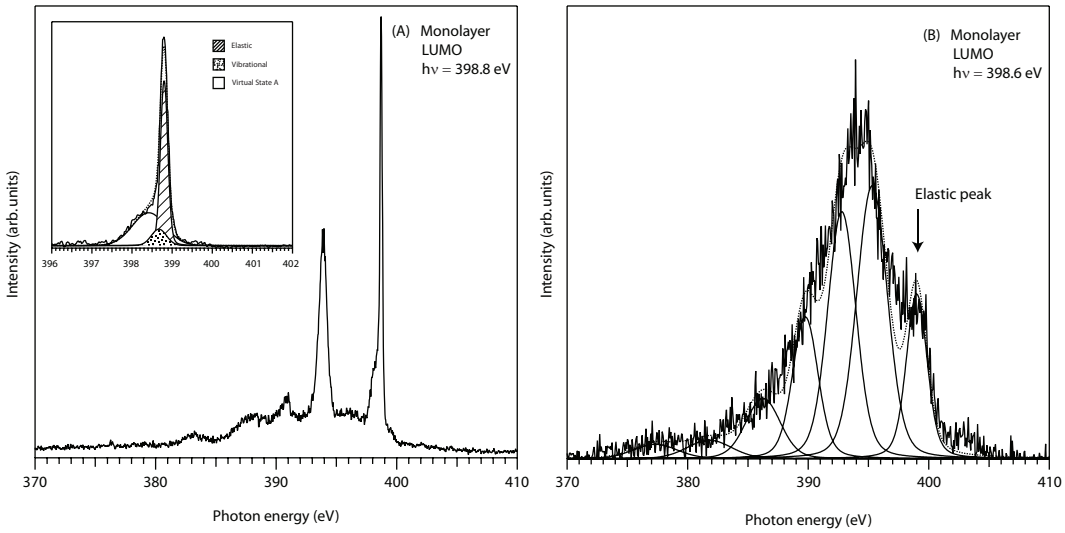

Figure 5.13: The LUMO+1 RIXS spectra for the multilayer of bi-isonicotinic acid on the rutile $TiO_2(110)$ surface. The left hand side marked (A) shows our data obtain at SEXTANS beamline, SOLEIL, France. On the right hand side marked (B) shows the LUMO+1 RIXS measurement publish by Britton *et al.* of the bi-isonicotinic acid on the rutile $TiO_2(110)$ surface.

of 0.041. The $\mathrm{FWHM}^{\mathrm{A}}_{\mathrm{MonoLUMO1}}$ is in this case found to be 0.2. On the left hand side Figure 5.14B shows the spectrum obtain by Britton *et al.* when they probe the system at the LUMO+1 for the monolayer of bi-isonicotinic acid on the rutile $TiO_2(110)$ surface. Similar to their case of the LUMO resonance, their elastic peak is heavily reduced to a low shoulder on their main broad peak of inelastic contribution. They report the areas of the elastic peak to be 0.033, and they have a $\mathrm{FWHM}^{\mathrm{B}}_{\mathrm{MonoLUMO1}}$ of 0.6.

The LUMO+1 resonance is overlapping with the conduction band edge of the rutile $TiO_2(110)$ and should therefore provide ultra-fast charge transfer into the substrate on the timescale of the core-hole lifetime preventing the originally excited electron to contribute to the participator decay. Accompanied by the core-hole clock implementation [156] the fitted elastic peaks allow thorough investigation of the charge transfer dynamics. The main fitted elastic peaks within inserts Figure 5.11A, 5.12A, 5.13A, and Figure 5.14A are representations of the fraction of the total number of photons arising from the participator decay. The LUMO state can be regarded as a benchmark since

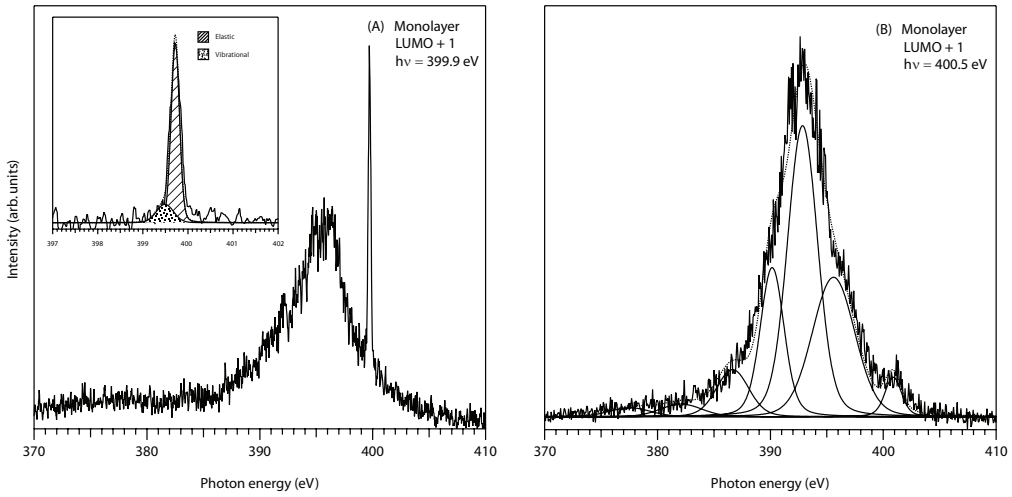

Figure 5.14: The LUMO+1 RIXS spectra for the multilayer of bi-isonicotinic acid on the rutile $TiO_2(110)$ surface. The left hand side marked (A) shows our data obtain at SEXTANS beamline, SOLEIL, France. On the right hand side marked (B) shows the LUMO+1 RIXS measurement publish by Britton *et al.* of the bi-isonicotinic acid on the rutile $TiO_2(110)$ surface.

no charge transfer to the substrate is allowed from this state. In the multilayer the molecules are decoupled from the substrate and no charge transfer is expected. By the absence of charge transfer the amount of participator decay from the LUMO+1 state compared to the LUMO state can be determined. A clear indication of charge transfer, in the lifetime of the core-hole, τ_{CH} – reported to be 6 fs [188] for N $1s$ – to the substrate will be a reduction of the ratio between the elastic peaks when moving to the monolayer situation.

Estimating the charge transfer out of the LUMO+1 state by the core-hole clock implementation

In Chapter 2 we found that the excited electron transfer time, τ_{CT}, in terms of the intensities of the participator channel for the isolated molecule I_{iso} in the multilayer and for the system of the coupled monolayer I_{coup} can be obtained by rearranging the equations of the relationship between the fractional spectral intensity of the participator channel to the rates of charge transfer into the conduction band and the core-hole decay displayed by Brühwiler *et al* [156]. This is shown in equation 5.1

$$\tau_{\mathrm{CT}} = \tau_{\mathrm{CH}} \frac{I_{\mathrm{coup}}}{I_{\mathrm{iso}} - I_{\mathrm{coup}}} \tag{5.1}$$

The term I_{coup} is the relative intensity of the LUMO+1 in the monolyer of the elastic peak, normalized to the intensity of the elastic peak of the LUMO where charge transfer is forbidden. The term I_{iso} is derived from the intensity of the elastic peak of the LUMO+1 in the multilayer and normalized to the intensity of the elastic LUMO peak for the same coverage ending up with equation 5.2

$$\tau_{\mathrm{CT}} = \tau_{\mathrm{CH}} \frac{\frac{I^{\mathrm{Mono}}_{\mathrm{LUMO+1}}}{I^{\mathrm{Mono}}_{\mathrm{LUMO}}}}{\frac{I^{\mathrm{Multi}}_{\mathrm{LUMO+1}}}{I^{\mathrm{Multi}}_{\mathrm{LUMO}}} - \frac{I^{\mathrm{Mono}}_{\mathrm{LUMO+1}}}{I^{\mathrm{Mono}}_{\mathrm{LUMO}}}} \tag{5.2}$$

The total sum of all the fitted contributions to the elastic peak of LUMO in the multilayer is 0.159 and for the LUMO+1 it is 0.121, giving a fraction of 0.76 for the LUMO+1 of the observed LUMO in the absence of charge transfer. All the peaks fitted to the LUMO state for the monolayer have a combined intensity of 0.161. When the areas of the peaks fitted to the LUMO+1 are added together we find a total sum of 0.041. This gives a corresponding fraction of 0.25. This reduction in the number of participator events is due to charge transfer out of the core-excited LUMO+1 state. Using equation 5.2 we obtain a charge transfer time, τ_{CT}, of 2.9 $\pm$ 0.3 fs, which is in good correspondence to the 2.8 fs $\pm$ 1.5 as reported from Britton *et al.*[25] Previous studies [18] where the technique of resonant photoemission spectroscopy has been employed to measure the charge transfer for the bi-isonicotinic acid, they report an upper limit of 3 fs for the electron injection into to the substrate, which our results are in good agreement with.

Estimating the charge transfer out of the LUMO+2 state by the core-hole clock implementation

In Figure 5.15(A) and Figure 5.15(B) the RIXS measurement for the LUMO+2 for both the multilayer and the monolayer is shown. The insert in both figures shows a close up of the elastic peaks. The contribution from the elastic scat-

tering are labelled with a line shape pattern and the vibrational losses with a dotted pattern. In the case of the multilayer in Figure 5.15(A) we note that between a photon energy of 396 eV and 399 eV a noticeable shoulder to the main inelastic peak is present.

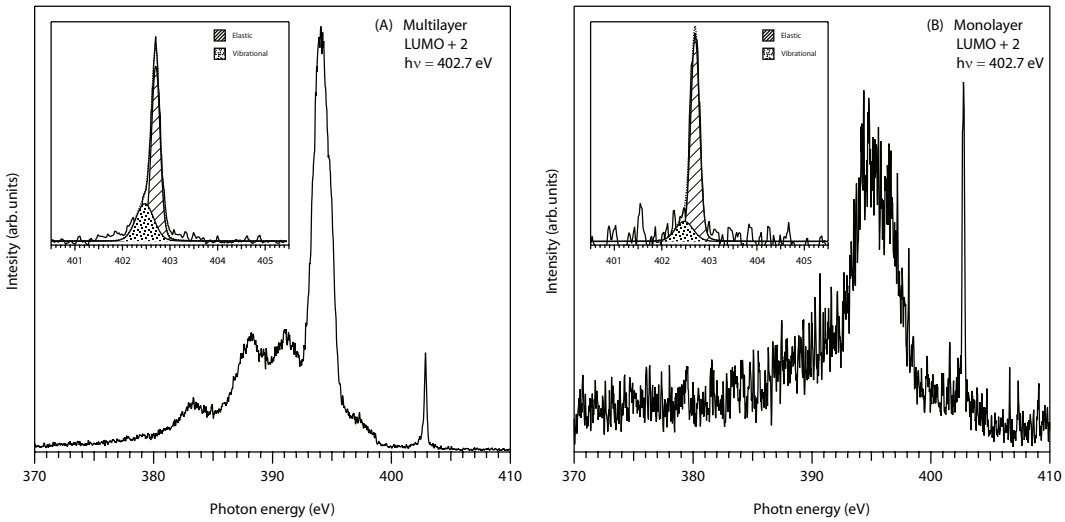

Figure 5.15: The LUMO+2 RIXS spectra for the multilayer of bi-isonicotinic acid on the rutile $TiO_2(110)$ surface. The left hand side marked (A) shows our data obtain at SEXTANS beamline, SOLEIL, France. On the right hand side marked (B) shows the LUMO+2 RIXS measurement publish by Britton *et al.*[25] of the bi-isonicotinic acid on the rutile $TiO_2(110)$ surface.

As discussed in the previous section, virtual states A and B are most likely present within this shoulder, but it is not possible to resolve them since they are covered by the contributions from the inelastic scattering processes. From the discussion for the LUMO+1 states we know that the virtual states A and B clearly participate in the charge transfer process. In the case of the LUMO+2 we can not resolve these to virtual states and therefore estimate the charge transfer out of the LUMO+2 state will not make any sense to perform.

From the work of Schnadt *et al.*[18] we know a charge transfer time in the low femto-second regime should be expected for the LUMO+2. When that charge transfer was measured, it was done by resonant photoemission. When resonant photoemission is applied, it will measure the emitted photo-electron from the highest occupied molecular orbital as shown in Figure 5.8(IV)

and (V), which does not carry any information of charge transfer within the molecule. When resonant inelastic X-ray scattering is applied to the system, the photon emitted when the electron decays from the constant loss state to the final state is measured. Since the Vibrational States A and B are not detectable when the LUMO+2 state is been probed with the technique of RIXS (see Figure 5.7) these highly important contributions to the charge transfer between the molecule and the substrate can not be included and therefore a non-real charge transfer time is obtained.

5.4 Conclusion

The reproducible result obtained for a charge transfer time of 2.9 fs out of the LUMO+1 state to the substrate supports the core-hole clock implementation to the technique of resonant inelastic X-ray scattering. Applying the clock-hole clock implementation to RIXS is highly encouraging, but when higher laying states where other contributions form interference can govern the measurements, careful consideration to how and if the experiment is carried out needs to be done. In our case were the noise and processes from the inelastic scattering where overlapping the contribution from the virtual states of A and B it was impossible to probe the charge transfer qualitatively. When evaluating higher laying states other factors as of charge transfer within the molecule or ultra fast relaxation of the molecule become dominant. A path to follow in the pursuit of the answer to if any ultra fast relaxation or charge transfer within the molecule occurs will be to employ the molecule of isonicotinic acid depicted in Figure 1.3(C). As mentioned in the Chapter 1 is the building blocks of the bi-isonicotinic acid molecule. The split in the HOMO peak when the LUMO+1 resonance is probed (see Figure 5.5) might be the result of introducing a core-hole excitation on one of the rings within the bi-isonicotinic acid and leading to charge transfer between rings. The split of the HOMO peak possibly originates from this charge transfer within the molecule. Therefore we suggest to carry out similar measurements on the somewhat simpler molecule

of isonicotinic to shed light upon this issue.

Chapter 6

RPES and XAS studies of zinc porphyrin nanoring on TiO_2(110) and Au(111) surfaces

6.1 Introduction

The production of nano-scale electronic devices may potentially be realized by utilising electronic components which have been produced via chemical synthesis. Many systems have been studied where the electronic components of a circuit are pre-designed "molecular components" with desired opto/electronic properties such as light emitting diodes[189], photo-voltaic diodes[48, 190–193], and field-effect transistors[45, 194–196]. In order to join these components together to produce a truly nano-electronic circuit, molecular wires will be required. Major candidates for molecular wires include materials like carbon nanotubes[197, 198] and π-conjugated organic polymers.[199–201] As many other organic materials, interfacial properties are likely to play an important role in their applications in molecular electronics.[202] One of the great hurdles of studies these effects is the difficulty of preparing suitable monolayer, since these polymers cannot by sublimed. Here we employ the technique of ultrahigh vacuum electrospray deposition preparing monolayer coverages of the c-**P**12 porphyrin nanorings shown in Figure 6.1.

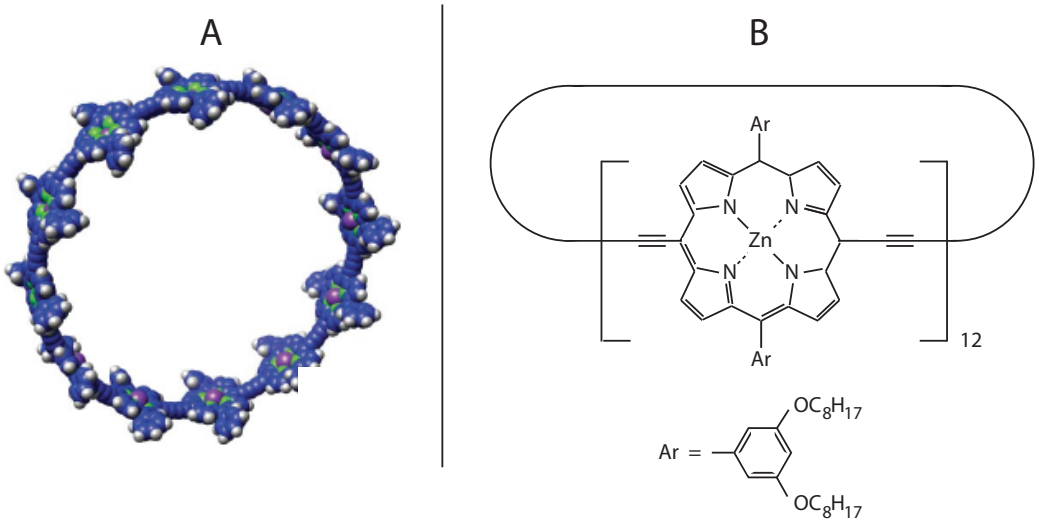

Figure 6.1: Ball-and-stick representation of the c-**P**12 molecule. (B) The chemical structure of c-**P**12.

6.2 Method

Experiments were carried out at beamline I311 of the Swedish synchrotron facility MAXlab in Lund. The beamline has a photon energy range of 43-1500 eV and is equipped with a Scienta SES200 hemispherical electron analyzer.[151] The radiation has a high degree of elliptical polarization and may be considered as linearly polarized for the purposes of this study. The pressure, in the analysis chamber, was in the mid 10^{-11} mbar range when measurements were carried out.

Two different substrates were used. The first substrate was a rutile TiO_2(110) single crystal of dimensions (10 × 10 × 1) mm, acquired from PI-KEM Ldt, UK. The crystal was cleaned along the lines of Barth *et al.*[95] by cycles of sputtering using 1 kV Ar^+ ions and then annealing at 900 K using a pBN heater mounted behind the crystal. Surface contamination was checked by ensuring that the C 1*s* and K 2*p* peak were below the detection limits of our measurements. The monochromator exit slits of the beamline were set to give a resolution of 100 meV for photons of 640 eV energy. X-ray absorption spec-

tra were measured using a partial yield detector with a 100 V retardation and the photon energy scale was calibrated from the separation between the Ti $2p$ peaks measured with 1^{st} and 2^{nd} order radiation.

The second substrate used was a Au(111) single crystal from Metal Crystals and Oxides Ltd. having a diameter of 10 mm and 2.5 mm thick. It was mounted on a loop of 0.5 mm diameter tungsten wire, that passed tightly through the body of the crystal, ensuring a good electrical and thermal contact. A thermocouple was attached within the body of the crystal in order to accurately monitor the temperature. The crystal was cleaned along the lines of Barth *et al.*[95] by cycles of sputtering using 1 kV Ar^+ ions and then annealing at 900 K by passing a current through the tungsten wire mount. Surface contamination was assessed by ensuring that the C $1s$ core level photoemission peak was below the detection limits of our measurements.

When the measurements for on the gold surface were conducted the monochromator exit slits of the beamline were set to give a resolution $\approx$ 50 meV for photons of energy hν = 340 eV. The photon energy was calibrated from the separation between the Au $4f$ peaks measured with 1^{st} and 2^{nd} order radiation. For measuring X-ray absorption and resonant photoemission spectra, a taper was applied to the undulator to reduce the intensity variation of the radiation as the photon energy was scanned. For XAS and RPES measurements, the analyzer pass energy and entrance slits were set to give a resolution of $\approx$ 100 meV with respect to binding energy. The analyzer was also set to record spectra in fixed mode for these measurements to give the best compromise between energy resolution and the number of counts required for two-dimensional RPES spectra. The final RPES spectra were a summation of a series of short measurements in order to take account of any change in coverage. For core level spectra, the analyzer was set to record in swept mode with an electron resolution of $\approx$ 100 meV.

The porphyrin nanorings were deposited using a commercial *in-situ* UHV electrospray deposition source from Molecularspray, UK. The molecules were deposited from a solution of 1 mg in a 10 mL of a 3:1 toluene-methanol mixture.

The liquid is delivered under a sufficient pressure to a hollow stainless-steel emitter held at 1.9 - 2.5 kV. At this potential the liquid becomes ionized and a plume emerges consisting of multiply charged droplets. The plume enters a series of differentially pumped molecular beam skimmers via a grounded entrance capillary, 5 cm long and with 0.25 mm internal diameter. During deposition the solvent molecule are gradually lost through evaporation and a cascade of Coulomb fission events. This deposition technique is described in greater detail elsewhere[23] and has been successfully used to deposit a range of complex organometallic molecules previously.[56, 74, 127, 129] A UHV gate valve separates the electrospray system from the preparation chamber. With the valve closed the base pressure of the preparation chamber was in the low 10^{-10} mbar range. With the gate valve open, but the emitter voltage off and thus no electrospray process occurring, the pressure in the preparation chamber was in the low 10^{-8} mbar range. When the electrospray process was carried out the pressure in the preparation chamber rose to the mid 10^{-7} mbar range, the additional pressure being due to residual solvent molecules in the molecular beam. The deposition spot from the electrospray source is circular shaped with a gaussian profile.

6.3 The c-P12 molecule on rutile TiO_2(110)

Results of the c-P12 molecule on the rutile TiO_2(110)

The main purpose of the this experiment was to investigate potential charge transfer between the c-**P**12 molecule and the surface. XPS spectra where recorded to in order to identify if any molecules have been deposited. These non-calibrated datasets are shown in Figure 6.2

The different datasets displayed in Figure 6.2 clearly show that molecules have been deposited on the surface. Figure 6.2(A) and Figure 6.2(B) which show the valence band photoemission spectra a multilayer and monolayer coverage, were used to identify if the following measurements where conducted for

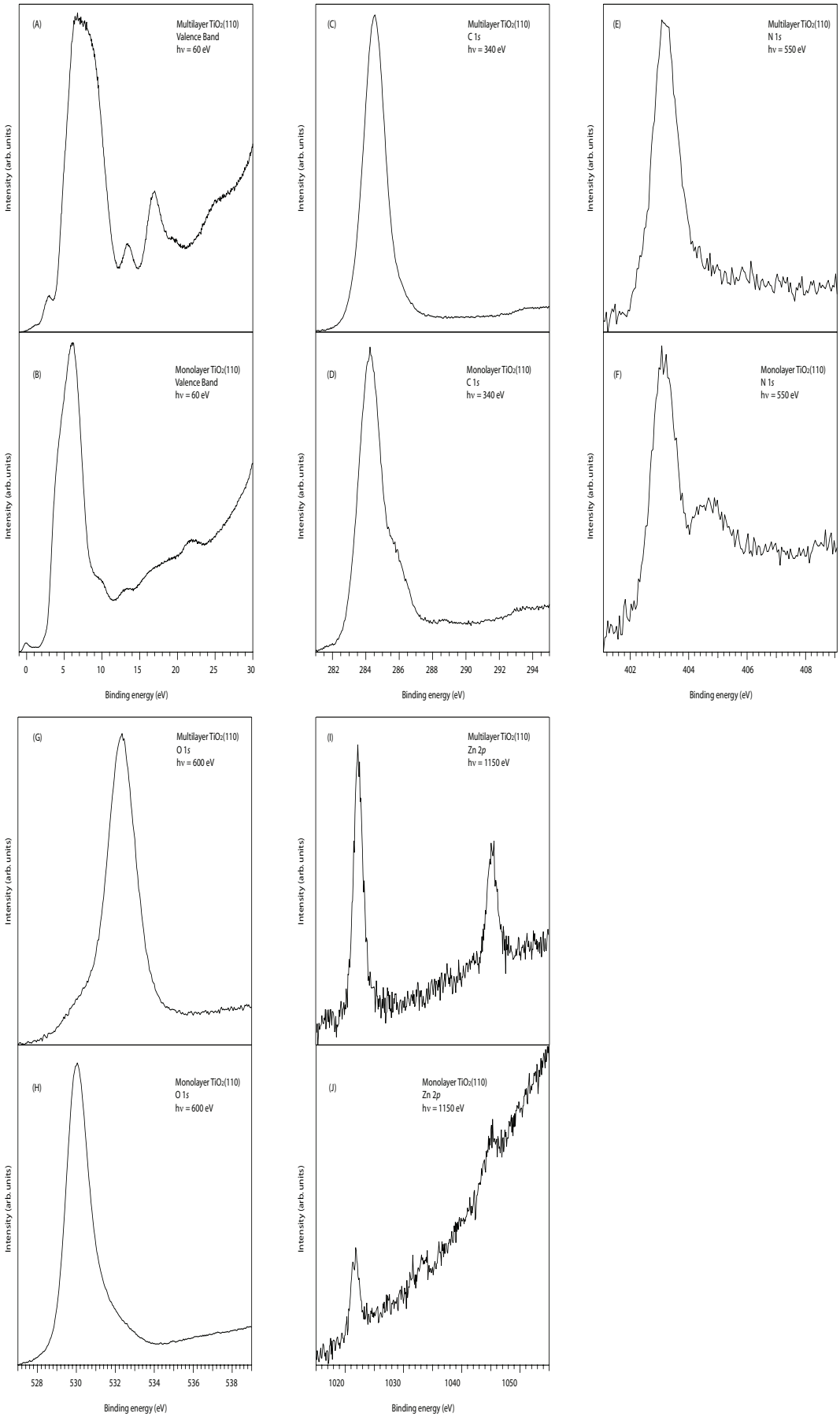

Figure 6.2: XPS data for the c-**P**12 molecule on the rutile TiO_2(110) surface. Each of the figures are labelled and displaying which kind of spectra they are, and at which excitation energy they where recorded.

either monolayer or multilayer. The small peak a 3 eV in Figure 6.2(A) is the contribution from the HOMO of the molecule, where the other peaks arises from the different molecular orbitals of the molecule. In the Figure 6.2(B) a small peak is located at a photon energy of 0 eV, which originates from defects introduction to the substrate during the cleaning process of the crystal. In the same figure between 8 eV and 10 eV a shoulder to the main peak is found, which are the valence band of the rutile TiO_2(110) substrate. The shoulder is a contribution from the molecule and was used as an indication if any molecules have been deposited on the surface.

The C 1*s* spectra recorded at an excitation energy of 340 eV for the multilayer and monolayer are shown in Figure 6.2(C) and (D). The multilayer spectrum (Figure 6.2(C)) shows a clear carbon peak originating from the vast amount of carbon within each molecule. In the Figure 6.2(D) the C 1*s* spectrum for the monolayer is displayed. The shoulder on the main carbon peak probably originates from residual solvents from the deposition.

The XPS data for the N 1*s* are shown in Figure 6.2(E) and Figure 6.2(F) for the multilayer and monolayer, respectively. The main peak in both spectra originates from the nitrogen within the molecule. For the monolayer in Figure 6.2(E) a second broad peak between a photon energy of 404 eV and 406 eV is clearly present. From previous studies of the somewhat similar molecule of zinc protoporphyrin, the zinc atom was reported to be pulled out of the molecule[127] when deposited on an oxide surface. In our experiment the same situation might be present, indicated by the peak between 404.8 eV, though some of the are still intact. The ratio between the two nitrogen peaks suggest that probably half of the molecules have suffered from the loss of zinc. The loss of the zinc from the molecules is due to the adicic nature of the rutile TiO_2(110) substrate.[127, 203]

The O 1*s* spectra for the multilayer and the monolayer are shown in Figure 6.2(G) and Figure 6.2(H), respectively. For the multilayer coverage the side groups of the molecule will be the main contribution and the substrate are not expected to been seen. When the monolayer spectrum is recorded the

substrate is dominating and therefore the oxygen peaks in the two spectra are shifted.

The XPS measurements for the multilayer and the monolayer for the Zn $2p$ are shown in Figure 6.2(I) and Figure 6.2(J). A reduction in the intensities are presence but we can not calibrate the binding energies reliably.

In order to reliably identify and quantify charge transfer, the participator and spectator components of the auto-ionisation decay channels, arising from an initial X-ray absorption excitation, must be identified. Moreover, the energetic position at which spectator electrons enter the spectrum needs to be determined accurately. Aside from the inaccuracies of counting spectator electrons as participator, it is essential to include as many participator electrons as possible in the analysis of the channel in order to reduce the effects of noise in the signal. These effects can be quite large, significantly hindering charge transfer assessment. The resonant photoemission data was obtained by measuring the valence-band photoemission up to 19 eV binding energy for the range of photon energies covering the N $1s$ absorption edge in 0.1 eV steps. Collecting the data in this energy window ensured that the lowest unoccupied levels were covered. Measuring the valence band spectra provides information about any interesting behaviour in the means of charge transfer. In Figure 6.3 the two dimensional resonant photoemission spectroscopy, RPES, spectrum of the multilayer is shown. It was recorded by scanning the photon energy, from 397 eV to 406 eV, over N $1s$ absorption edge, and thereby covering the lowest unoccupied level.

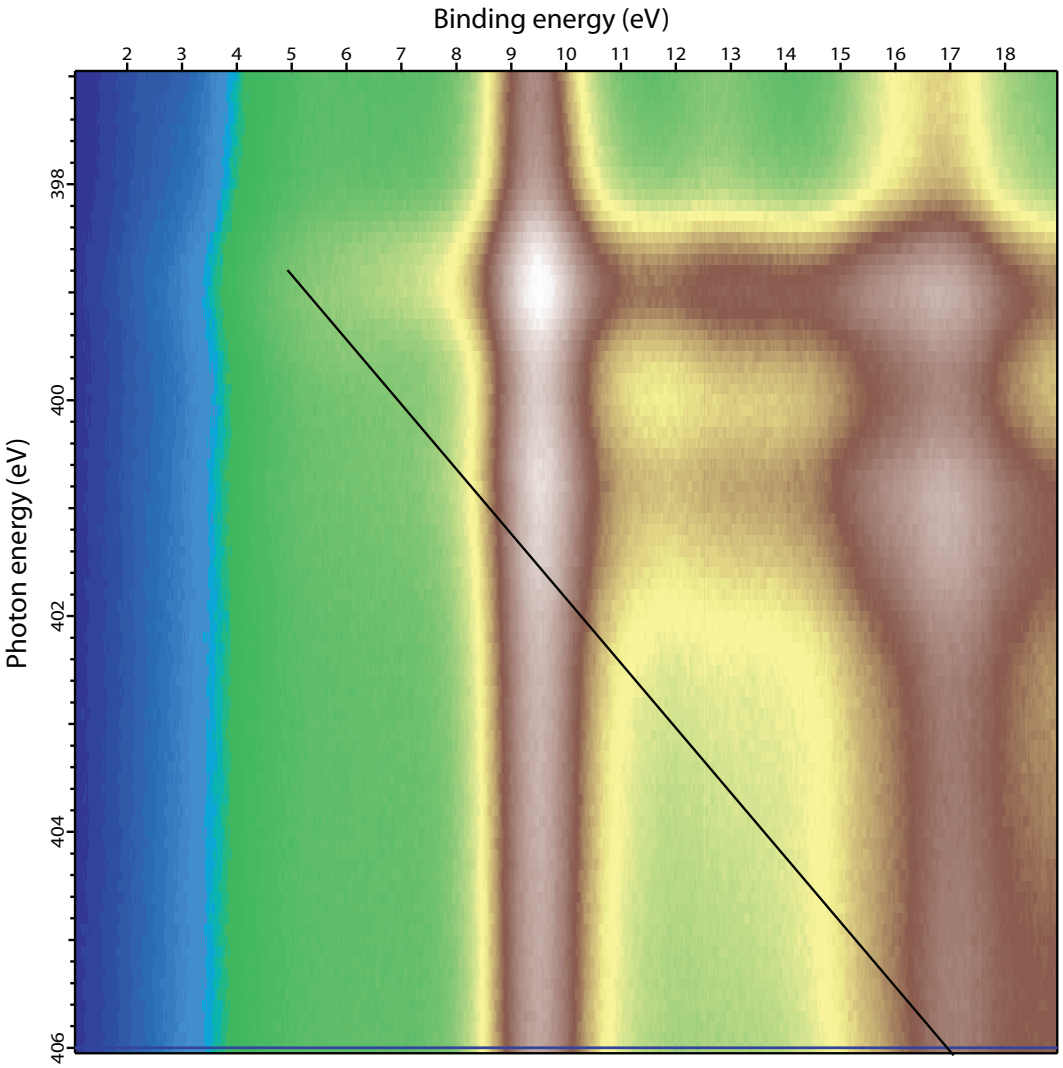

Figure 6.3: Resonant photoemission spectra of the c-**P**12 molecule on the rutile $TiO_2(110)$ surface. The horizontal axis represents the binding energy and the vertical axis the photon energy. The placement of the black line is discussed below.

The two main vertical features between 8.5-10.5 eV and again 15-18 eV binding energy, truly dominate the spectrum with an intense peak at 399 eV. The two main lines are the result of direct photoemission. The interesting enhancement in intensity at a binding energy of 8.5-10.5 eV and a photon energy of 399 eV can either be a result of resonant photoemission or an overlap of Auger decays. The Auger decays processes disperse with constant kinetic energy, due to the linear relationship between $h\nu$ and the binding energy[156, 158], which enable their separation by subtracting the pre-edge structure from

each recorded photon energy. The pre-edge structure in this setup is found below a photon energy of 398 eV, and is here chosen to be 397 eV, since this is where the photon energy scan starts. The pre-edge structure is obtain by making a horizontal line scan at constant photonenergy of 397 eV. In this case at a photon energy of 397 eV and from a binding energy of 0 eV to 19 eV. The pre-edge structure is indicated by the solid blue spectrum in Figure 6.4. For selected constant photon energies starting at 397 eV, 398.4 eV, 398.9 eV, 399.4 eV, 399.9 eV, 400.2 eV, 401.2 eV, and 406 eV similar integration have been done over the two-dimensional resonant photoemission spectrum for the c-**P**12 porphyrin nanorings. The two extremes obtained at 398.9 eV and 406 eV are labelled in the Figure 6.4 together, with the pre-edge structure at 397 eV.

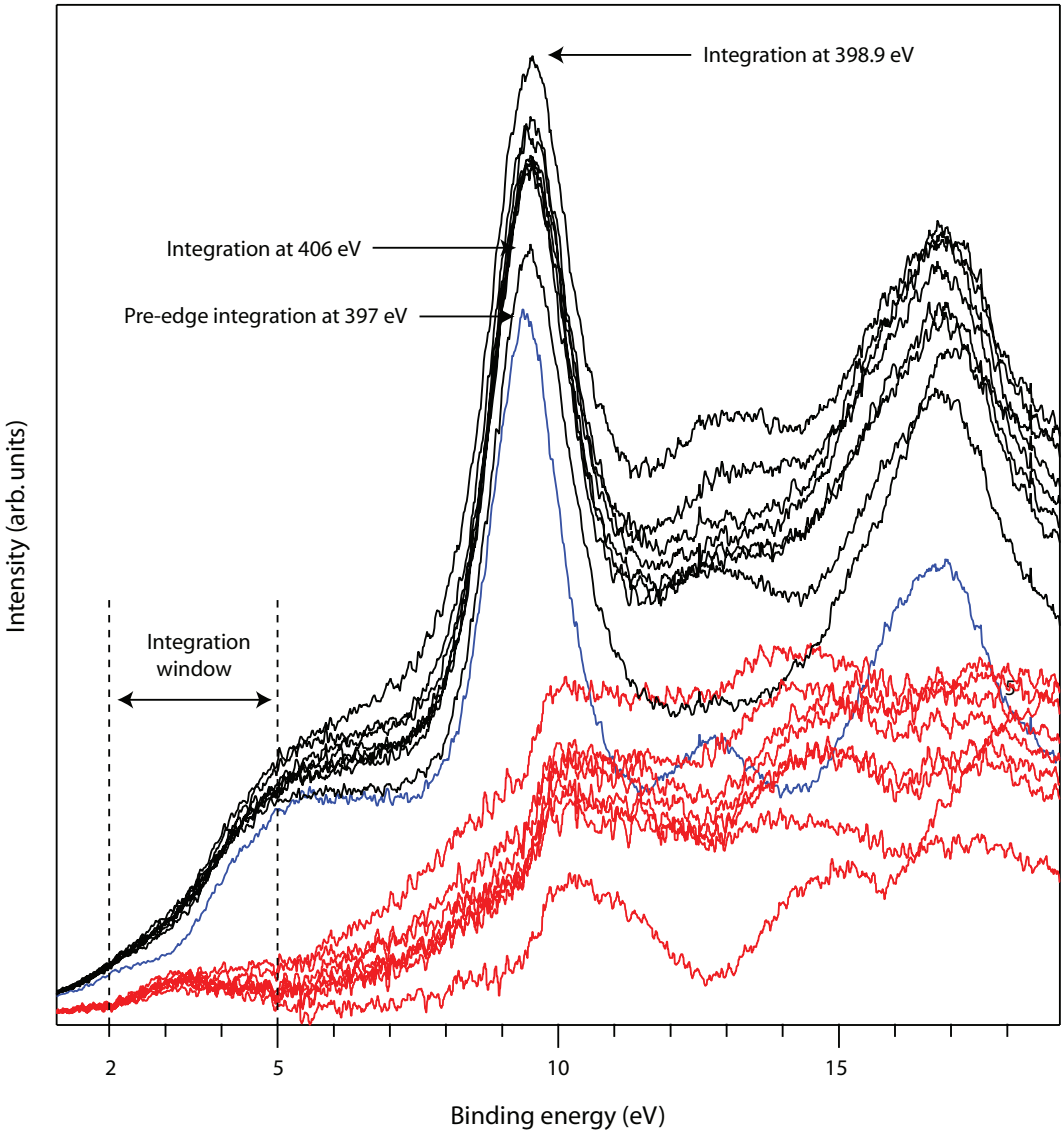

Figure 6.4: Integration over the two-dimensional RPES scan at constant photon energies. The dotted lines indicates the the result after the integration. The blue solid line is the integration over the pre-edge structure. The red solid lines in the bottom is the results after subtraction the pre-edge structure from the integrations. The integration window between 2 eV and 5 eV binding energy is indicated.

These are indicated by the black curves in Figure 6.4. When the pre-edge structure, indicated by the solid blue line, is subtracted from each of the integration spectra above the N 1s absorption edge are indicated by the red solid lines in Figure 6.4. A clear common feature for each of the subtracted spectra are the broad peak between 2 eV and 5 eV binding energy. An indication of the feature is also found in the two-dimensional resonant photoemission spectrum

in Figure 6.3. At a photon energy of 399 eV and at a binding energy of 3.5 eV a faint feature is located. This constant feature for each of the integrated photon energies therefore suggest the an integration window well above any contribution from Auger processes. This finding we can place the black solid line in Figure 6.3. This line represent the constant kinetic energy, starting at the binding energy of 5 eV, and it takes the presented shape due to linear relationship, $E_{\mathrm{kin}} = \hbar\nu$. The binding energy of 5 eV is also the lower limit of the main Auger peak, having a bright white feature at a binding energy of 9.5 eV. Any features at lower binding energy in that of the constant kinetic energy line will be due to photoemission and resonant photoemission only. This is shown in Figure 6.5. In Figure 6.5 the RPES spectrum is normalized to the LUMO found at a photon energy of 399 eV, as is the corresponding XAS spectrum which is also shown.

The Auger decay matrix element influences the intensity of resonances through the Auger transition rate that is given by a Fermi's Golden Rule treatment of the transitions (see Chapter 2. For a system where no charge transfer can occur, following normalization to the LUMO resonance the intensity will be reflected by the matrix element from the participator channel. An increase in the participator LUMO+1 can then occur through an increase in matrix element for the RPES representing the LUMO+1 or a decrease of the matrix element of RPES representing the LUMO. The matrix elements are dependent upon the Coulomb operator-modified overlap between the initial and final state wavefunctions of the system. Assuming the applicability of single electron states, this takes the form $< \phi^*_{\mathrm{occ}}\phi^*_k \mid 1/r \mid \phi_{\mathrm{N1}s}\phi_{\mathrm{unocc}} >$ where $< \phi^*_{\mathrm{occ}} \mid$ represents the state of a hole in the occupied orbitals of the low binding energy region of the valence band that are involved in participator decay, ϕ^*_k is the electron emitted, $\phi_{\mathrm{N1}s}$ represents the state due to the core-hole, and ϕ_{unocc} represents the core-excited unoccupied state (i.e., LUMO, LUMO + 1, etc.). An increase in matrix element of the RPES representing the LUMO+1 would then be motivated by a decrease in the spatial extent of the LUMO+1 or the low binding energy valence states, yielding a smaller spatial separation

between these orbitals, which feature in the initial- and final-state wavefunctions. Similarly, a decrease in the matrix element representing the LUMO would be motivated by an increase in the spatial extent of the LUMO or the low binding energy valence states. It is noted that matrix elements associated with the XAS signal have not been considered. These are neglected on the basis that many more states contribute to the intensity of this signal; hence, changes to the top of the valence band are much less important as compared to the affect on the participator signal. Therefore, choosing the LUMO intensities as normalization points for both the RPES and XAS spectra allows the investigation of any changes to the spectra. If any changes are present between the multilayer and monolayer, which will be analyzed in the following, it can be explained by charge transfer between the molecule and the surface.[18]

The two-dimensional monolayer RPES spectrum of the c-**P**12 molecule on the rutile TiO_2 surface is shown in Figure 6.6. This spectrum was acquired in a similar way in that of the multilayer spectrum. The somewhat faint vertical line found between a binding energy of 8.5 eV and 10.5 eV arises from the molecule. On a clean TiO_2(110) surface (not shown) this would not be present as we would expect. In contrast to the multilayer in Figure 6.3 the monolayer (Figure 6.6) displays an intense broad vertical band between 3 eV and 7 eV binding energy is the direct valence band photoemission from the substrate.

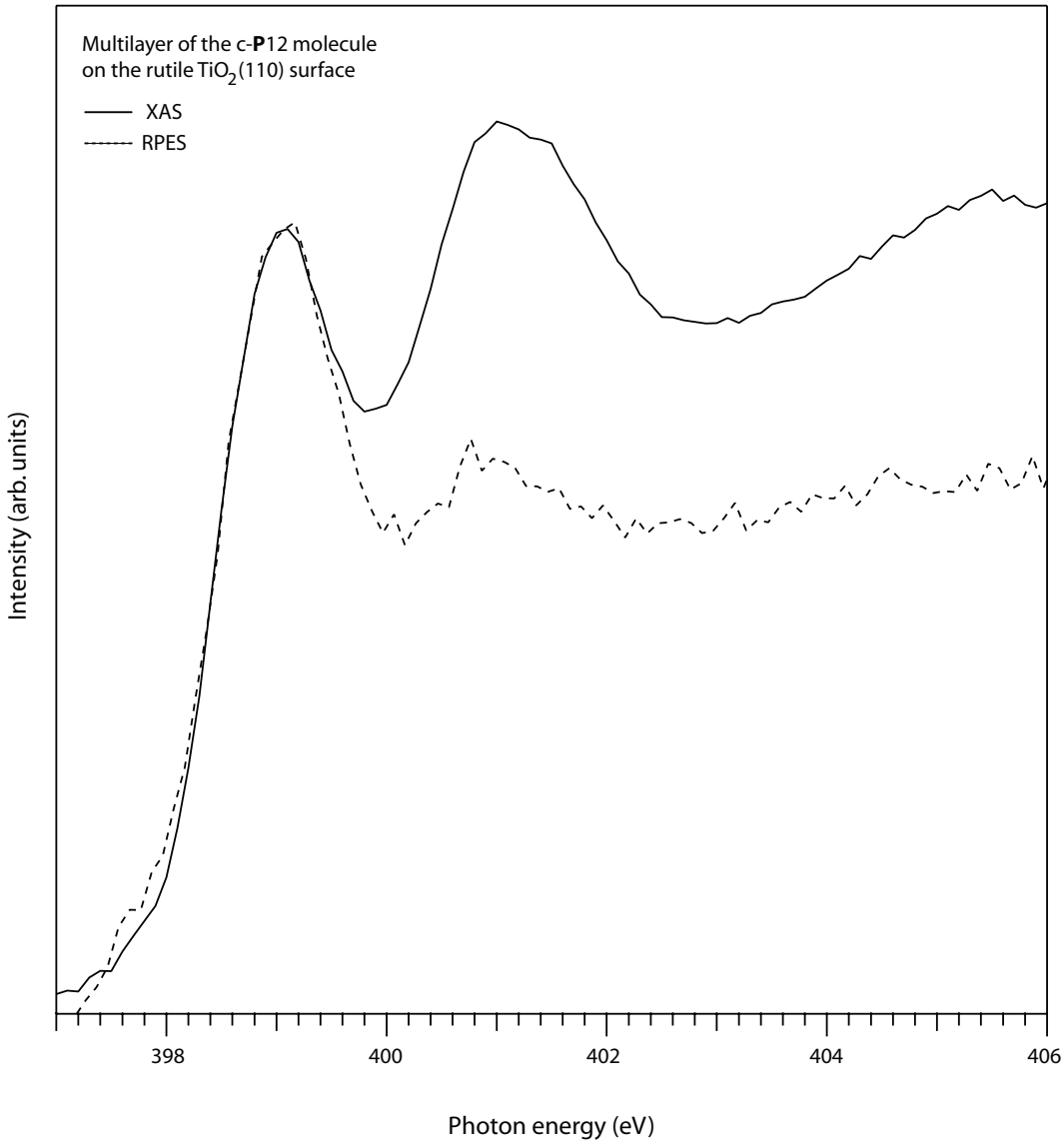

Figure 6.5: The N 1*s* RPES and XAS spectra of the c-**P**12 on the rutile $TiO_2(110)$ surface for the multilayer.

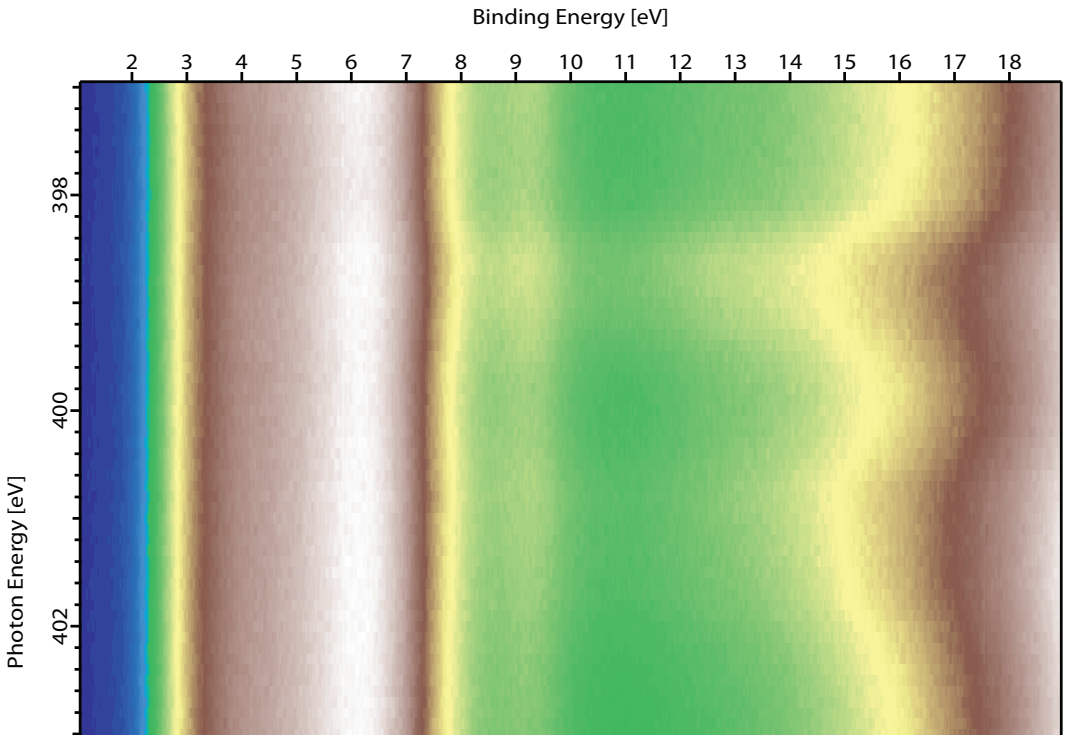

Charge transfer between the molecule and the substrate, in either direction, depends on the energetics of the lowest unoccupied molecular orbitals with respect to the substrate density of states. If the LUMO lies within the band gap of the TiO_2 surface then charge transfer from this state is not possible. In the core-excited state, the presence of the core-hole can lead to the LUMO state being excitonically pulled down so that it crosses into the band gap of the TiO_2 surface.[155] We can measure the position of the core-excited LUMO, with respect to the band gap, by placing the calibrated N 1*s* XAS and valence-band photoemission for each monolayer on a common energy scale,[20] as in Figure 6.7. The alignments of the spectra are done along the lines explained in Chapter 3. Here the valence band have been calibrated to the vacuum level at 27 eV of the TiO_2(110) surface, providing a common energy scale in ionization potential[20]. The data show that the LUMO of all the molecule lie above the band gap in the core-excited state. This provides a theoretical transfer of electrons from all the vibrational states of the core-excited LUMO.

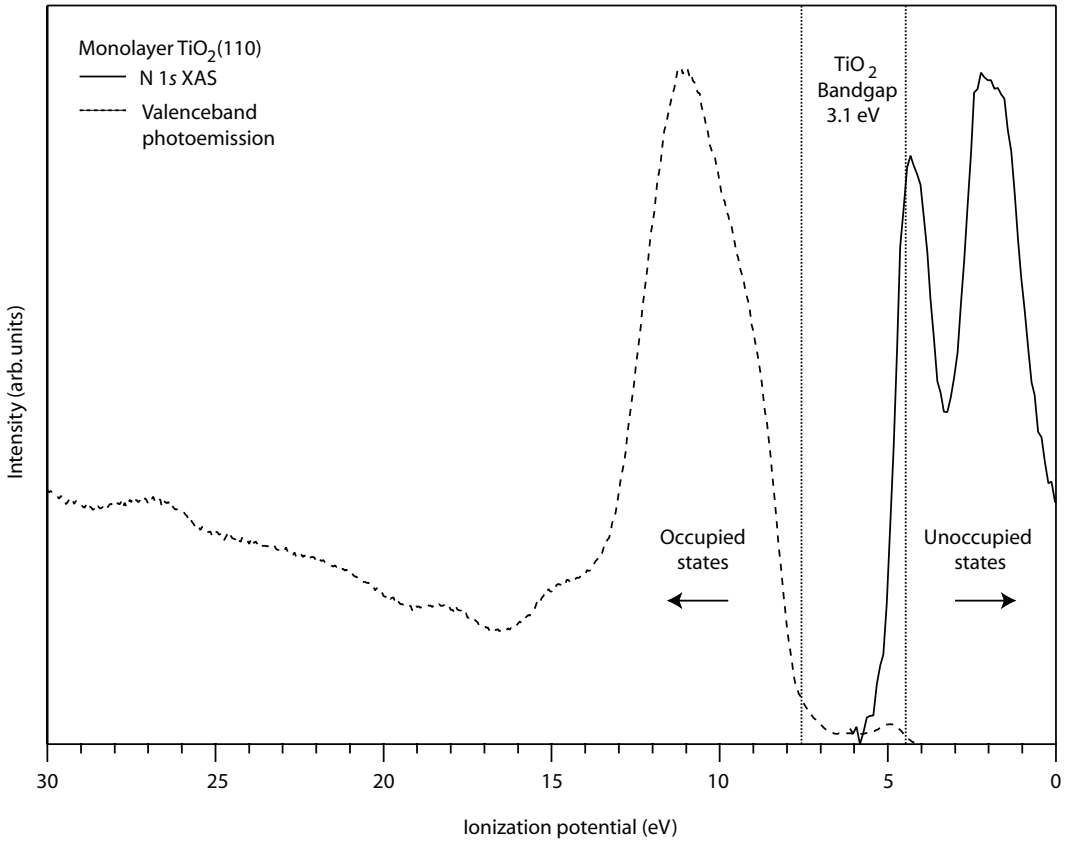

Figure 6.7: Energy level alignment of the substrate valence band and the unoccupied molecular orbitals of the molecule for c-**P**12 molecule on the rutile TiO_2(110) surface.

Using the core-hole clock implementation to estimate the charge transfer times out the core-excited states, relies on the fact having at least one of the core-excited states lying within the band gap of the substrate[156], normally the LUMO, but in some cases also the LUMO+1 lays with in the band gap as well.[126] If the LUMO state is located within the band gap, no transitions from this state to the substrate are allowed[156], and the LUMO state becomes a benchmark, to which all the higher lying resonances can be normalized. Comparing the losses of intensity between the the higher lying states in the integrated XAS and RPES spectra for the monolayer it is possible to estimate the charge transfer out of the higher lying states in the orders of the core-hole life time.[156] In the case of the LUMO laying within the band gap the difference between the integrated XAS and RPES are quite profound.[23, 126] The XAS spectrum will still display the higher laying LUMO states, whereas a

depletion of the these states will be present in the integrated RPES spectrum, due to the charge transfer process. From the difference in these intensities and the core-hole clock implementation, the charge transfer time between the molecules and the substrate can be extracted.

In our case, as seen in Figure 6.7, all the unoccupied states lie above the band gap of the TiO_2 substrate. This allows potential charge transfer from all the core-excited states to take place. This mean that all the states could be depleted. Figure 6.8 shows the integrated XAS and RPES spectra for a monolayer of the c-**P**12 molecule on the rutile TiO_2 surface. When the multilayer coverage was the evaluated the resonant photo-emissions processes was found to take place between the biding energies of 2 eV and 5 eV. A similar integration window was used to obtain the RPES spectrum. Both spectra were normalized to the LUMO resonance found at 399 eV.

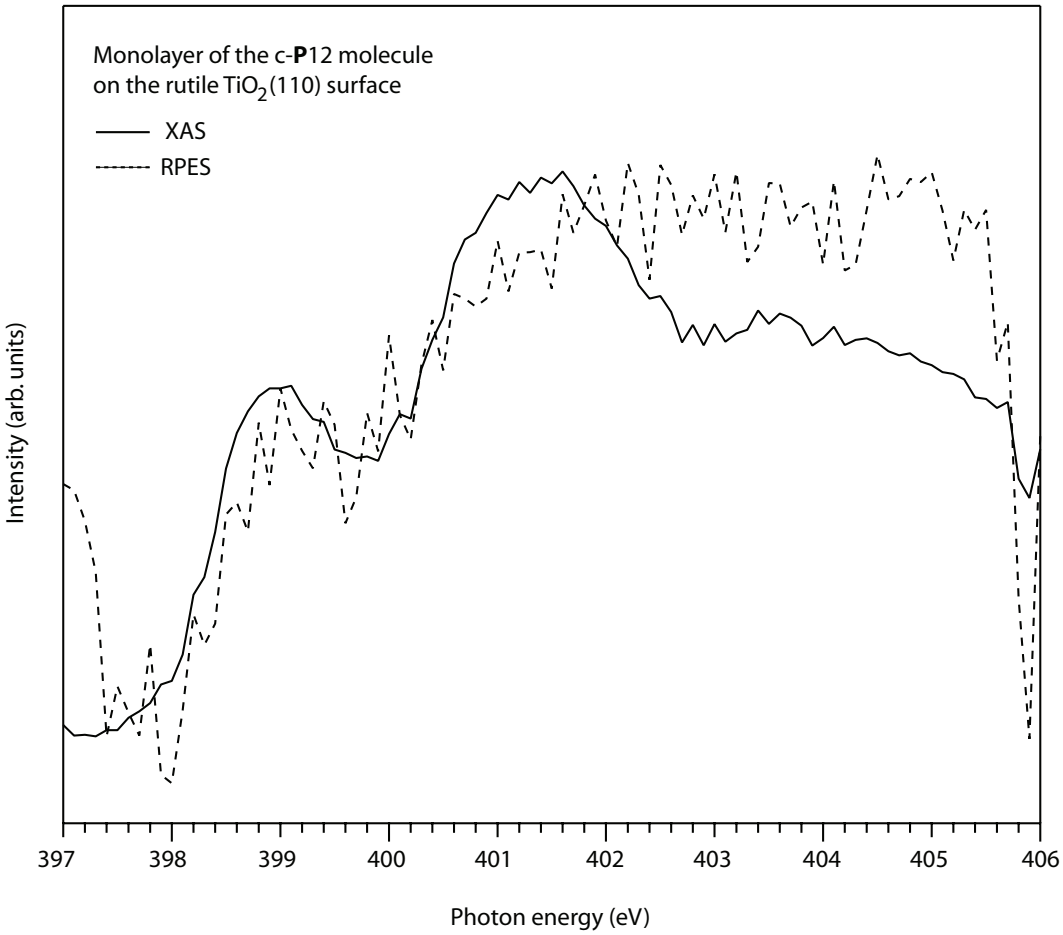

Figure 6.8: The N 1*s* RPES and XAS spectra for a monolayer coverage of the c-**P**12 molecule on the rutile $TiO_2(110)$ surface.

Figure 6.8 clearly shows that the RPES spectrum displays a high level of noise. A highly generous interpretation of the RPES spectrum would say that the RPES spectrum to some extent follows the one of the XAS when normalized to the intensity of the LUMO. Figure 6.8 underlines the prediction obtained from Figure 6.7, that there potentially is charge transfer out of all the core-excited states. Even though that we can not estimate any charge transfer time out of the core-excited states, the results are still encouraging. In the pursuit of high efficient solar cells the highest amount of charge transfer from the molecule is wanted. Therefore having all the core-excited states of the molecule located above the conduction band edge of the substrate will be

the most promising path to follow.

6.4 The c-P12 molecule on Au(111)

In this section the results of the c-**P**12 molecule on Au(111) are presented. Similar to the measurement conducted on the rutile TiO_2(110) surface, the technique of XPS was employed to verify if any molecules were deposition on the Au(111) surface. The non-calibrated XPS datasets are display in Figure 6.9

The different datasets displayed in Figure 6.9 clearly show that molecules have been deposited on the surface. Figure 6.2(A) and Figure 6.2(B) which show the valence band photoemission spectra a multilayer and monolayer coverage, where used to identify if the following measurements where conducted for either monolayer or multilayer. The small peak a 3 eV in Figure 6.9(A) is the contribution from the HOMO of the molecule, and is found at the same photon energy disregarding the surface, as we would expect. In Figure 6.9(A) shows the valence band for the monolayer coverage. The steep slope found at 0 eV is the Fermi level of the Au(111) surface. Between a photon energy of 8 eV and 10 eV a shoulder to the main peak is found. This a contribution from the molecule and was used as an indication if any molecules have been deposited on the surface. In the same spectrum two peaks are found around the photon energies of 23.5 eV and 27.5 eV. They are peaks originating from the gold substrate.

In Figure 6.9(C) and (D) the spectra for C 1s measurements for both the multilayer and the monolayer are shown, respectively. In contrast to the similar C 1s spectra for the TiO_2(110) surface, no residual solvent contribution is recorded for for the monolayer on the Au(111) surface. The solvent probably does not bond to the gold surface as efficient as in that of the rutile TiO_2(110) surface, hence no residual solvent is observed here. The C 1s monolayer spectrum in Figure 6.9(D) is somewhat nosier due to the lower coverage compared to the corresponding multilayer spectrum in Figure 6.9(C).

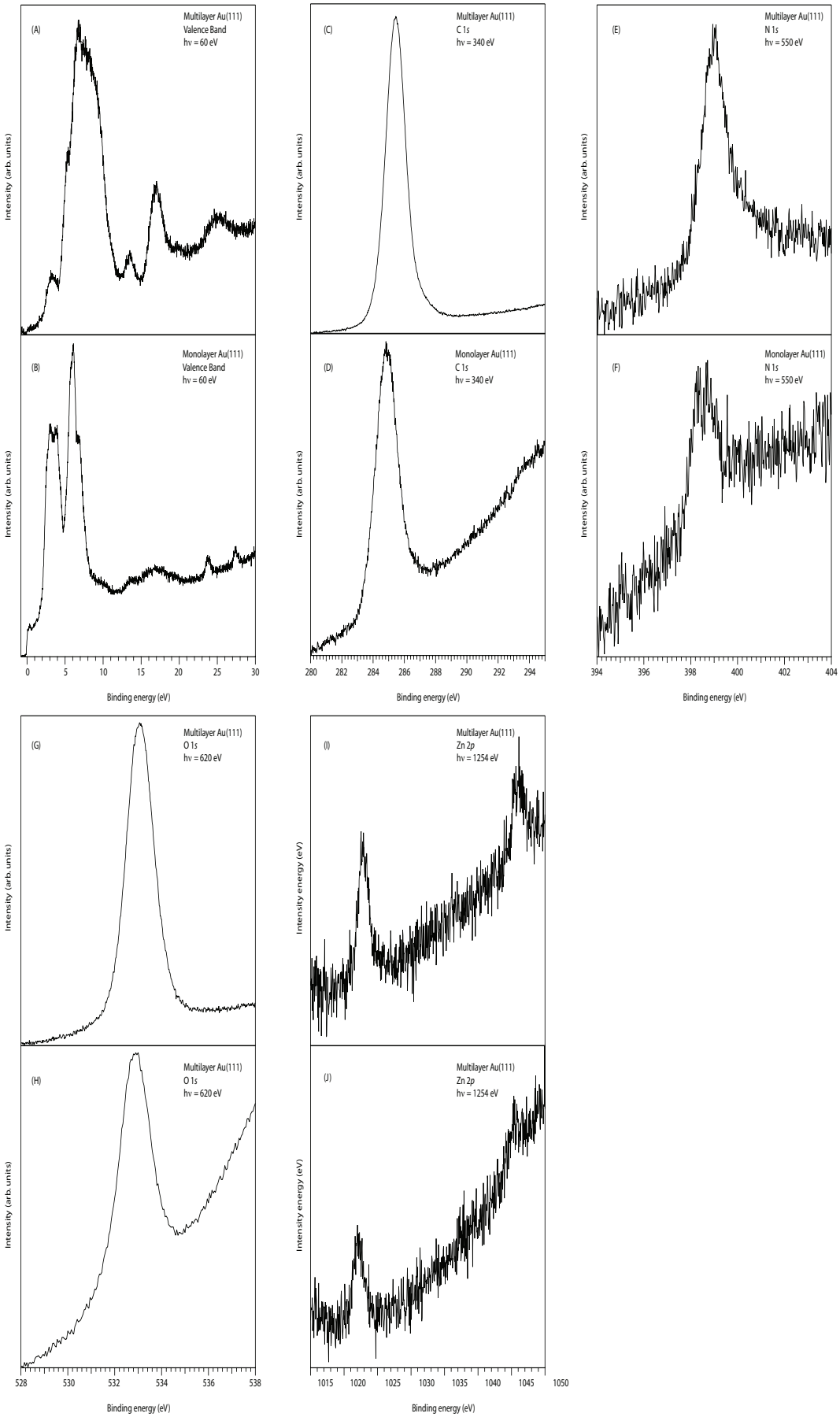

Figure 6.9: XPS data for the c-**P**12 molecule on the rutile Au(111) surface.

Considering the spectra in Figure 6.9(E)-(J) the only main difference the multilayer and the monolayer are the level of noise due to different coverages. For the monolayer N 1*s* spectrum in Figure 6.9(F) we note there is no second peak, which were recorded when the molecule where deposited on the TiO_2 surface. The lack of this second peak is due to the metallic substrate and the zinc atom is not pulled out of the molecule. All the molecules can therefore be regarded as intact.

One approach toward determining if charge transfer could be possible between a molecule and the substrate is by measuring the spatial overlap between the LUMO resonance of the molecule and the orbitals of the surface. Along the lines of the details in Chapter 3 the angle resolved spectra provides the information about the orientation of the molecules on the surface. The dipole matrix element associated with excitation to the π^* orbitals is oriented perpendicular to the plane of the aromatic ring structure of the molecule. When the polarization vector of the light lies perpendicular to the molecular plane, the NEXAFS cross section will be maximized.[144, 150] The reverse being true of the intensity variation of the σ^* states.[144, 150].

In Figure 6.10 the spectra over the N 1*s* for a variety of angles for the c-**P**12 molecule on the Au(111) surface. The spectra have been corrected for undulator intensity variations and normalized to the continuum of states above the vacuum level at 420 eV. The angles shown are the ones between the surface normal and the wave vector of the radiation. This corresponds to the dominant component of the electric field vector to the surface plane. The azimuthal intensity variations can be neglected since the Au(111) substrate has a three-fold rotational symmetry[144, 150] and the molecules have a 12-fold rotational symmetry. The sharp low energy peaks below 405 eV are identified with the π^* unoccupied molecular orbitals.[127] The structure above a photon energy of 405 eV are identified with the σ^* states.[127]

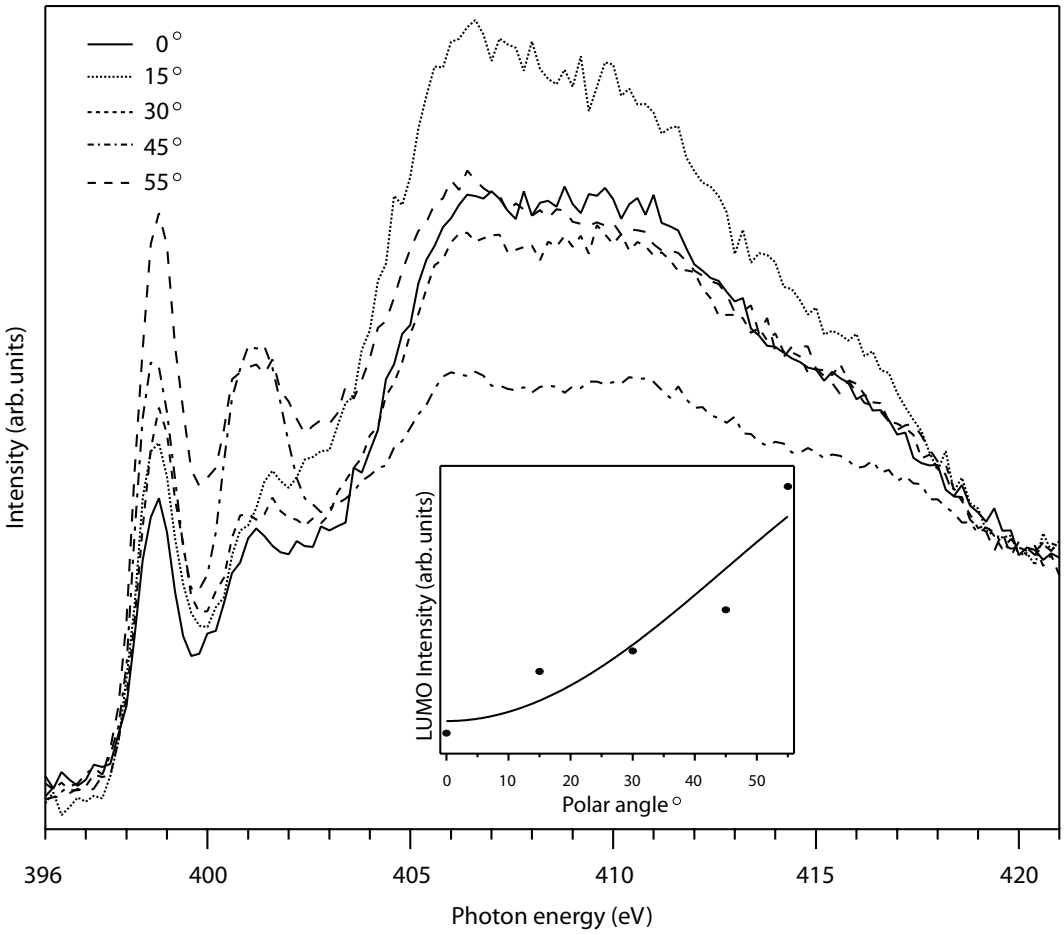

Figure 6.10: Angle resolved NEXAFS spectra N 1*s* for a monolayer of c-**P**12 molecule on Au(111). Inset shows the variation of the LUMO intensity with the angle of the incident radiation to the surface normal. The fit curve is the theoretical angular dependence for an aromatic ring with tilt angle of 45° to the surface normal, assuming a random azimuthal orientation and linear light polarisation[144, 150]. Photon resolution was ≈ 100 meV.

The π^* intensity takes its highest value when the electric field vector is 55° to the surface plane. The π^* intensity obtains it's minimum value when the electric field vector is parallel to the surface at 0°. The variation of LUMO intensity with angle for the c-**P**12 molecule reveals a tilt of 86 ± 10° shown in the inset. This curve is based on perfect linear polarisation of the light and an averaged azimuthal orientation of the nitrogen atoms within the ring structure. Even through the spectra have been normalized to the continuum far above resonance some variation are still present, resulting in the somewhat high uncertainty of ±10°. Nevertheless the results show that the molecules

can be regarded as laying flat on the surface. This result of the adsorption geometry of the c-**P**12 molecule on the Au(111) is in good correspondence to previous reported scanning tunneling microscopy measurements of the c-**P**12 molecule on the similar surface.[37] A STM image of the porphyrin nanorings are shown in Figure 6.11

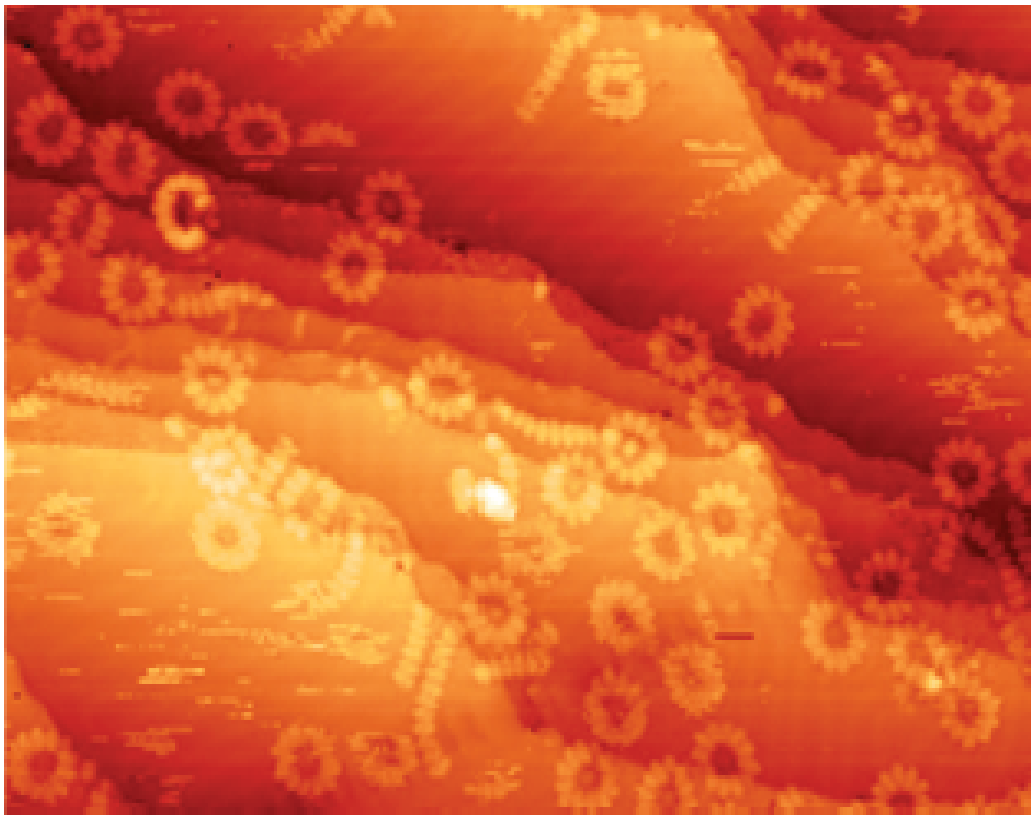

Figure 6.11: The c-**P**12 molecules on the Au(111) surface. The samples examined by NEXAFS and STM are not the same. Reproduced from reference [37].

The porphyrin nanoring possessing this adsorption geometry parallel to the Au(111) surface will provide spatial overlap between the $5d$ orbitals of the Au(111) surface and the LUMO orbital of the molecule. This would potentially facilitate charge transfer between the molecule and the surface.

Resonant photoemission spectra of the c-P12 molecule the Au(111)

The two-dimensional resonant photoemission spectra of the c-**P**12 molecule the Au(111) surface for the multilayer and for the monolayer are shown in Figure

6.12. The datasets were obtained by measuring the valence band photoemission up to 16 eV binding energy for the range of photon energies covering the N 1*s* absorption edge in 0.1 eV steps.

For the multilayer in Figure 6.12(A) we immediately see a dominating vertical line between a binding energy of 9 eV and 11 eV. At this coverage no contributions from the substrate are expected, therefore only the c-**P**12 molecule will be present in the spectrum. In good correspondence with literature[204] this line at binding energy of 9 eV and 11 eV originate from the zinc atoms within the molecule. We note that it is found in the same binding energy region as of when the experiments where carried out in the rutile TiO_2(110) surface as we would expect. The somewhat faint, compared to that just mentioned, vertical line between a binding energy of 5 eV and 7 eV originates from the Au(111) substrate. In the case of the medium layer shown in Figure 6.12(B) the features from the substrate and the contribution from the molecules take more or less the same intensity. The contribution from the substrate is located between a binding energy of 1.5 eV and 7 eV and the molecule contributes between 9 eV and 11 eV. Moving on to the monolayer shown in Figure 6.12(C) the substrate is truly dominating the spectra between 1.5 eV and 7 eV. The faint line found between a binding energy of 9 eV and 11 eV is the contribution from the molecule.

When the experiments where conducted on the rutile TiO_2(110) surface, the multilayer coverage showed a faint feature between a biding energy of 2 eV and 5 eV. For the multilayer coverage when the Au(111) surface was employed only the features from the molecules and the substrate are observed.

The spatial overlap between the molecules π^* orbital and the orbitals of the Au(111) surface could potentially lead to a high amount of charge transfer between the molecules and the surface. Further investigation of this potential charge transfer between the would be to enlighten the situation from a energetic point of view. Following this path the core-hole clock implementation of resonant photoemission outlined in Chapter 2 the the valence band and NEXAFS spectra are aligned on a common binding energy scale[20], see Chapter 3.

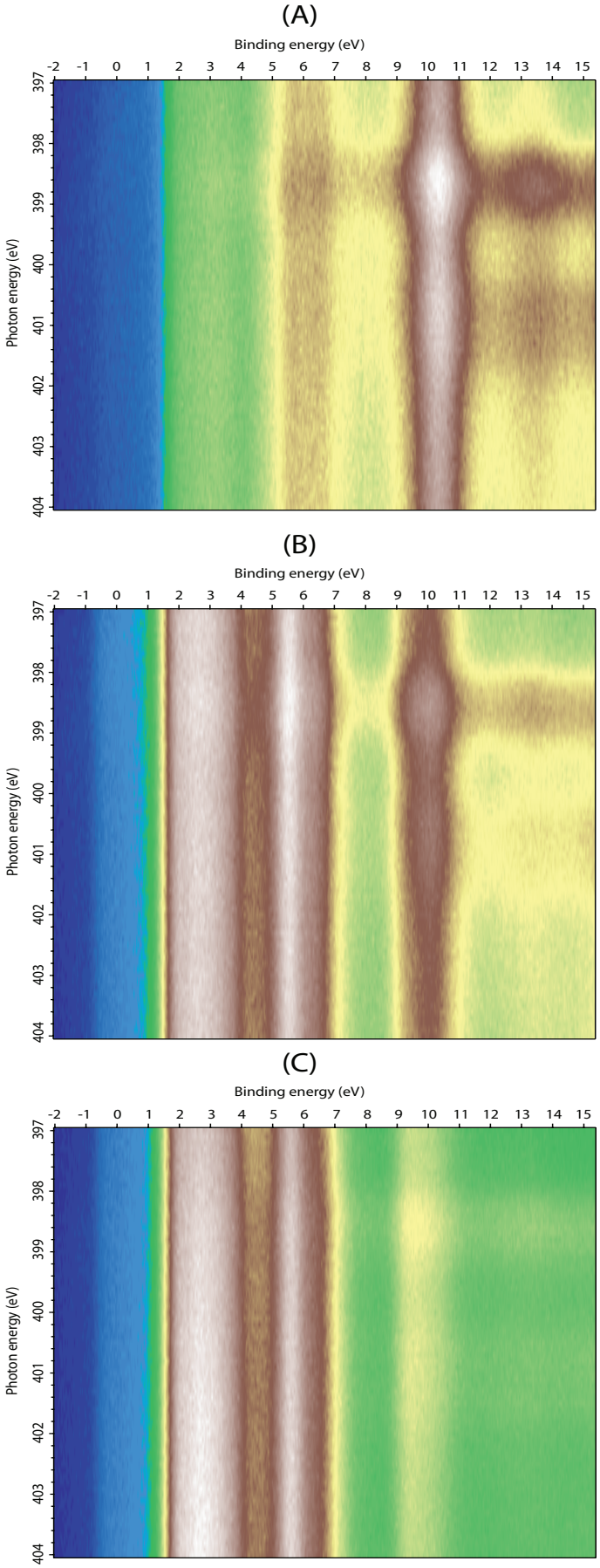

Figure 6.12: N 1*s* resonant photoemission for a monolayer (A) for the medium layer (B) and for the multilayer (C) of c-**P**12 molecule on Au(111).

This is presented in Figure 6.13. Having a metallic substrate the Fermi level is used as a calibration point and is defined to be at 0 eV binding energy.

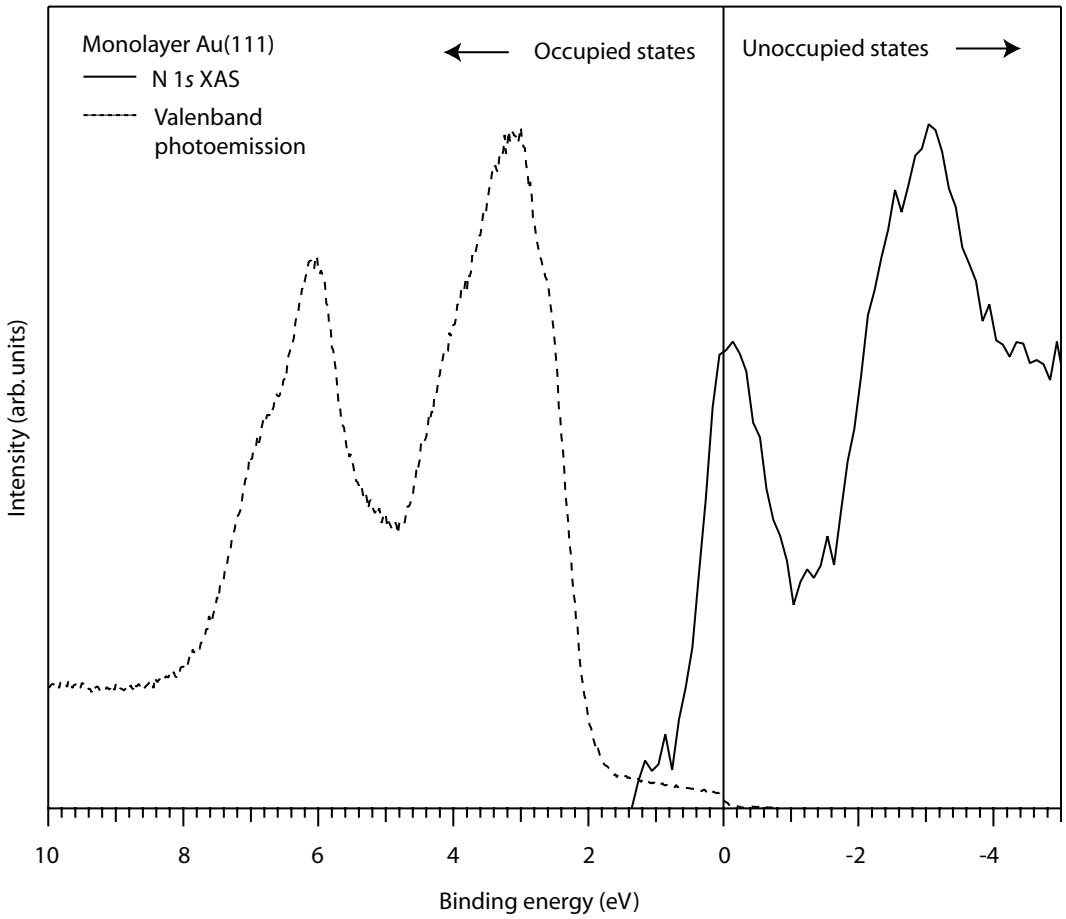

Figure 6.13: Energy level alignment of the molecule unoccupied and the substrate occupied states. Both spectra were acquired with the sample in normal emission. The XAS spectrum is recorded over the N 1s edge. The Fermi level of the substrate is used at calibration for the binding energy.

Figure 6.13 shows that the core-excited LUMO and LUMO+1 overlaps with the unoccupied states of the substrate. This means that after resonant excitation charge transfer from these molecular states can take place. Outlined in Chapter 2 at least on of the core-excited states of the molecule needs to overlap with occupied states of the substrate, providing a forbidden transition out of this state. In our case all the unoccupied states in the core-excited state of c-**P**12 molecule on the Au(111) surface lie above the Fermi level of the Au(111) surface so the initial conclusion is that charge transfer from the

molecule is possible due to the spatial overlap between the unoccupied states of the molecule and the substrate. This is underlined by comparing the RPES and XAS spectra for the monolayer coverage on the Au(111) substrate. This is done in Figure 6.14. They are both normalized to the LUMO intensities and with the integration windows being between a binding energy of 2 eV and 5 eV. Similar, to the case when the rutile TiO_2(110) substrate was employed the generous interpretation of the RPES spectrum would say that it follows that of the XAS. Figure 6.14 underlines the prediction obtained from Figure 6.13, that all the core-excited states can potentially participate in charge transfer. Similar, conclusion as with the previous substrate, this result is encouraging in the pursuit of high efficient solar cells.

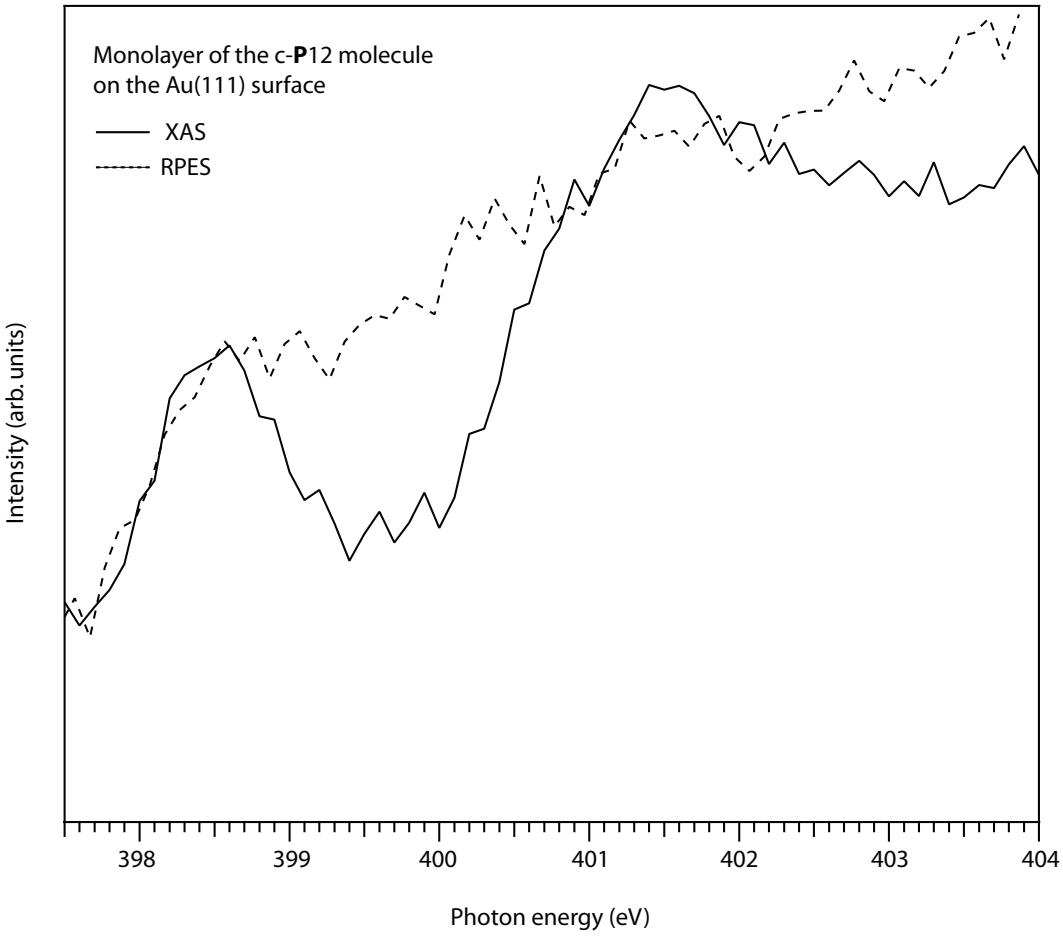

Figure 6.14: The N 1*s* RPES and XAS spectra for a monolayer coverage of the c-**P**12 molecule on the Au(111) surface

6.5 Conclusion

The energy alignment for the c-**P**12 molecule on the rutile TiO_2(110) surface and for the Au(111) surface both states that all the core-excited states electronically overlaps with the unoccupied states of the surface, providing charge transfer out of all of these states. Having no core-excited states laying within the band gap of the rutile TiO_2(110) surface or below the Fermi edge for the Au(111) it is not possible to estimate a charge transfer time out of these states within the realms of the core-hole clock implementation. However for a real solar cell application all of the core-excited states should be located across the unoccupied states of the substrate to facilitate high transfer efficiency.

When probing the N 1*s* XAS, a core exciton – bound electron-hole pair – will be created, whereas in a real dye-sensitized solar cell a valence exciton will be created. The presence of a hole in both XAS and optical absorption shift the unoccupied states to higher binding energies with respect to the ground state.[23, 125, 126, 155] The binding energy of the excitons, equivalent to the amount by which the unoccupied levels shift,(about 1.5 eV[18]) is attributed to a combination of the Coulomb interaction between the hole and excited electron, and the rehybridisation of the molecular states upon core- or valence-hole creation.[155] This result shows for sure that the LUMO would lie above the conduction band edge of the TiO_2 substrate in a real solar cell.

Chapter 7

Summary and conclusion

The aim of all the research in this thesis was to gain a better understanding of charge transfer between organic molecules and surfaces, especially relating to the situation observed in dye sensitized solar cells. This broad theme can be further subdivided into two main avenues of research. Firstly, there was the X-ray adsorption studies of the single molecule magnets on the two different surfaces in that of rutile $TiO_2(110)$ and the Au(111) single crystal. The NEXAFS analysis for the $Mn_{12}(benzoate)_{16}$ on the rutile $TiO_2(110)$ surface show that the expected oxidation states for the single molecule magnet undergo a reduction of its core in the sub-monolayer regime facilitating a unwanted charge transfer between the molecules and the substrates. In the multilayer the intermediate layer protects the magnet core and no reduction is observed, hence their magnetic properties are maintained. Replacing the ligand shell with the must larger terphenyl-4-carboxylate ligand provides a substantial degree of protection for the oxidation states even for the sub-monolayer coverage on both the gold and titanium dioxide surfaces. This shows that we are able to deposit the complex single molecule magnets without alternating the magnetic core upon deposition, which are highly encouraging in the pursuit for nano-scale electronics.

As well as studying molecules adsorbed onto metal and semiconducting surfaces, we also studied charge transfer from adsorbed molecules into the conduction band of a semiconductor substrate. Previously, photoemission had

been used to perform a core-hole clock analysis, which is described fully in chapter 2. Research within our group[25] have shown that the core-hole clock implementation can be adapted to the technique of resonant inelastic scattering. Here we revisit the system of bi-isonicotinic acid adsorbed on the rutile $TiO_2(110)$ surface. In contrast to the single molecule magnets where charge transfer was an unwanted effect within the system, charge transfer from either the molecule to substrate or within the molecule itself will here be the prime goal of this research. By measuring the change in the elastic peak for the monolayer for the LUMO and LUMO+1, compared to the respective change for the multilayer we could reproduce the previous results of the charge transfer 2.9 ± 0.3 femtoseconds. Using the high resolution beamline of SEXTANS at the French National Synchrotron Facility of SOLEIL we discovered vibrational states as well as virtual states only present in the core-excited states of the molecule. These states prove to be highly important when charge transfer out of the higher lying states are evaluated. When the LUMO+2 resonance was probed, these states where masked by the inelastic scattering and we could therefore not estimate any charge transfer out of this state. During the resonant inelastic scattering process a core-hole is introduced on just one of the rings within the bi-isonicotinic acid. This core-hole can facilitate charge transfer within the molecule and might be the reason for the observed split of the HOMO peak when the LUMO+1 resonance is probed. The results suggest either ultra fast relaxation of bi-isonicotinic acid molecule or ultra fast charge transfer within the molecule. In the further investigation to enlighten this issue we suggest to conduct resonant inelastic scattering measurement on the isonicotinic acid.

In chapter 6 we studied the large and complex π-conjugated zinc porphyrin nanorings. Here we employed the techniques of resonant photoemission spectroscopy and near edge X-ray absorption fine structure. Our studies shows that the c-**P**12 molecules lies flat on the gold surface, which is in good correspondence to previous reports.[37] The resonant photoemission spectroscopy measure of the c-**P**12 molecules on both the rutile $TiO_2(110)$ surface and on

the Au(111) shows that all the core-excited states can potential participate in charge transfer into the substrates. Since all the core-excited states lies overlaps with the unoccupied states of the substrates estimates of charge transfer in the means of the core-hole clock implementation have not been conducted. Although the almost complete reduction of the participator peaks compared to previous studied molecules[23, 125, 126, 129] suggest ultrafast charge transfer around the molecule itself and its further reduction in the monolayer supports ultrafast charge transfer to the surface. Having all the core-excited states overlapping unoccupied states of the substrates are promising in the pursuit for new materials of renewable energy sources.

Chapter 8

Acknowledgements

I would like to thank my supervisor, James N. O'Shea, and my colleagues Andrew J. Britton, Matthew Weston, Robert H. Temperton and Andrew J. Gibson, as well as everyone in the NanoScience Group at the University of Nottingham. I would like to thank all the technical support at MAXlab, particulary the I311 and D1011 beamline managers, Karina Schulte and Alexei Preobrajenski. I would also like to thank Nicolaou Alessandro and Nicolas Jaouen for the technical support at the SEXTANS beamline at SOLEIL. I am grateful for the financial support through the Marie Curie Action - ITN SMALL network.

Bibliography

[1] R. P. Feynman, "There's Plenty of Room at the Bottom," *CalTech Engineering and Science*, vol. 23, pp. 22–36, 1960.

[2] Intel, "Microprocessor Quick Refeerence Guide," *http://www.intel.com/pressroom/kits/quickreffam.htm.*

[3] I. P. on Climate Change, *Climate Change 2007: The Physical Science Basis – Summary for Policymakers.* Geneva, Switzerland: IPCC Secretariat, 2007.

[4] T. Sekitani, M. Takamiya, Y. Noguchi, S. Nakano, Y. Kato, T. Sakurai, and T. Someya, "A large-area wireless power-transmission sheet using printed organic transistors and plastic MEMS switches," *Nature Materials*, vol. 6, pp. 413–417, 2007.

[5] L. Frazer, "Organic electronics: A Cleaner Substitute for Silicon," *Environmental Health Prospectives*, vol. 111, pp. A288–A291, 2003.

[6] A. J. Bard, R. Memming, and B. Miller, "Terminology in semiconductor electrochemistry and photoelectrochemical energy conversion," *Pure and Applied Chemistry*, vol. 63, pp. 569–596, 1991.

[7] M. Grätzel, "Photoelectrochemical cells," *Nature*, vol. 414, pp. 388–344, 2001.

[8] J. Winkler, *Titanium dioxide.* Vincentz Network, Hannover, 2003.

[9] NASA *http://earthobservatory.nasa.gov/*, September, 2013.

[10] W. West, "First Hundred Years of Spectral Sensitization," *Photographic Science and Engineering*, vol. 18, pp. 35–48, 1974.

[11] H. Gerischer and I. Mattes, "Über die Mitwirkung von Oberflächenzuständen bei Redoxreaktionen an Halbleitern," *Zeitschrift für Physikalische Chemie*, vol. 52, pp. 60–72, 1967.

[12] B. O'Regan and M. Grätzel, "A low-cost, high-efficiency solar cell based on dye-sensitized colloidal TiO_2 films," *Letters to Nature*, vol. 353, pp. 737–740, 1991.

[13] M. Grätzel, "Dye-sensitized solar cells," *Journal of Photochemistry and Photobiology C: Photochemistry Reviews*, vol. 4, pp. 145–153, 2003.

[14] L. E. Chaar, L. A. Lamont, and N. E. Zein, "Review of photovoltaic technologies," *Renewable and Sustainable Energy Reviews*, vol. 15, pp. 2165–2175, 2011.

[15] P. Persson, A. Stashans, R. Bergström, and S. Lunell, "Periodic INDO calculations of Organic Adsorbates on a TiO_2 Surface," *International Juornal of Quantum Chemistry*, vol. 70, p. 1055, 1998.

[16] L. Patthey, H. Rensmo, P. Persson, K. Westermark, L. Vayssieres, A. Stashans, Å. Petersson, P. A. Brühwiler, H. Siegbahn, S. Lunell, and N. Mårtensson, "Adsorption of bi-isonicotinic acid on rutile $TiO_2(110)$," *Journal of Chemical Physics*, vol. 110, pp. 5913–5918, 1999.

[17] P. Persson, S. Lunell, P. A. Brühwiler, J. Schnadt, S. Södergren, J. N. O'Shea, O. Karis, H. Siegbahn, N. Mårtensson, M. Bässler, and L. Patthey, "N $1s$ x-ray absorption study of the bonding interaction of bi-isonicotinic acid adsorbed on rutile $TiO_2(110)$," *Journal of Chemical Physics*, vol. 112, pp. 3945–3948, 2000.

[18] J. Schnadt, P. A. Brühwiler, L. Patthey, J. N. O'Shea, S. Södergren, M. Odelius, R. Ahuja, O. Karis, M. Bässler, P. Persson, H. Siegbahn, S. Lunell, and N. Mårtensson, "Experimental evidence for sub-3-fs

charge transfer from an aromatic adsorbate to a semiconductor," *Nature*, vol. 418, pp. 620–623, 2002.

[19] J. Schnadt, J. Schiessling, J. N. O'Shea, S. M. Gray, L. Patthey, M. K.-J. Johansson, M. Shi, J. Krempaský, J. Åhlund, P. G. Karlsson, , P. Persson, N. Mårtensson, and P. A. Brühwiler, "Structural study of adsorption of isonicotinic acid and related molecules on rutile TiO_2(110) I: XAS and STM," *Surface Science*, vol. 540, pp. 39–54, 2003.

[20] J. Schnadt, J. N. O'Shea, L. Patthey, J. Krempaský, N. Mårtensson, and P. A. Brühwiler, "Alignment of valence photoemission, X-ray absorption, and substrate density of states for an adsorbate on a semiconductor surface," *Physical Review B*, vol. 67, pp. 235420–235420–7, 2003.

[21] J. Schnadt, J. N. O'Shea, L. Patthey, L. Kjeldgaard, J. Åhlund, K. Nilson, J. Schiessling, J. Krempaský, M. Shi, O. Karis, C. Glover, H. Siegbahn, N. Mårtensson, and P. A. Brühwiler, "Excited-state charge transfer dynamics in systems of aromatic adsorbates on TiO_2 studied with resonant core techniques," *The Journal of Chemimical Physics*, vol. 119, pp. 12462–12472, 2003.

[22] J. Schnadt, J. N. O'Shea, L. Patthey, J. Schiessling, J. Krempaský, N. Mårtensson, and P. A. Brühwiler, "Structural study of adsorption of isonicotinic acid and related molecules on rutile tio_2(110)II: XPS," *Surface Science*, vol. 544, pp. 74—-86, 2003.

[23] L. C. Mayor, J. B. Taylor, G. Magnano, A. Rienzo, C. J. Satterley, J. Schnadt, and J. N. O'Shea, "Photoemission, resonant photoemission, and X-ray absorption of a Ru(II) complex adsorbed on rutile TiO_2(110) prepared by in situ electrospray deposition," *Journal of Chemical Physics*, vol. 129, pp. 114701–114701–9, 2008.

[24] H. McIlleron, M. Willemse, C. J. Werely, G. D. Hussey, H. S. Schaaf, P. J. Smith, and . R. Donald, "Isoniazid Plasma Concentrations in a Cohort of South African Children with Tuberculosis: Implications for

International Pediatric Dosing Guidelines," *Clinical Infectious Diseases*, vol. 48, pp. 1547–1553, 2000.

[25] A. J. Britton, M. Weston, and J. N. O'Shea, "Charge Transfer from an Aromatic Adsorbate to a Semiconductor TiO_2 Surface Probed on the Femtosecond Time Scale with Resonant Inelastic X-Ray Scattering," *Physical Review Letters*, vol. 109, pp. 017401–017401–5, 2012.

[26] J.-E. Rubensson, "RIXS dynamics for beginners," *Journal of Electron Spectroscopy and Related Phenomena*, vol. 110–111, pp. 135–151, 2000.

[27] H. Kallmann and M. Pope, "Photovoltaic Effect in Organic Crystals," *The Jopurnal of Chemical Physics*, vol. 30, pp. 585–586.

[28] M. R. Wasielewski, "Photoinduced electron transfer in supramolecular systems for artificial photosynthesis," *Chimical Reviews*, vol. 92, no. 3, pp. 435–461, 1992.

[29] H. L. Anderson, "Conjugated Porphyrin Ladders," *Inorganic Chemistry*, vol. 33, pp. 972–981, 1994.

[30] D. P. Arnold, D. Manno, G. Micocci, A. Serra, A. Tepore, , and L. Valli, "Porphyrin Dimers Linked by a Conjugated Alkyne Bridge: Novel Moieties for the Growth of Langmuir–Blodgett Films and Their Applications in Gas Sensors," *Langmuir*, vol. 13, pp. 5951–5956, 1997.

[31] J. R. Reimersa, T. X. Lüa, M. J. Crossleya, and N. S. Husha, "Molecular electronic properties of fused rigid porphyrin-oligomer molecular wires," *Chemical Physics Letters*, vol. 256, pp. 353–359, 1996.

[32] B. Jiang, S.-W. Yang, D. C. Barbini, and W. E. J. Jr., "Synthesis of soluble conjugated metalloporphyrin polymers with tunable electronic properties," *Chemical Communications*, vol. 2, pp. 213–214, 1998.

[33] S. M. LeCours, H.-W. Guan, S. G. DiMagno, C. H. Wang, and M. J. Therien, "Push–Pull Arylethynyl Porphyrins: New Chromophores That

Exhibit Large Molecular First–Order Hyperpolarizabilities," *Journal of American Chemical Society*, vol. 118, pp. 1497–1503, 1996.

[34] A. D. Jenkins, P. Kratochvíl, R. F. T. Stepro, and U. W. Suter, "Glossary of Basic Terms in Polymer Science," *International Unioun of Pure and Applied Chemistry*, vol. 68, pp. 2287–2311, 1996.

[35] L. R. Milgrom, *The Colours of Life: An Introduction to the Chemistry of Porphyrins and Related Compounds.* Oxford University Press, 1997.

[36] D. Dolphin, *The Porphyrins.* Academic Press, 1978.

[37] S. A. Svatek, L. M. A. P. ao, A. Stannard, M. B. Wieland, D. V. Kondratuk, H. L. Anderson, J. N. O'Shea, , and P. H. Beton, "Mechanical Stiffening of Porphyrin Nanorings through Supramolecular Columnar Stacking," *Nano Letters*, vol. 13, pp. 3391–3395, 2013.

[38] D. V. K. C. R. T. D. W. C. A. S. M. O. B. J. N. O. P. H. B. M. M. M. C. O'Sullivan, J. K. Sprafke and H. L. Anderson, "Vernier templating and synthesis of a 12-porphyrin nano-ring," *Nature*, vol. 469, pp. 72–75, 2011.

[39] C. J. Martin, C. L. W. III, and A. M. Ducatman, "The interpretation of zinc protoporphyrin changes in lead intoxication: a case report and review of the literature," *Occupational Medicine*, vol. 54, pp. 587–591, 2004.

[40] M. Verschoor, R. Herber, R. Zielhuis, and A. Wibowo, "Zinc protoporphyrin as an indicator of lead exposure: precision of zinc protoporphyrin measurements," *International Archives of Occupational and Environmental Health*, vol. 59, p. 613–621, 1987.

[41] A. A. Lamola and T. Yamane, "Zinc Protoporphyrin in the Erythrocytes of Patients with Lead Intoxication and Iron Deficiency Anemia," *Science*, vol. 186, p. 936–938, 1974.

[42] J. H. Burroughes, D. D. C. Bradley, A. R. Brown, R. N. Marks, K. Mackay, R. H. Friand, P. L. Burns, and A. B. Holmes, "Light-emitting diodes based on conjugated polymers," *Nature*, vol. 347, pp. 539–541, 1990.

[43] K. T. Kamtekar, A. P. Monkman, and M. R. Bryce, "Recent advances in white organic light-emitting materials and devices (WOLEDs)," *Advanced Materials*, vol. 22, pp. 572–582, 2010.

[44] A. Moliton, *Optoelectronics of Molecules and Polymers*. New York: Springer, 2006.

[45] H. Sirringhaus, N. Tessler, and R. H. Friend, "Integrated Optoelectronic Devices Based on Conjugated Polymers," *Science*, vol. 280, pp. 1741–1744, 1998.

[46] C. D. Dimitrakopoulos and P. R. L. Malenfant, "Organic Thin Film Transistors for Large Area Electronics," *Advanced Matrials*, vol. 14, pp. 99–117, 2002.

[47] Y. Guo, G. Yu, and Y. Liu, "Functional Organic Field-Effect Transistors," *Advanced Materials*, vol. 22, pp. 4427–4447, 2010.

[48] M. Granström, K. Petritsch, A. C. Arias, A. Lux, M. R. Andersson, and R. H. Friend, "Laminated fabrication of polymeric photovoltaic diodes," *Nature*, vol. 395, pp. 257–260, 1998.

[49] A. J. Moulé, "Power from plastic," *Current Opinion in Solid State and Materials Science*, vol. 14, no. 6, pp. 123–130, 2010.

[50] A. Facchetti, "π-Conjugated Polymers for Organic Electronics and Photovoltaic Cell Applications," *Chemistry of Materials*, vol. 23, pp. 733–758, 2011.

[51] A. Rose, Z. Zhu, C. F. Madigan, T. M. Swager, and V. Bulovi, "Sensitivity gains in chemosensing by lasing action in organic polymers," *Nature*, vol. 434, pp. 876–879, 2005.

[52] J. H. Wosnick and T. M. Swager, "Molecular photonic and electronic circuitry for ultra-sensitive chemical sensors," *Current Opinion in Chemical Biology*, vol. 4, pp. 715–720, 2000.

[53] W. Riess, T. A. Beierlein, and H. Riel, "Optimizing OLED structures for a-Si Display Applications via Combinatorial Methods and Enhanced Outcoupling," *Physica Status Solidi A*, vol. 201, no. 6, pp. 1360–1371, 2004.

[54] T. Dobbertin, M. Kroeger, D. Heithecker, D. Schneider, D. Metzdorf, H. Neuner, E. Becker, H.-H. Johannes, and W. Kowalsky, "Inverted top-emitting organic light-emitting diodes using sputter-deposited anodes," *Applied Physics Letters*, vol. 82, no. 2, pp. 284–286, 2003.

[55] R. Ruiz, H. Kang, F. A. Detcheverry, E. Dobisz, D. S. Kercher, T. R. Albrecht, J. J. d. Pablo, and P. F. Nealey, "Density Multiplication and Improved Lithography by Directed Block Copolymer Assembly," *Science*, vol. 321, pp. 936–939, 2008.

[56] D. V. Kondratuk, L. M. A. P. ao, M. C. O'Sullivan, S. A. Svatek, G. Smith, J. N. O'Shea, P. H. Beton, and H. L. Anderson, "Two Vernier-Templated Routes to a 24-Porphyrin Nanoring," *Angewandte Chemie International Edition*, vol. 51, pp. 6696–6699, 2012.

[57] G. McDermott, S. M. Prince, A. A. Freer, A. M. Hawthornrhwaite-Lawless, R. J. C. M. Z. Papiz, and N. W. Isaacs, "Crystal structure of an integral membrane light-harvesting complex from photosynthetic bacteria," *Nature*, vol. 374, pp. 517–521, 1994.

[58] S. Scheuring, J. Seguin, S. Marco, D. Lévy, B. Robert, and J. L. Rigaud, "Nanodissection and high-resolution imaging of the Rhodopseudomonas viridis photosynthetic core complex in native membranes by AFM," *Proceedings of the National Academy of Sciences*, vol. 100, pp. 1690–1693, 2003.

[59] C. Hunter, "Supramolecular chemistry: Bigger and better synthesis," *Nature*, vol. 469, p. 39–41, 2011.

[60] M. Affronte, "Molecular nanomagnets for information technologies," *Journal of Materials Chemistry*, vol. 19, no. 12, pp. 1731–1737, 2009.

[61] L. Bogani and W. Wernsdorfer, "Molecular spintronics using single-molecule magnets," *Nature Materials*, vol. 7, no. 3, pp. 179–186, 2008.

[62] M. N. Leuenberger and D. Loss, "Quantum computing in molecular magnets," *Nature*, vol. 410, pp. 789–793, 2001.

[63] F. Meier, J. Levy, and D. Loss, "Quantum computing with spin cluster qubits," *Physical Review Letters*, vol. 90, pp. 047901–047901–4, 2003.

[64] M. Affronte, F. Troiani, A. Ghirri, A. Candini, M. Evangelisti, V. Corradini, S. Carretta, P. Santini, G. Amoretti, F. Tuna, G. Timco, and R. E. P. Winpenny, "Single molecule magnets for quantum computation," *Journal of Physics D: Applied Physics*, vol. 40, no. 10, pp. 2999–3004, 2007.

[65] R. Winpenny, *Single-Molecule Magnets and Related Phenomena.* Springer-Verlag, Berlin, 2006.

[66] D. Gatteschi and R. Sessoli, "Quantum tunneling of magnetization and related phenomena in molecular materials," *Angewandte Chemie International Edition*, vol. 42, pp. 268–297, 2003.

[67] A. Caneschi, D. Gatteschi, and R. Sessoli 1991.

[68] R. Sessoli, "Large Magnetic Anisotropy in High Spin Clusters; a Route to Magnetic Hysteresis at the Molecular Level," *Molecular Crystals and Liquid Crystals Science and Technology. Section A. Molecular Crystals and Liquid Crystals*, vol. 274, pp. 145–157, 1995.

[69] R. E. P. Winpenny, "Serendipitous assembly of polynuclear cage compounds," *Journal of the Chemical Society, Dalton Transactions*, vol. 274, pp. 1–10, 2002.

[70] S. Osa, T. Kido, N. Matsumoto, N. Re, A. Pochaba, and J. Mrozinski, "A Tetranuclear 3d-4f Single Molecule Magnet: $[Cu^{II}LTb^{III}(hfac)_2]_2$," *Journal of the American Chemical Society*, vol. 126, pp. 420–421, 2004.

[71] C. M. Zaleski, E. C. Depperman, J. W. Kampf, M. L. Kirk, and V. L. Pecoraro, "Synthesis, Structure, and Magnetic Properties of a Large Lanthanide–Transition–Metal Single–Molecule Magnet," *Angewandte Chemie*, vol. 116, pp. 4002–4004, 2004.

[72] D. Gatteschi, R. Sessolia, and A. Corniab, "Single-molecule magnets based on iron(III) oxo clusters," *Chemical Communications*, vol. 9, pp. 725–732, 2000.

[73] R. Winpenny, *Molecular Cluster Magnets*. World Scientific, 2011.

[74] A. Saywell, A. J. Britton, N. Taleb, M. d. C. Giménez-López, N. R. Champness, P. H. Beton, and J. N. O'Shea, "Single molecule magnets on a gold surface: *in situ* electrospray deposition, X-ray absorption and photoemission," *Nanotechnology*, vol. 22, pp. 075704–075704–7, 2011.

[75] A. Saywell, G. Magnano, C. J. Satterley, L. M. A. Perdigão, A. J. Britton, N. Taleb, M. del Carmen Giménez-López, N. R. Champness, J. N. O'Shea, and P. H. Beton, "Self-assembled aggregates formed of single molecule magnets on a gold surface," *Nature Communications*, vol. 1, pp. 75–75–8, 2010.

[76] S. Kahle, Z. Deng, N. Malinowski, C. Tonnoir, A. Forment-Aliaga, N. Thontasen, G. Rinke, D. Le, V. Turkowski, T. S. Rahman, S. Rauschenbach, M. Ternes, and K. Kern, "The Quantum Magnetism of Individual Manganese–12–Acetate Molecular Magnets Anchored at Surfaces," *Nano Letters*, vol. 12, pp. 518–521, 2011.

[77] K. Handrup, V. J. Richards, M. Weston, N. R. Champness, and J. N. O'Shea, "Single molecule magnets with protective ligand shells on gold and titanium dioxide surfaces: In situ electrospray deposition and x-ray absorption spectroscopy," *The Journal of Chemical Physics*, vol. 139, pp. 154708–154708–5, 2013.

[78] K. Sun, K. Park, J. Xie, J. L. H. Yuan, Z. Xiong, J. Wang, and Q. Xue, "Direct Observation of Molecular Orbitals in an Individual Single–Molecule Magnet Mn_{12} on Bi(111)," *ACS Nano*, vol. 7, pp. 6825–6830, 2013.

[79] R. F. Weinland and G. Fischer, "Über Manganiacetate und –benzoate," *Zeitschrift für anorganische und allgemeine Chemie*, vol. 120, pp. 161–180, 1921.

[80] A. H. Reidies, "Manganese Compounds," *Ullmann's Encyclopedia of Industrial Chemistry*, vol. 20, p. 495–542, 2000.

[81] G. Rayner-Canham and T. Overton, *Descriptive Inorganic Chemistry*. W. H. Freeman, 3th ed., 2003.

[82] E. Chalmin, M. Menu, and C. Vignaud, "Analysis of rock art painting and technology of Palaeolithic painters," *Measuremen Science and Technology*, vol. 14, pp. 1590–1597, 2003.

[83] R. Sessoli, H. L. Tsai, A. R. Schakes, S. Y. Wang, J. B. Vincent, K. Folting, D. Gatteschi, G. Christou, and D. N. Hendrickson, "High sping molecules," *Journal of the American Chemical Society*, vol. 115, pp. 1804–1816, 1993.

[84] T. Lis, "Preparation, Structurem and Magnetic Properties of a Dodecanuclaer Mixed–Valence Manganese Carboxylate," *Structural Crystallography and Crystal Chemistry*, vol. B36, pp. 2042–2046, 1980.

[85] R. Sessoli, D. Gatteschi, A. Caneschi, and M. A. Novak, "Magnetic bistability in a metal-ion cluster," *Nature*, vol. 365, pp. 141–143, 1993.

[86] F. Pineider, M. Mannini, R. Sessoli, A. Caneschi, D. Barreca, L. Armelao, A. Cornia, E. Tondello, and D. Gatteschi, "Solvent Effects on the Adsorption and Self–Organization Mn_{12} on Au(111)," *Langmuir*, vol. 23, pp. 11836–11843, 2007.

[87] S. Voss, O. Zander, M. Fonin, U. Rüderger, M. Burgert, and U. Groth, "Electronic transport properties and orientation of individual Mn_{12} single–molecule magnets," *Physical Review Letters B*, vol. 78, pp. 155403–155403–5, 2008.

[88] M. Mannini, P. Sainctavit, R. Sessoli, C. C. Moulin, F. Pineider, M. Arrio, A. Cornia, and D. Gatteschi, "XAS and XMCD Investigation of Mn_{12} Monolayers on Gold," *Chemistry - A European Journal*, vol. 14, pp. 7530–7535, 2008.

[89] G. Rogez, B. Donnio, E. Terazzi, J. L. Gallani, J. P. Kappler, J. P. Bucher, and M. Drillon, "The quest for nanoscale magnets: The example of [mn12] single molecule magnets," *Advanced Materials*, vol. 21, p. 4323–4333, 2009.

[90] S. M. J. Aubin, Z. M. Sun, H. J. Eppley, R. M. Rumberger, I. A. Guzei, K. Folting, P. K. Gantzel, A. L. Rheingold, G. Christou, and D. N. Hendrickson, "Single–molecule magnets: Jahn–Teller isomerism and the origin of two magnetization relaxation processes in Mn_{12} complexes," *Polyhedron*, vol. 20, no. 11-14, pp. 1139–1145, 2001.

[91] S. Phark, Z. G. Khim, B. J. Kim, B. J. Suh, S. Yoon, J. Kim, J. M. Lim, and Y. Do, "Atomic Force Microscopy Study of $Mn_{12}o_{12}(o_2cc_4h_3s)_{16}(h_2o)_4$ Single–Molecule Magnet Adsorbed on Au Surface," *Japanese Journal of Applied Physics*, vol. 43, no. 12, pp. 8273–8277, 2004.

[92] A. Naitabdi, J. P. Bucher, P. Gerbier, P. Rabu, and M. Drillon, "Self–Assembly and Magnetism of Mn_{12} Nanomagnets on Native and Func-

tionalized Gold Surfaces," *Advanced Materials*, vol. 17, pp. 1612–1616, 2005.

[93] V. E. Henrich, "The nature of transition–metal–oxide surfaces," *Progress in Surface Science*, vol. 14, pp. 175–199, 1983.

[94] D. Vogtenhuber, R. Podloucky, and A. Neckel, "Electronic structure and relaxed geometry of the ti0_2 rutile (110) surface," *Physical Review B*, vol. 49, pp. 2099–2103, 1994.

[95] J. V. Barth, H. Brune, G. Ertl, and R. J. Behm, "Scanning tunneling microscopy observations on the reconstructed Au(111) surface: Atomic structure, long-range superstructure, rotational domains, and surface defects," *Physical Review B*, vol. 42, pp. 9307–9318, 1990.

[96] V. May and O. Köhn, *Charge and energy transfer dynamics in molecular systems.* Wiley-VCH, Berlin, 2000.

[97] R. J. D. Miller, G. L. McLendon, A. J. Nozik, W. Schmickler, and F. Willig, *Surface electron transfer processes.* New York: VCH, 1995.

[98] N. Sutin, "Electron transfer reactions in solution: a historical perspective," *Advances in Chemical Physics: Electron Transfer - from Isolated Molecules to Biomolecules*, vol. 106, 2007.

[99] N. W. Ashcroft and N. D. Mermin, *Solid State Physics.* Cornell University, 1976.

[100] J. Jortner and M. Bixon, "Intramolecular vibrational excitations accompanying solvent-controlled electron transfer reactions," *Journal of Chyemical Physics*, vol. 88, pp. 167–170, 1988.

[101] M. Bixon and J. Jortner, "Electron Transfer - from Isolated Molecules to Biomolecules," *Advances in Chemical Physics*, vol. 106, 1999.

[102] R. A. Marcus, "On the Theory of Oxidation-Reduction Reactions Involving Electron Transfer. I," *The Journal of Chemical Physics*, vol. 24, pp. 966–978, 1956.

[103] R. A. Marcus, "Electrostatic free energy and other properties of states having nonequilibrium polarization. I," *Journal of Chemical Physics*, vol. 24, pp. 979–989, 1956.

[104] R. A. Marcus, "Chemical and Electrochemical Electron-Transfer Theory," *Annual Review of Physical Chemistry*, vol. 15, pp. 155–196, 1964.

[105] P. W. Atkins, *Physical Chemnistry*. Oxford University Press, 1998.

[106] R. A. Marcus, "Electron transfer reactions in chemistry: Theory and experiment." Nobel lecture, 1992.

[107] R. A. Marcus and N. Sutin, "Electron transfers in chemistry and biology," *Biochimica et Biophysica Acta*, vol. 811, pp. 265–322, 1985.

[108] J. S. Bader and D. Chandler, "Computer Simulation of Photochemically Induced Electron Transfer," *Chemical Physics Letters*, vol. 157, pp. 501–504, 1989.

[109] J. R. Hook and H. E. Hall, *Solid State Physics*. Wiley, 2001.

[110] C. Kittel, *Introduction to Solid State Physics*. Wiley, 1996.

[111] J. M. Lanzafame, S. Palese, D. Wang, R. J. D. Miller, and A. A. Muenter, "Ultrafast non-linear optical studies of surface reaction dynamics: Mapping the electron trajectory," *Journal of Chemical Physics*, vol. 98, pp. 11020–11033, 1994.

[112] J. M. Lanzafame, R. J. D. Miller, A. A. Muenter, and B. A. Parkinson, "Ultrafast charge-transfer dynamics at SnS_2 surfaces," *Journal of Chemical Physics*, vol. 96, pp. 2820–2826, 1992.

[113] M. Knudsen, "Die gesetze der Molekularströmung und der inneren Reibungsströmung der Gase durch Röhren," *Annalen der Physik*, vol. 333, pp. 75–130, 1909.

[114] M. Knudsen, "Experimentelle Bestimmung des Druckes gesättigter Quecksilberdämpfe bei 0° und höheren Temperaturen," *Annalen der Physik*, vol. 334, pp. 179–193, 1909.

[115] W. P. McCray, "MBE deserves a place in the history books," *Nature Nanotechnology*, vol. 2, pp. 259–261, 2007.

[116] L. Grill, "Large molecules on surfaces: deposition and intramolecular STM manipulation by directional forces," *Journal of Physics: Condensed Matter*, vol. 22, pp. 084023–14, 2010.

[117] T. Zambelli, P. Jiang, J. Lagoute, S. E. Grillo, S. Gauthier, A. Gourdon, and C. Joachim, "Deformation of a 3.7-nm long molecular wire at a metallic step edge," *Physical Review B*, vol. 66, pp. 075410–075410–7, 2002.

[118] C. M. Whitehouse, R. N. Dreyer, M. Yamashita, and J. B. Fenn *Analytical Chemistry*, vol. 57, pages = 675-679, title = Electrospray interface for liquid chromatographs and mass spectrometers, 1985.

[119] J. B. Fenn, M. Mann, C. K. Meng, S. F. Wong, and C. M. Whitehouse, "Electrospray ionization for mass spectrometry of large biomolecules," *Science*, vol. 246, pp. 64–71, 1989.

[120] S. J. Gaskell, "Electrospray: Principles and Practice," *Journal of Mass Spectroscopy*, vol. 32, pp. 677–688, 1989.

[121] J. N. O'Shea, J. B. Taylor, J. C. Swarbrick, G. Magnano, L. C. Mayor, and K. Schulte, "Electrospray deposition of carbon nanotubes in vacuum," *Nanotechnology*, vol. 18, pp. 035707–035707–4, 2007.

[122] L. C. Mayor, A. Saywell, G. Magnano, C. J. Satterley, J. Schnadt, and J. N. O'Shea, "Adsorption of a Ru(II)dye complex on the Au(111) surface: Photoemission and scanning tunneling microscopy," *Journal of Chemical Physics*, vol. 130, pp. 164704–164704–6, 2009.

[123] C. J. Satterley, L. M. A. Perdigao, A. Saywell, G. Magnano, A. Rienzo, L. C. Mayor, V. R. Dhanak, P. H. Beton, and J. N. O'Shea, "Electrospray deposition of fullerenes in ultra-high vacuum: *in situ* scanning tunneling microscopy and photoemission spectroscopy," *Nanotechnology*, vol. 18, pp. 455304–455304–5, 2007.

[124] A. Saywell, G. Magnano, C. J. Satterley, L. M. A. Perdigao, N. R. Champness, P. H. Beton, and J. N. O'Shea, "Electrospray Deposition of C_{60} on a Hydrogen–Bonded Supramolecular Network," *Journal of Chemical Physics*, vol. 112, pp. 7706–7709, 2008.

[125] M. Weston, T. J. Reade, A. J. Britton, K. Handrup, N. R. Champness, and J. N. O'Shea, "A single centre water splitting dye complex adsorbed on rutile $TiO_2(110)$: Photoemission, X-ray absorption, and optical spectroscopy," *The Journal of Chemical Physics*, vol. 135, pp. 114703–114703–8, 2011.

[126] M. Weston, A. J. Britton, and J. N. O'Shea, "Charge transfer dynamics of model charge transfer centers of a multicenter water splitting dye complex on rutile $TiO_2(110)$," *The Journal of Chemical Physics*, vol. 134, pp. 054705–054705–10, 2011.

[127] A. Rienzo, L. C. Mayor, G. Magnano, C. J. Satterley, E. Ataman, J. Schnadt, K. Schulte, and J. N. O'Shea, "X-ray absorption and photoemission spectroscopy of zinc protoporphyrin adsorbed on rutile $TiO_2(110)$ prepared by in situ electrospray deposition," *Journal of Chemical Physics*, vol. 132, pp. 084703–084703–6, 2010.

[128] A. J. Britton, M. Weston, J. B. Taylor, A. Rienzo, L. C. Mayor, and J. N. O'Shea, "Charge transfer interactions of a Ru(II) dye complex and

related ligand molecules adsorbed on Au(111)," *The Journal of Chemical Physics*, vol. 135, pp. 164702–164702–8, 2011.

[129] M. Weston, K. Handrup, T. J. Reade, N. R. Champness, and J. N. O'Shea, "Experimental observation of sub-femtosecond charge transfer in a model water splitting dye-sensitized solar cell," *Journal of Chemical Physics*, vol. 137, pp. 224706–224706–7, 2012.

[130] P. Kebarle and L. Tang, "From ions in solution to ions in the gas phase – the mechanism of electrospray mass spectrometry," *Analytical Chemistry*, vol. 65, p. 972A–986A, 1993.

[131] A. M. Gañán-Calvo, "Cone-Jet Analytical Extension of Taylor's Electrostatic Solution and the Asymptotic Universal Scaling Laws in Electrospraying," *Physical Review Letters*, vol. 79, pp. 217–220, 1997.

[132] J. F. D. L. Mora, J. Navascues, F. Fernandez, and J. Rosell-Llompart, "Generation of submicron monodisperse aerosols in electrosprays," *Journal of Aerosol Science*, vol. 21, pp. S673–S676, 1990.

[133] R. B. Cole, "Some tenets pertaining to electrospray ionization mass spectrometry," *Journal of Mass Spectrometry*, vol. 35, pp. 763–722, 2000.

[134] P. Willmott, *Introduction to Synchrotron Radiation: Techniques and Applications*. Wiley, 2011.

[135] D. Attwood, *Soft X-rays and Extreme Ultraviolet Radiation – Principles and Applications*. Springer-Verlag, 1st ed., 2000.

[136] M. P. Seah and W. A. Dench, "Quantitative Electron Spectroscopy of Surfaces: A Standard Data Base for Electron Inelastic Mean Free Paths in Solids," *Surface and Interface Analysis*, vol. 1, pp. 2–11, 1979.

[137] H. Hertz, "Über einen einfluss des ultravioletten lichtes auf die electrische entladung," *Annalen der Physik*, vol. 267, pp. 983–1000, 1887.

[138] A. Einstein, "Über einen die erzeugung und verwandlung des lichtes betreffenden heuristischen gesichtspunkt," *Annalen der Physik*, vol. 17, pp. 132–148, 1905.

[139] S. Hüfner, *Photoelectron Spectroscopy*. Springer-Verlag, 3nd ed., 2003.

[140] L. C. Mayor, *The adsorption and charge-transfer dynamics of model dye sensitized solar cells*. University of Nottingham, ph.d. thesis ed., 2009.

[141] D. P. Woodruff and T. A. Delchar., *Modern Techniques of Surface Science*. University Press, 2nd ed., 1994.

[142] G. D. Mahan, "Theory of Photoemission in Simple Metals," *Physical Review Letters B*, vol. 2, pp. 4334–4350, 1970.

[143] J. B. Pendry, "Theory of photoemission," *Surface Science*, vol. 57, pp. 679–705, 1976.

[144] J. Stöhr, *NEXAFS Spectroscopy*. Springer-Verlag, 1996.

[145] M. Hollas, *Modern Spectroscopy*. John Wiley & Sons, 4th ed., 2004.

[146] J. L. Campbell and T. Papp, "WIDTHS OF THE ATOMIC K–N7 LEVELS," *Atomic Data and Nuclear Data Tables*, vol. 77, pp. 1–56, 2001.

[147] A. Thorne, U. Litzèn, and S. Johansson, *Spectrophysics: principles and applications*. Springer, Berlin, 1999.

[148] P. Atkins and R. Friedman, *Molecular Quantum Mechanics*. Oxford University Press, New York, 4th ed., 2005.

[149] K. Siegbahn, "Electron spectroscopy - an outlook," *Journal of Electron Spectroscopy and Related Phenomena*, vol. 5, pp. 3–97, 1974.

[150] J. Stöhr and D. A. Outka, "Determination of molecular orientations on surfaces from the angular dependence of near-edge x-ray-absorption fine-structure spectra," *Physical Review B*, vol. 36, pp. 7891–7905, 1987.

[151] R. Nyholm, J. N. Andersen, U. Johansson, B. N. Jensen, and I. Lindau, "Beamline I311 at MAX-LAB: A VUV/Soft X-Ray Undulator Beamline for High Resolution Electron Spectroscopy," *Nuclear Instruments and Methods in Physics Research Section A: Accelerators, Spectrometers, Detectors and Associated Equipment*, vol. 467-468, pp. 520–524, 2001.

[152] K. T. Boon, *EXAFS: Basic Principles and Data Analysis.* Springer, 1986.

[153] Y. Zubavichus, Y. J. Yang, M. Zharnikov, O. Fuchs, T. Schmidt, C. Heske, E. Umbach, G. Tzvetkov, F. P. Netzer, and M. Grunze, "Local Structure of Amorphous Ice as Revealed by O K-edge EXAFS," *ChemPhysChem*, vol. 5, pp. 509–514, 2004.

[154] Y. Zubavichus, M. Zharnikov, Y. J. Yang, O. Fuchs, E. Umbach, C. Heske, and M. Grunze, "Oxygen K-edge X-ray Absorption Fine Structure Studies of Vacuum-Deposited Ice Films," *Langmuir*, vol. 22, pp. 7241–7247, 2006.

[155] J. Schnadt, J. Schiessling, and P. A. Brühwiler, "Comparison of the size of excitonic effects in molecular π systems as measured by core and valence spectroscopies," *Chemical Physics*, vol. 312, pp. 39–45, 2005.

[156] P. A. Brühwiler, O. Karis, and N. Mårtensson, "Charge-transfer dynamics studied using resonant core spectroscopies," *Reviews of Modern Physics*, vol. 74, pp. 703–740, 2002.

[157] J. Schnadt, A. Henningsson, M. P. Andersson, P. G. Karlsson, P. Uvdal, H. Siegbahn, P. A. Brühwiler, and A. Sandell, "Adsorption and charge-transfer study of bi-isonicotinic acid on in situ-grown anatase TiO_2 nanoparticles," *The Journal of Physical Chemistry B*, vol. 108, pp. 3114–3122, 2004.

[158] W. Wurth and D. Menzel, "Ultrafast electron dynamics at surfaces probed by resonant Auger spectroscopy," *Chemical Physics*, vol. 251, pp. 141–149, 2000.

[159] O. Björneholm, A. Nilsson, A. S., B. Hernnäs, and N. Mårtensson, "Determination of time scales for charge-transfer screening in physisorbed molecule," *Physical Review Letters*, vol. 68, pp. 1892–1895, 1992.

[160] W. Eberhardt, R. Dudde, M. L. M. Rocco, E. E. Koch, and S. Bernstorff, "Dynamic screening effects observed in the deexcitation of core electron excited states in molecules," *Journal of Electron Spectroscopy and Related Phenomena*, vol. 51, pp. 373–382, 1990.

[161] C. Westphal, "The study of the local atomic structure by means of X-ray photoelectron diffraction," *Surface Science Reports*, vol. 50, pp. 1–106, 2003.

[162] E. M. Purcell, "The Focusing of Charged Particles by a Spherical Condenser," *Physical Review*, vol. 54, pp. 818–826, 1938.

[163] R. Nyholm, S. Svensson, and J. Nordgren, "A soft X-ray monochromator for the MAX synchrotron radiation facility," *Nuclear Instruments and Methods in Physics Research Section A: Accelerators, Spectrometers, Detectors and Associated Equipment*, vol. 246, pp. 267–271, 1986.

[164] J. N. Andersen, O. Björneholm, A. Sandell, R. Nyholm, J. Forsell, L. Thånell, A. Nilsson, and N. Mårtensson, "Photoemission spectroscopy at MAX-Lab," *Synchrotron Radiation News*, vol. 4, pp. 15–19, 1991.

[165] L. J. P. Ament, M. v. Veenendaal, T. P. Devereaux, J. P. Hill, and J. v. d. Brink, "Resonant inelastic x-ray scattering studies of elementary excitations," *Review of Modern Physics*, vol. 83, pp. 705–767, 2011.

[166] M. A. Novak, R. Sessoli, A. Caneschi, and D. Gatteschi, "Magnetic properties of a mn cluster organic compound," *Journal of Magnetism and Magnetic Materials*, vol. 146, pp. 211–213, 1995.

[167] L. Zobbi, M. Mannini, M. Pacchioni, G. Chastanet, D. Bonacchi, C. Zanardi, R. Biagi, D. d. Pennino, D. Gatteschi, A. Cornia, and R. Sessoli, "Isolated single-molecule magnets on native gold," *Chemical Communications*, no. 12, pp. 1640–1642, 2005.

[168] V. Corradini, U. d. Pennino, R. Biagi, V. D. Renzi, A. Gambardella, G. C. Gazzadi, A. Candini, L. Zobbi, and A. Cornia, "Self–assembling of mn_{12} molecular nanomagnets on FIB-patterned Au dot matrix," *Surface Science*, vol. 601, no. 13, pp. 2618–2622, 2007.

[169] S. H. Phark, Z. G. Khim, J. M. Lim, J. Kim, and S. Yoon, "Study on the films of a single-molecule magnet Mn_{12} modified by the selective insertion of a sulfur-terminated ligand," *Journal of Magnetism and Magnetic Materials*, vol. 310, pp. E483–E485, 2007.

[170] U. d. Penninoa, V. D. Renzia, R. Biagia, V. Corradinib, L. Zobbic, A. Corniac, D. Gatteschid, F. Bondinoe, E. Magnanoe, M. Zangrandoe, M. Zacchignae, A. Lichtensteinfa, and D. W. Boukhvalovg 2006.

[171] J. S. Steckel, N. S. Persky, C. R. Martinez, C. L. Barnes, E. A. Fry, J. Kulkarni, J. D. Burgess, R. B. Pacheco, and S. L. Stoll, "Monolayer and Multilayer Films of $[Mn_{12}o_{12}(o_2cme)_{16}]$," *Nano Letters*, vol. 4, pp. 399–402, 2004.

[172] E. Coronado, A. Forment-Aliaga, F. M. Romero, V. Corradini, R. Biagi, V. D. Renzi, A. Gambardella, and U. d. Pennino, "Isolated Mn_{12} Single–Molecule Magnets Grafted on Gold Surfaces via Electrostatic Interactions," *Inorganic Chemistry*, vol. 44, pp. 7693–7695, 2005.

[173] R. V. Martínez, F. García, R. García, E. Coronado, A. Forment-Aliaga, F. M. Romero, and S. Tatay, "Nanoscale Deposition of Single–Molecule Magnets onto SiO_2 Patterns," *Advanced Materials*, vol. 19, pp. 291–295, 2007.

[174] J. Means, V. Meenakshi, R. V. A. Srivastava, W. Teizer, A. Kolomenskii, H. A. Schuessler, H. Zhao, and K. R. Dunbar, "Films of Mn_{12}–acetate deposited by low–energy laser ablation," *Journal of Magnetism and Magnetic Materials*, vol. 284, pp. 215–219, 2004.

[175] V. Meenakshi, W. Teizer, D. G. Naugle, H. Zhao, and K. R. Dunbar, "Films of Mn_{12}-acetate by pulsed laser evaporation," *Solid State Communications*, vol. 132, no. 7, pp. 471–476, 2004.

[176] R. Moroni, R. Buzio, A. Chincarini, U. Valbusa, F. B. d. Mongeot, L. Bogani, A. Caneschi, R. Sessoli, L. Cavigli, and M. Gurioli, "Optically addressable single molecule magnet behaviour of vacuum-sprayed ultrathin films," *Journal of Materials Chemistry*, vol. 18, no. 48, pp. 109–115, 2008.

[177] L. Vitali, S. Fabris, A. M. Conte, S. Brink, M. Ruben, S. Baroni, and K. Kern, "Electronic Structure of Surface–supported Bis(phthalocyaninato) terbium(III) Single Molecular Magnets," *Nano Letters*, vol. 8, no. 10, pp. 3364–3368, 2008.

[178] A. L. Barra, A. Caneschi, D. Gatteschi, D. P. Goldberg, and R. Sessoli, "Slow Magnetic Relaxation of $[Et_3NH]_2Mn(CH3CN)_4(H_2O)_2]$ $[Mn10O_4(biphen)_4Br_{12}]$ (biphen=2,2'-biphenoxide) at Very Low Temperature," *Journal of Solid State Chemistry*, vol. 145, pp. 484–487, 1999.

[179] S. Voss, M. Fonin, U. Ruediger, M. Burgert, U. Groth, and Y. S. Dedkov, "Electronic structure of mn_{12} derivatives on the clean and functionalized Au surface," *Physical Review B*, vol. 75, pp. 045102–045102–7, 2007.

[180] S. Voss, M. Fonin, L. Burova, M. Burgert, Y. S. Dedkov, A. B. Preobrajenski, E. Goering, U. Groth, A. R. Kaul, and U. Ruediger, "Investigation of the stability of Mn_{12} single molecule magnets," *Applied Physics A*, vol. 94, pp. 491–495, 2009.

[181] M. Mannini, F. Pineider, P. Sainctavit, L. Joly, A. Fraile-Rodriguez, M. Arrio, C. C. Moulin, W. Wernsdorfer, A. Cornia, D. Gatteschi,

and R. Sessoli, "X–Ray Magnetic Circular Dichroism Picks out Single–Molecule Magnets Suitable for Nanodevices," *Advanced Materials*, vol. 21, pp. 167–171, 2009.

[182] S. G. Chiuzbaian and C. Hague, "High acceptance high resolution soft X-ray grating spectrometer: Choice of optical design," *Journal of Electron Spectroscopy and Related Phenomena*, vol. 188, pp. 121–126, 2012.

[183] U. Diebold, "The surface science of titanium dioxide," *Surface Science Reports*, vol. 48, pp. 53–229, 2003.

[184] J. N. O'Shea, J. B. Taylor, L. C. Mayor, J. C. Swarbrick, and J. Schnadt, "Molecular damage in bi-isonicotinic acid adsorbed on rutile $Tio_2(110)$," *Surface Science*, vol. 602, pp. 1693–1698, 2008.

[185] F. Hennies, S. Polyutov, I. Minkov, A. Pietzsch, M. Nagasono, F. Gel'mukhanov, L. Triguero, M.-N. Piancastelli, W. Wurth, H. Ågren, and A. Föhlisch, "Nonadiabatic Effects in Resonant Inelastic X-ray Scattering," *Physical Review Letter*, vol. 95, pp. 163002–163002–4, 2005.

[186] Y. Ma, P. Skytt, N. Wassdahl, P. Glans, D. C. Mancini, J. Guo, and J. Nordgren, "Core Excitons and Vibronic Coupling in Diamond and Graphite," *Physical Review Letter*, vol. 71, pp. 3725–3728, 1993.

[187] Y. Harada, T. Tokushima, Y. Takata, T. Takeuchi, Y. Kitajima, S. Tanaka, Y. Kayanuma, and S. Shin, "Dynamical Symmetry Breaking under Core Excitation in Graphite: Polarization Correlation in Soft X-ray Recombination Emission," *Physical Review Letter*, vol. 93, pp. 017401–017401–4, 2004.

[188] B. Kempgens, A. Kivimäki, M. Neeb, H. M. Köppe, A. M. Bradshaw, and J. Feldhaus, "A high-resolution N 1s photoionization study of the N_2 molecule in the near-threshold region," *Journal of Physics B: Atomic, Molecular and Optical*, vol. 29, pp. 5389–5402, 1996.

[189] R. H. Friend, R. W. Gymer, A. B. Holmes, J. H. Burroughes, R. N. Marks, C. Taliani, D. D. C. Bradley, D. A. D. Santos, M. L. J. L. Brédas, and W. R. Salaneck, "Electroluminescence in conjugated polymers," *Nature*, vol. 395, pp. 257–260, 1999.

[190] B. R. D'Andrade, R. J. Holmes, and S. R. Forrest, "Efficient Organic Electrophosphorescent White-Light-Emitting Device with a Triple Doped Emissive Layer," *Advanced Materials*, vol. 16, pp. 624–628, 2004.

[191] J.-S. Kim, F. Cacialli, and R. Friend, "Surface conditioning of indium-tin oxide anodes for organic light-emitting diodes," *Thin Solid Films*, vol. 445, no. 2, pp. 358–366, 2003.

[192] C. Väterlein, H. Neureiter, W. Gebauer, B. Ziegler, M. Sokolowski, P. Bäuerle, and E. Umbach, "Organic light emitting devices based on vapor deposited films of end-capped sexithiophene: Evidence for schottky barriers and transport limitations," *Journal of Applied Physics*, vol. 82, no. 6, pp. 3003–3013, 1997.

[193] Y. Gao, L. Wang, D. Zhang, L. Duan, G. Dong, and Y. Qiu, "Bright single-active layer small-molecular organic light-emitting diodes with a polytetrafluoroethylene barrier," *Applied Physical Letters*, vol. 82, pp. 155–157, 2003.

[194] H. E. Katz, M. X. Hong, A. Dodabalapur, and R. Sarpeshkar, "Organic field-effect transistors with polarizable gate insulators," *Applied Physics Letters*, vol. 91, no. 3, pp. 1572–1576, 2002.

[195] H. Sandberg, O. Henze, A. F. M. Kilbinger, H. Sirringhaus, W. J. Feast, and R. H. Friend, "Oligoethyleneoxide functionalised sexithiophene organic field effect transistors," *Synthetic Metals*, vol. 137, no. 1-3, pp. 885–886, 2003.

[196] K. Takimiya, Y. Kunugi, Y. Konda, N. Niihara, and T. Otsubo, "2,6-diphenylbenzo[1,2-*b*:4,5-*b'*]dichalcogenophenes: A New Class of High-

Performance Semiconductors for Organic Field-Effect Transistors," *Journal of American Chemical Society*, vol. 126, no. 16, pp. 5084–5085, 2004.

[197] S. J. Tans, M. H. Devoret, H. Dai, A. Thess, R. E. Smalley, L. J. Geerligs, and C. Dekker, "Individual single-wall carbon nanotubes as quantum wires," *Nature*, vol. 386, pp. 474–477, 1997.

[198] S. Frank, P. Poncharal, Z. L. Wang, and W. A. de Heer, "Carbon Nanotube Quantum Resistors," *Science*, vol. 280, pp. 1744–1746, 1998.

[199] K. Susumu, P. R. Frail, P. J. Angiolillo, and M. J. Therien, "Conjugated Chromophore Arrays with Unusually Large Hole Polaron Delocalization Lengths," *Journal of American Chemical Society*, vol. 128, pp. 8380–8381, 2006.

[200] M. U. Winters, E. Dahlstedt, H. E. Blades, C. J. Wilson, M. J. Frampton, H. L. Anderson, and B. Albinsson, "Probing the Efficiency of Electron Transfer through Porphyrin-Based Molecular Wires," *Journal of American Chemical Society*, vol. 129, pp. 4291–4297, 2007.

[201] G. Sedghi, K. Sawada, L. J. Esdaile, M. Hoffmann, H. L. Anderson, D. Bethell, W. Haiss, S. J. Higgins, and R. J. Nichols, "Single Molecule Conductance of Porphyrin Wires with Ultralow Attenuation," *Journal of American Chemical Society*, vol. 130, pp. 8582–8583, 2008.

[202] F. Schreiber, "Structure and growth of self-assembling monolayers," *Progress in Surface Science*, vol. 65, pp. 151–256, 2000.

[203] *Private communications with Professor Harry L. Anderson.*

[204] J. C. Fuggle and N. N. Mårtensson, "Core-level binding energies in metals," *Journal of Electron Spectroscopy and Related Phenomena*, vol. 21, pp. 278–281, 1980.